การปรับปรุงไทเทเนียมไดออกไซด์ด้วย ไนโตรเจน ซิลิคอน และคาร์บอน สำหรับปฏิกิริยาการเร่งด้วยแสงโดยใช้ตัวเร่งปฏิกิริยาภายใต้แสงที่มองเห็นได้

นายราชัน คล้ายศรี

วิทยานิพนธ์นี้เป็นส่วนหนึ่งของการศึกษาตามหลักสูตรปริญญาวิศวกรรมศาสตรดุษฎีบัณฑิต
สาขาวิชาวิศวกรรมเคมี ภาควิชาวิศวกรรมเคมี
คณะวิศวกรรมศาสตร์ จุฬาลงกรณ์มหาวิทยาลัย
ปีการศึกษา 2560

MODIFICATION OF TITANIUM DIOXIDE WITH NITROGEN, SILICON, AND CARBON FOR
VISIBLE LIGHT PHOTOCATALYSIS

Mr. Rachan Klaysri

A Dissertation Submitted in Partial Fulfillment of the Requirements

for the Degree of Doctor of Engineering Program in Chemical Engineering

Department of Chemical Engineering

Faculty of Engineering

Chulalongkorn University

Academic Year 2017

Thesis Title	MODIFICATION OF TITANIUM DIOXIDE WITH NITROGEN, SILICON, AND CARBON FOR VISIBLE LIGHT PHOTOCATALYSIS
By	Mr. Rachan Klaysri
Field of Study	Chemical Engineering
Thesis Advisor	Professor Piyasan Praserthdam, Dr.Ing.
Thesis Co-Advisor	Professor Peter J. Kelly, Ph.D.

Accepted by the Faculty of Engineering, Chulalongkorn University in Partial Fulfillment of the Requirements for the Doctoral Degree

....Dean of the Faculty of Engineering

(Associate Professor Supot Teachavorasinskun, D.Eng.)

THESIS COMMITTEE

....Chairman

(Professor Suttichai Assabumrungrat, Ph.D.)

....Thesis Advisor

(Professor Piyasan Praserthdam, Dr.Ing.)

....Thesis Co-Advisor

(Professor Peter J. Kelly, Ph.D.)

....Examiner

(Associate Professor Anongnat Somwangthanaroj, Ph.D.)

....Examiner

(Akawat Sirisuk, Ph.D.)

....External Examiner

(Assistant Professor Okorn Mekasuwandumrong, D.Eng.)

ราชัน คล้ายศรี : การปรับปรุงไทเทเนียมไดออกไซด์ด้วย ไนโตรเจน ซิลิคอน และคาร์บอน สำหรับปฏิกิริยาการเร่งด้วยแสงโดยใช้ตัวเร่งปฏิกิริยาภายใต้แสงที่มองเห็นได้ (MODIFICATION OF TITANIUM DIOXIDE WITH NITROGEN, SILICON, AND CARBON FOR VISIBLE LIGHT PHOTOCATALYSIS) อ.ที่ปรึกษาวิทยานิพนธ์หลัก: ศ. ดร. ปิยะสาร ประเสริฐธรรม, อ.ที่ปรึกษาวิทยานิพนธ์ร่วม: ศ. ดร. ปีเตอร์ เจ. เคลลี, 148 หน้า.

ไทเทเนียมไดออกไซด์และไทเทเนียมไดออกไซด์ที่โดปด้วยไนโตรเจนและซิลิคอนเตรียมโดยสองวิธีที่แตกต่างกัน วิธีแรกเป็นการใช้ก๊าซไนโตรเจนเป็นแหล่งของไนโตรเจน และใช้สารเคมีที่ส่วนประกอบของซิลิคอนเป็นแหล่งของซิลิคอน โดยวิธีนี้จะใช้ในการโดปบนไทเทเนียมไดออกไซด์ที่เตรียมด้วยวิธีโซลโวเทอร์มอลและวิธีโซลเจล ไนโตรเจนซิลิคอนโคโดปไทเทเนียมไดออกไซด์ที่เตรียมด้วยวิธีนี้จะให้แอกทิวิทีสูงสุดทั้งภายใต้แสงยูวีและแสงที่มองเห็นได้ การเติมซิลิคอนลงไปจะทำให้เกิดชั้นของซิลิคอนคลุมไทเทเนียมไดออกไซด์บางส่วนซึ่งเป็นการเพิ่มความเสถียรของเฟสอะนาเทส การใช้ก๊าซในการเผาจะส่งผลให้ออกซิเจนบนพื้นผิวและไทเทเนียมไทเทเนียม 3+ เพิ่มขึ้น นอกจากนั้นแล้วอีกวิธีหนึ่งที่ใช้ในการเตรียมไนโตรเจนซิลิคอนโคโดปไทเทเนียมไดออกไซด์คือการใช้สาร Aminopropyltriethoxysilane (APTES) ด้วยวิธีไฮโดรเทอร์มัล วิธีนี้จะทำให้เกิดชั้นของอะมิโนไซเลนปกคลุมไทเทเนียมไดออกไซด์ซึ่งเป็นการลดค่าพลังงานระหว่างช่องว่างและช่วยยับยั้งการรวมตัวกันของอิเลกตรอน-โฮล การเพิ่มปริมาณ APTES ส่งผลให้คุณสมบัติความชอบน้ำลดลงในขณะที่ออกซิเจนและหมู่อะมิโนเพิ่มขึ้น การลดลงของหมู่เอมีนเป็นตัวแปรสำคัญในการเพิ่มแอกทิวิตีของปฏิกิริยา งานวิจัยชิ้นนี้ยังได้อธิบายวิธีการใช้เทคนิคสปัตเตอริงในการโดปคาร์บอนลงบนไทเทเนียมไดออกไซด์แบบฟิล์มบางโดยใช้ก๊าซคาร์บอนไดออกไซด์เป็นแหล่งของคาร์บอน จากผลการวิเคราะห์พบว่าการโดปด้วยคาร์บอนสามารถเพิ่มแอกทิวิทีของปฏิกิริยา สุดท้ายในการวิจัยเล่มนี้ได้มีการศึกษาวิธีการกราฟท์ตัวเร่งปฏิกิริยาไทเทเนียมไดออกไซด์ลงบนแผ่นฟิล์มพีเอ็มเอ็มเอโดยใช้วิธีการเกิดพอลิเมอร์แบบอนุมูลอิสระถ่ายโอนอะตอม (Atom transfer radical polymerization, ATRP) ในงานวิจัยได้ใช้เทคนิคหลาย ๆ เทคนิคในการพิสูจน์ความสำเร็จในการกราฟท์ และพิสูจน์แอกทิวิทีของปฏิกิริยาโดยใช้แสงยูวี โดยแผ่นฟิล์มที่มีการกราฟท์ไทเทเนียมไดออกไซด์สามารถใช้งานซ้ำได้อย่างน้อย 5 ครั้ง

ภาควิชา	วิศวกรรมเคมี	ลายมือชื่อนิสิต ....
สาขาวิชา	วิศวกรรมเคมี	ลายมือชื่อ อ.ที่ปรึกษาหลัก ....
ปีการศึกษา	2560	ลายมือชื่อ อ.ที่ปรึกษาร่วม ....

5771438021 : MAJOR CHEMICAL ENGINEERING

KEYWORDS: TITANIUM DIOXIDE / NITROGEN / SILICON / CARBON / VISIBLE LIGHT / PHOTOCATALYSIS

RACHAN KLAYSRI: MODIFICATION OF TITANIUM DIOXIDE WITH NITROGEN, SILICON, AND CARBON FOR VISIBLE LIGHT PHOTOCATALYSIS. ADVISOR: PROF. PIYASAN PRASERTHDAM, Dr.Ing., CO-ADVISOR: PROF. PETER J. KELLY, Ph.D., 148 pp.

Titanium dioxide and nitrogen-silicon-codoped titanium dioxide were prepared by two different ways. The first method was prepared by using nitrogen as a nitrogen source and silicon-containing chemical as a silicon source via solvothermal- and sol-gel-made photocatalysts. The nitrogen-silicon-codoped titanium dioxide showed the highest photocatalytic activity under both UV and visible light irradiation. The addition of silicon resulted in the formation of partial monolayer of silicon on titanium dioxide and an increase of the anatase phase stability. The annealing atmosphere affected the distribution concentration of surface and interface species such as surface oxygen and Ti^{3+} sites, thus improving photocatalytic activity. Moreover, the other method was prepared by using aminopropyltriethoxysilane (APTES) via hydrothermal method. As results, the monolayer and/or multilayer amino-silane coverage on titanium dioxide surface substantially decreased the indirect band gap, leading to the formation of silicon-nitrogen intermediate level within band gap and suppressing the electron-hole recombination. It subsequently enhanced the photoactivity. With increasing APTES contents, the hydrophilic property was decreased whereas the formation of amine group and the oxygen chemisorption were apparently increased. However, the difference in APTES concentration significantly affected the hydrophobicity. The reduction in protonated amine played an essential role in the retarding of photoactivity. In addition, the present work also describes the use of pulsed direct current magnetron sputtering for the deposition of carbon-doped titanium dioxide thin films, using carbon dioxide as the carbon source. It was found that, though carbon-doping resulted in improved dye degradation compared to undoped titanium dioxide, the UV-induced photoactivity of carbon-doped photocatalysts was lower for model pollutants used. Finally, the grafting of titanium dioxide on PMMA film via atom transfer radical polymerization (ATRP) was also studied. As a result, a method of grafting process was successfully completed and confirmed by various techniques. The photocatalytic activity was evaluated under UV light irradiation. The TiO_2-g-PMMA films was reused at least 5 times.

Department:	Chemical Engineering	Student's Signature ....
Field of Study:	Chemical Engineering	Advisor's Signature ....
Academic Year:	2017	Co-Advisor's Signature ....

ACKNOWLEDGEMENTS

CONTENTS

LIST OF TABLES

Page

จุฬาลงกรณ์มหาวิทยาลัย
CHULALONGKORN UNIVERSITY

LIST OF FIGURES

CHAPTER I

INTRODUCTION

1.1 Rationale

Since the discovery of water photocatalysis by Fujishima and Honda in 1972 [1], photocatalysis has been paid much attention and widely used in various processes. During the past few decades, photocatalysis has been identified as an environmentally friendly process for not only the degradation of organic pollutions [2-4], (air and water remediation, self-cleaning and bactericidal coating), but also the energy production [5-7], (dye sensitised solar cell and hydrogen production). These processes can operate at room temperature. The process needs only atmospheric oxygen to mineralize organic pollutants and light source. Semiconductor nanostructures have attracted considerable interest, such as titanium dioxide, zinc oxide, tin oxide, and cerium oxide, because of their great potential in photocatalysis [8-11]. Among these semiconductors, titanium dioxide (TiO_2) becomes the most promising semiconductor photocatalyst that has been proven by literatures [12-14], due to its nontoxicity [15], low cost [16], high chemical stability [17], strong oxidative ability [18], intriguing electronic structure [19], and commercial availability. The morphology and the structure of titanium dioxide can affect the photocatalytic activity differently [20-23]. Generally, titanium dioxide has a wide band gap (3.2 eV) which is only excited by ultraviolet light, it is inactive under visible light irradiation. The limitations of using titanium dioxide under visible light is poor light adsorption ability and low charge separation efficiency. Therefore, in recent years, studies have begun to modify titanium dioxide to improve the light adsorption of titanium dioxide for efficient utilization of visible light. Various strategies have been developed to enhance the photocatalytic activity of titanium dioxide towards higher wavelength. Some significant advances have been reported to enhance the photocatalytic activity of titanium dioxide based materials; e.g. surface modification [24, 25], structure optimization [26, 27], elemental doping [28, 29], grafting on solid substrates [30, 31], and mixed with other materials [32, 33].

Extensive work in modification of titanium dioxide for visible light photocatalysis started with the pioneering work of researchers who showed that the visible light response of titanium dioxide can be significantly enhanced through nitrogen doping [34]. Doping titanium dioxide with transition metals enhances the photocatalytic activity by inserting a new band gap into the original band gap which modify the conduction band or valence band. Precious metal are widely used to deposit on titanium dioxide surface such as silver, gold, and copper, that is exploited as a light harvester [35-37]. The major drawbacks of the precise metal deposition are the high cost and the efficacy of the method and some of them are toxic and quite expensive. Therefore, replacing precious metal or metal deposition with non-metal deposition, such as nitrogen deposition, is becoming feasible and appears to enhance the visible light photocatalysis [38, 39]. Nitrogen doping is quite encouraging due to its stability, low ionization energy and comparable atomic size. Moreover, nitrogen doping not only suppresses the recombination process but also modifies the titanium dioxide structure. Many studies confirmed that the nitrogen doping titanium dioxide easily increases the visible light photocatalytic activity for environmental remediation applications but further research will be needed to improve alternative pathways for preparing nitrogen doped titanium dioxide. Most of publications of nitrogen-doped titanium dioxide have confirmed its visible light photocatalytic activity. However, the loss of nitrogen-doped titanium dioxide due to annealing may also be one of the most important concern and that resulted in decreased in photocatalytic activity. Therefore, in order to prepare nitrogen-doped titanium dioxide with high photocatalytic efficiency, the annealing in nitrogen atmosphere in synthesis method should be studied in such a way that avoid the loss of nitrogen.

Additionally, the morphology and structure of titanium dioxide are important factors affecting light adsorption, reactant adsorption, and recombination rate resulting in photocatalytic activity. Large number of studies have focused on the titanium dioxide preparation methods. Several methods including solvothermal method [32, 40-44], sol-gel method [45-49], precipitation [50-52], flame spray pyrolysis [53-55], thermal decomposition of alkoxide [56], electrospinning [57, 58], chemical vapour

deposition [59-61], and sputtering [62, 63] have been investigated for the preparation of titanium dioxide photocatalyst.

Focusing on the titanium dioxide preparation, the flame spray pyrolysis method is flexible to produce commodity nanoparticles at the industrial scale and allows the use of a wide range of precursors, solvents and process conditions, thus providing control over particle size and composition but generally the products are composed of morphologically simple particles with large particle sizes [64-66]. The solvothermal is a one-step route that can control over the size, shape distribution, and crystallinity. These properties can be adjusted by changing experimental parameters, such as amount of precursor, reaction temperature, and reaction holding time into well-defined crystal growing to the controllable alcoholysis rate [67]. On the other hand, the sol-gel method is widely used to prepare amorphous titanium dioxide and required an annealing for its crystalline, but this method is a very cost effective and simple technique suitable for large area scaling [68]. Moreover, the sol–gel process has many advantages such as good homogeneity, highly crystalline anatase titanium dioxide photocatalyst and endowed with sophisticated architecture, which easily conducted and especially attractive, but the precipitated powders obtained are amorphous in nature and further heat treatment is required for crystallization [66, 69-71]. The sol-gel method can be used to control morphology and structure. In several cases, the hydrolysis rate of titanium ions is very fast under the aqueous medium. Hydrothermal method has also attract much attention due to its very simple and low cost.

In order to improve the photocatalytic activity of titanium dioxide, the preparation method, the post annealing treatment and the addition of second metal or organic molecules were frequently studied. The addition of a second metalloid such as silicon [72], and metal such as zirconium [73], tungsten [74], cerium [75] and aluminium [76] that increased both of the thermal stability for phase transformation and the surface area of titanium dioxide. For example, silicon-doped titanium dioxide prepared showed high photocatalytic activity due to the suppression of the phase transformation of titanium dioxide from anatase to rutile and the formation of oxygen vacancies [77]. Preparation of titanium dioxide and silicon-doped mesoporous titanium

dioxide continuous fibres via the sol–gel method combined with centrifugal spinning, the addition of proper silica content into titanium dioxide could enhance the thermal stability, crystal stability and photocatalytic activity [78]. Other report has also found that the interaction between titanium dioxide and silica in TiO_2/SiO_2 occurred on supported Ti^{4+} sites and the prepared catalysts had sufficient Lewis acid sites [7]. In this dissertation, titanium dioxide and nitrogen-silicon-codoped titanium dioxide photocatalyst were prepared using the solvothermal and sol-gel methods. The obtained powders were then treated at 723 K under different gas flows, namely, oxygen, air zero, and nitrogen.

Surface modification is an alternative way to improve the performance of titanium dioxide for photocatalyst. Among the covalent surface modification strategies of metal oxide has been widely reported [79, 80]. For example, 3-aminopropyltriethoxysilane (APTES) is one of the most commonly used as organic silane coupling agents for modifying titanium dioxide surface. Many researchers have proposed the possible mechanism of the formation of a covalent linkage between oxide metal surface and the anchoring group of amino-silane coupling agent. The ethoxy groups (CH_3CH_2O-R) of APTES reacted with hydroxyl groups on titanium dioxide surface (Ti-OH) to form the primary Ti-O-Si, therefore, the projection of free NH_2 termination [81, 82] and NH_3^+ protonation [81, 83] can attach on Ti-O-Si surface. The electrostatic interaction or hydrogen bonding between reactive dyes and amine groups can substantially increase the ability of attapulgite adsorptive for reactive dyes from aqueous solution [84].

Generally, APTES modified titanium dioxide surface liked as nitrogen-silicon-codoped titanium dioxide [85]. The partial monolayer of silicon- and nitrogen-doped titanium dioxide can also enhance the adsorption and degradation of methylene blue for photocatalytsis [86, 87]. Moreover, the presence of Ti-O-Si in titanium dioxide surface not only promote the formation of active oxygen species but also increase the mobility of lattice oxygen (O^{2-}), thus changing the electronic band structure of titanium dioxide [88]. Therefore the nitrogen atoms incorporation into titanium dioxide

can significantly create intermediate level within band gap, thus reducing in band edge positions and leading to enhancement of photocatalytic activity in visible region [87].

So far, however, there has been little discussion about an effect of the amine-functional on titanium dioxide on surface properties. Recently, researchers studied the coating of paper with APTES-modified titanium dioxide for photocatalytic degradation of organic material under UV light irradiation [89]. They found that the modification of titanium dioxide by APTES plays a crucial role of the stability in UV-bleaching. Therefore, this dissertation will be focused on the APTES modification titanium dioxide surface in photocatalytic reaction under visible light irradiation.

Additionally, the doping of titanium dioxide with p-block elements still remains a popular method for the synthesis of visible light photocatalysts, along with other techniques, such as transition metal doping [90] or photosensitization. Various p-block elements have been studied as dopants for the enhancement of photocatalytic properties, including nitrogen [91-96], carbon [97], sulphur [98, 99], boron [100], fluorine [101], and combinations of several elements [102, 103]. The exact mechanism of the photocatalytic activity enhancement is still under question, however it is generally accepted that band gap narrowing takes place due to mixing of the $2p$ states of the dopant with the $2p$ states of oxygen [104]. Alternatively, it has been suggested that the red shift observed as a result of p-element doping is due to the formation of colour centres, and that the doped materials may have completely different band gap electronic structures, as compared to undoped titanium dioxide [105].

Compared to nitrogen-doping, carbon-doping is a considerably less studied field, mainly due to fact that synthesis routes for carbon-doped titanium dioxide photocatalysts often involve multiple stages and/or unstable and costly reagents [104]. Nevertheless, a number of studies that are available indicate that carbon doping is a promising method for the enhancement of titanium dioxide photocatalytic activity due to band gap narrowing and the extended lifetime of photogenerated electrons and holes [106, 107]. The well-known fact that carbon-doped titanium dioxide photocatalysts can have very different characteristics, with carbon found in interstitial, as well as in substitutional positions in the titanium dioxide lattice, depending on the

synthesis route, means that the choice of production technique is of particular importance in this case.

Titanium dioxide thin films, as opposed to powdered or particulate photocatalysts, offer multiple advantages from the point of practical applicability, such as high recycle rates, ease of recovery, and separation from the media [108]. A number of deposition techniques are typically used for the deposition of titanium dioxide and doped titanium dioxide coatings, including chemical vapour deposition (CVD), sol gel, atomic layer deposition (ALD), hydrothermal synthesis, magnetron sputtering, etc. Of the methods given, magnetron sputtering is a process of particular industrial importance, as it is widely used for the production of high quality coatings for various commercial applications, including glazing products, thin film photovoltaics, data storage media, etc. [109, 110]. It offers such advantages as excellent scalability, versatility, and high uniformity of the produced thin films. A number of techniques can be used for the deposition of carbon-doped titanium dioxide via magnetron sputtering, including using carbon dioxide gas [111] or solid carbon targets as the source of carbon [112]. However, due to a limited number of studies available to date, it is still unclear how the choice of the dopant affects structural and photocatalytic properties of the carbon-doped titanium dioxide coatings. Also, this work describes the deposition of carbon-doped titanium dioxide using a mixture of carbon dioxide/oxygen as the reactive gas at different ratios.

Furthermore, many researchers have completed important work with titanium dioxide in other particle supports i.e. clay, zeolite and activated carbon [113-115]. The one disadvantage of using titanium dioxide particles in the liquid phase of photocatalysis is their difficulty in being reused. Various techniques have been widely reported for attaching the titanium dioxide nanoparticles to different polymers using different methods such as liquid phase deposition, dip coating technique, phosphonate coupling, chemical reduction, emulsion polymerization and spreading [116-121]. Atom transfer radical polymerization (ATRP) was the most attractive modification method. ATRP covalently grafts monomer chains formed from various monomers effectively to nanoparticles, in order that the chain distribution of

monomers can graft polymers onto nanoparticle surfaces [122]. Moreover, ATRP is a more versatile method because it does not require complex experimental conditions and allows for the polymerization of a large number of functional monomers [123]. ATRP has been widely used to graft polymers onto metal oxides including silicon dioxide, aluminium oxide, ferric oxide and zinc oxide [124-127].

The use of PMMA as a substrate material has several advantages. The PMMA film is a non-porous solid and inexpensive, is stable at high temperatures and has high pH-values. In addition, PMMA is inert in neutral aqueous solutions and no hydrolysis occurs during its application [128, 129]. This work presents and emphasizes a method of grafting titanium dioxide nanoparticles onto PMMA film, using a monomer chain between the titanium dioxide particles and the film substrate in order to protect the PMMA film from degradation caused by the deposited titanium dioxide. The reusability was also studied.

Recently, various characterization techniques have been used to provide the scientific information of titanium dioxide. For example, X-ray diffraction (XRD) X-ray diffraction (XRD) has become a fundamental technique in investigating the crystal phase that can relate to the photocatalytic performance of titanium dioxide. Photoluminescence (PL) provide the photocatalytic reaction mechanism and provide multiscale information of photocatalysis process. X-ray photoelectron spectroscopy (XPS) is possible to probe the electronic state by the shift of the characteristic peaks of the elements in titanium dioxide after modification. This work performs various means of techniques to evaluate the properties of modified titanium dioxide in each sections.

1.2 Research objectives

To investigate the characteristics and catalytic properties of nitrogen and/or silicon doped titanium dioxide nanoparticles prepared by solvothermal and sol-gel methods in the photocatalytic degradation of methylene blue dye under UV and visible light irradiation in comparison to those prepared by other common preparation techniques and commercial titanium dioxide.

To study the hydrothermal surface modification of commercial titanium dioxide by 3-aminopropyltriethoxysilane (APTES) on the photocatalytic degradation of methylene blue dye under UV and visible light irradiation.

To study the carbon-doped titanium dioxide thin film by using carbon dioxide as a carbon source on sputtering process in photocatalytic degradation of methylene blue dye and the photodegradation of stearic acid under both UV light and visible light irradiation in comparison with using carbon target and carbon powder as carbon sources.

To emphasize the grafting process of titanium dioxide on polymethyl methacrylate (PMMA) film by using atomic transfer radical polymerization (ATRP) that was previously studied by other student.

1.3 Scope of research

- Preparation of titanium dioxide support, silicon-doped titanium dioxide by solvothermal and sol-gel methods with 1 wt. % silicon and post-annealing in three different atmospheric gas i.e. oxygen, air, and nitrogen.

- Preparation of APTES modified commercial titanium dioxide with three different APTES concentration i.e. 0.1, 1.0, and 10 mM with using hydrothermal method.

- Preparation of carbon-doped titanium dioxide thin films with three different flow rate of carbon dioxide i.e. 2.5, 5, and 7 mL/min.

- Characterization of the titanium dioxide photocatalysts using X-ray diffraction (XRD), X-ray photoelectron spectroscopy (XPS), scanning electron microscopy

with energy dispersive X-ray spectroscopy (SEM-EDX), electron spin resonance (ESR), nitrogen gas physisorption, stylus profilometer, transmission electron microscope (TEM), UV-vis spectroscopy (UV-vis), thermo gravimetric analysis (TGA), differential scanning calorimetry (DSC), Fourier-transform infrared spectroscopy (FTIR), water contact angle measurement, and nuclear magnetic resonance spectroscopy (NMR).

- Reaction study of the photocatalysts in the photocatalytic degradation of methylene blue dye and/or the photocatalytic degradation of stearic acid under UV and visible light irradiation.

1.4 Research methodology

```
                    ┌─────────────────────────────────┐
                    │  Modification of titanium dioxide │
                    └─────────────────────────────────┘
```

| Nitrogen | Silicon | Carbon |

| Post annealing | Physical mixing | Sputtering |

| O_2 | Air | N_2 | TEOS | Carbon dioxide |

N-Si

APTES

Characterization by means of techniques

Photocatalysis reaction tests
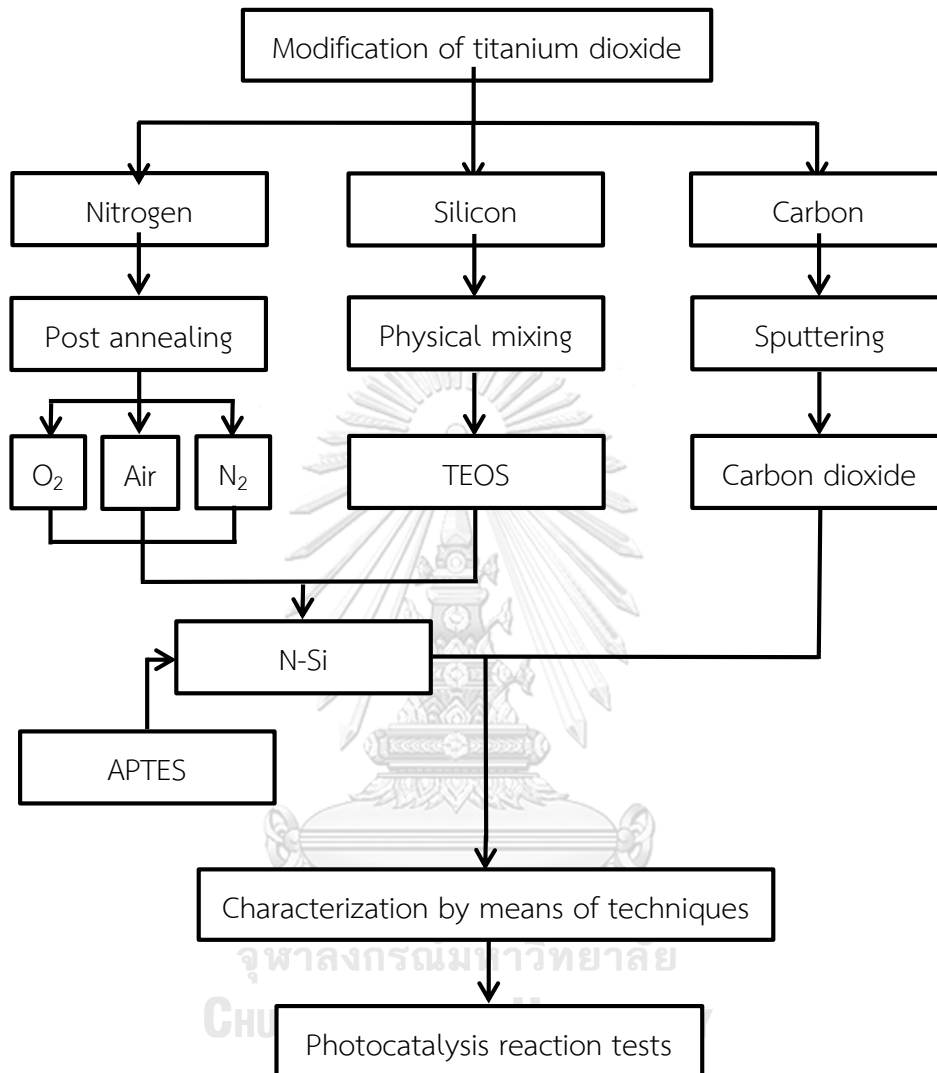
CHAPTER II

THEORY AND LITERATURE REVIEWS

2.1 Titanium dioxide crystal structure and properties

Titanium dioxide exhibits mainly three important polymorphs namely anatase, rutile and brookite. Each polymorph gives different physical properties. In all three polymorphs, titanium (IV) cations are surrounded by six oxygen (II) anions, forming the TiO_6 octahedron, as shown in **Figure 2.1**. The anatase phase shows obvious tetragonal distortion resulting in lower symmetry than the tetragonal crystal structure, whereas the rutile phase shows slightly tetragonal distortion, and brookite phase shows the orthorhombic structure. Generally, anatase and rutile phases are widely used in photocatalytic reactions whilst brookite phase receives limited research interest. Among the different polymorphs, rutile is generally considered to be the most stable phase, while anatase and brookite are considered to be more stable because of their lower surface energy that will transform to rutile when the temperature raised. The transformation of anatse to rutile is an irreversible process because the bond breaks and reforms to a new structure [130]. It was reported that the transformation occurs at between 673 and 873 K depending on the titanium precursor, preparation methods, and annealing atmospheres [131-134]. Most commercial titanium dioxide are a mixture of rutile and anatase, e.g. as known as Degussa P25 which contains 80-90% anatase and the balance is rutile. The properties of titanium dioxide phases are summarized in **Table 2.1**. As known, the optical band gap of anatase is reported about 3.2 eV and 3.0 eV in rutile and fast recombination of electron-hole pairs limit their wide photocatalytic applications. This properties can be improved by modifying with various elements to narrowing the band the optical band gad energy and/or to suppress electron-hole pair recombination.
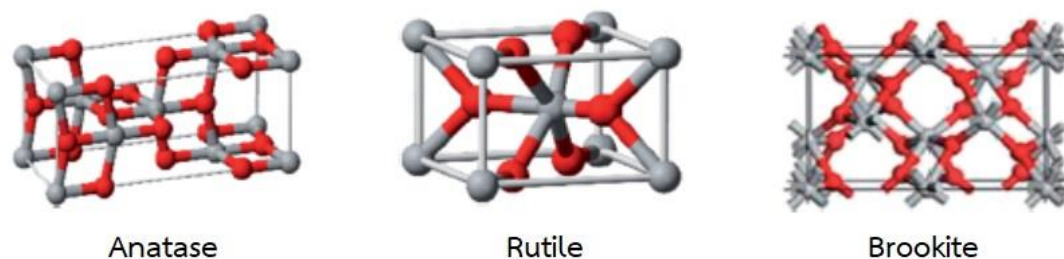
Figure 2.1 *Bulk structure of titanium dioxide phases [135]. (The grey and the red atoms represent titanium and oxygen, respectively.)*

Table 2.1 *Physical and structural properties of three titanium dioxide phases.*

Property	Anatase	Rutile	Brookite
Crystal system	Tetragonal	Tetragonal	Orthorhombic
Crystal size (nm)	< 11	> 35	11 - 35
Packing density (g/cm^3)	3.83	4.24	4.17
Lattice constants (nm)	a = b = 0.3785, c = 0.9514	a = b = 0.4594, c = 0.2959	a = c = 0.5436, b = 0.9166
Band gap (eV)	3.2	3.0	NA
Light adsorption (nm)	< 390	< 415	NA

2.2 The heterogeneous photocatalysis mechanism

In titanium dioxide photocatalysis studies, so far, the reactions between the pollutant molecules and the hydroxyl radical has been used for the reaction mechanism. The rate determining step of the whole reaction has been accepted as the transfer of conduction band electrons to the adsorbed oxygen. The general scheme of the photocatalysis, as shown if **Figure 2.2**, is based on the generation of electron (e^-) and hole (h^+) pairs upon irradiation with light by band-gap excitation that can initiate redox reactions on the titanium dioxide surface. In parallel, the electron migrates from the valence band to the conduction band, leaving behind a hole in the valence band. Surface defect sites (Ti^{3+}) trap electrons and its will be removed by reactions with adsorbed molecular oxygen to produce superoxide anion radical ($O2^{\bullet-}$). On the other hand, holes react with absorbed water molecules or hydroxide ions (OH^-) to produce hydroxyl radicals ($\bullet OH$), which is considered as the principal reactive species and the most important chemical process for the reactions. The hydroxyl radicals diffuse either in solution or on the titanium dioxide surface. Besides, electrons and holes can recombine and called as recombination process that is too fast, because of short charge separation distances in titanium dioxide. Organic pollutant molecules are generally composed of aromatic rings. It has been experimentally proven that hydroxyl radicals react with the aromatic ring in the molecules which then form intermediates. The final step in the photocatalysis process gives stable molecules such as carbon dioxide and water. The heterogeneous photocatalytic mechanism is a complex sequence of reactions that was widely postulated by the following simplified equations:

Photoexcition	$TiO_2 + h\nu$	--->	$e^-_{CB} + h^+_{VB}$	(2.1)
Charge carrier trapping of e^-	e^-_{CB}	--->	e^-_{TR}	(2.2)
Charge carrier trapping of h^+	h^+_{VB}	--->	h^+_{TR}	(2.3)
Electron-hole recombination	$e^-_{TR} + h^+_{VB} / h^+_{TR}$	--->	$e^-_{CB} + heat$	(2.4)
Oxygen ionosorption	$O_{2,\,ads} + e^-_{TR}$	--->	$O_2{\bullet}^-$	(2.5)

Water Dissociation	H_2O	--->	$H^+ + OH^-$	(2.6)
Neutralization of OH^-	$OH^-_{,ads} + h^+_{TR}$	--->	$OH\bullet$	(2.7)
Neutralization of $O_2\bullet^-$	$O_2\bullet^- + H^+$	--->	$HO_2\bullet$	(2.8)
Protonation of $O_2\bullet^-$	$O_2\bullet^- + OH\bullet$	--->	$HO_2\bullet$	(2.9)
Co-scavenger of e^-	$HO_2\bullet + e^-$	--->	HO_2^-	(2.10)
Formation of H_2O_2	$HO_2^- + H^+$	--->	H_2O_2	(2.11)
H_2O_2 Dissociation	$H_2O_2 + e^-$	--->	$OH\bullet + OH^-$	(2.12)
Photodagradation by $OH\bullet$	$R\text{-}H + OH\bullet$	--->	$R'\bullet + H_2O$	(2.13)
Photodagradation by h^+_{TR}	$R\text{-}COO^- + h^+_{TR}$	--->	$R' + CO_2$	(2.14)
Direct photoholes	$R + h^+_{TR}$	--->	$R^+\bullet + prod.$	(2.15)

Figure 2.2 *Photo-induced formation mechanism of electron-hole pair in a titanium dioxide particle with the presence of water pollutant (P) [136].*

The photodegradation reactions is known as one of the advanced oxidation processes. The main industrial application of titanium dioxide based photocatalysts is the degradation of dyes from the textile industry [137]. The photodegradation of organic compounds can occur not only on the surface of titanium dioxide but also in the liquid near the titanium dioxide surface. The factors that influence the photodegradation range from the choice of crystalline structure, the synthesis methods, the amount of photocatalyst, the pollutant concentration, and the experimental conditions, etc. Moreover, the surface property plays an important role in the photocatalytic process. Many reports realize the importance of surface hydroxylation, particularly, in titanium dioxide.

2.3 Titanium dioxide preparation methods

2.3.1 Solvothermal

The solvothermal method is a common method used to fabricate titanium dioxide and has been developed rapidly. This method is usually conducted in a stainless steel reactor with high temperature and pressure. This method generally uses titanium (IV) n-butoxide (TNB), and titanium (IV) chloride (TTC) as a titanium source and is conducted in an organic solvent. Various alcohols are used as both the solvents and the oxygen donors as well as the structural templates during the solvothermal synthesis of titanium dioxide-based nanomaterials such as methanol, ethanol, and butanediol [138]. The general mechanism could be expressed in the following reactions.

$$TiX_4 + 4R\text{-}OH \longrightarrow Ti(OR)_4 + 4HX;$$

$$Ti(OR)_4 + TiX_4 \longrightarrow 2TiO_2 + 4RX$$

$$2R\text{-}OH \longrightarrow R\text{-}O\text{-}R + H_2O$$

$$TiX_4 + 2H_2O \longrightarrow TiO_2 + 4HX$$
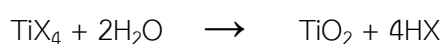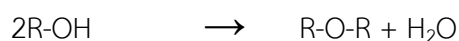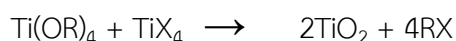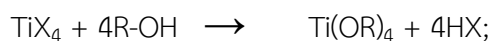
Both titanium dioxide precursors and alcohol solvents affect the morphological and structural properties as well as the crystallinity of titanium dioxide. The amount

of titanium precursor, reaction temperature, and holding time effects were reported. The findings showed that increasing reaction temperature and holding time resulted in an increase in the titanium dioxide crystallite size [51]. The main advantage of this method is the ability to grow high quality crystals while maintaining good control of their chemical structure. On the other hand, the disadvantages of using the solvothermal method were its need of expensive autoclaves due to the increase of the reaction pressure during the process and the impossibility of observing the crystal growth.

2.3.2 Sol-gel

The sol-gel method is used to prepare titanium dioxide in many forms, particles and thin film. Hydrolysis, condensation, polymerization, gelation, aging, drying and densification are involved in the sol-gel method [137]. Usually, the titanium precursor is used in the alkoxide form. This technique presents several advantages like homogeneity, low cost, reliability, reproducibility, and controllability. Negatively, this method requires a long period of deposition, high cost for fabrication, and high temperature to form anatase phase.

2.3.3 Hydrothermal

The hydrothermal method is one of the most used method for the fabrication of titanium dioxide. It is usually conducted in a Teflon or stainless steel reactor with additional temperature and high pressure inside the reactor. This method was first reported to treat titanium dioxide nanotubes at 383 K in a concentrated sodium hydroxide solution [139]. Since then, many studies have been carried out with different types of titanium dioxide. The hydrothermal method is a well-established technique and can synthesize titanium dioxide in just one single process. The effect of alkali concentration and temperature on Degussa P25 was investigated through an alkali hydrothermal treatment, the results showed that the morphological and structural properties of titanium dioxide can be transferred to each other by changing the hydrothermal conditions [140]. After that, the solution concentration, reaction temperature, reaction time effects were reported [141]. One of the disadvantages of

the hydrothermal method is the low reaction kinetics resulting in needing a long reaction time.

2.3.4 Sputtering

The sputtering process is a suitable technique for preparation of titanium dioxide thin films because it is cheap and provides good film adhesion. It allows uniformity in large area applications, high mechanical durability, and easy to control the physical, chemical and structural properties. Although metal titanium targets are used in the sputtering process is generally kept in the transition or oxide mode of sputtering in order to assure the stoichiometric content of oxygen atoms, which also induces significant decrease in the deposition rate [142]. Generally, argon was used as a noble gas in the sputtering chamber. The argon bombardment with the proper energy is reported to increase the growth and crystallization of the films [143].
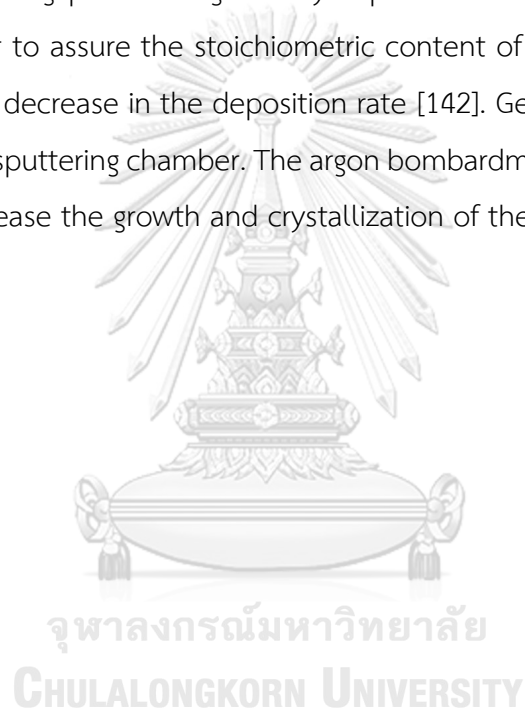
2.4 Titanium dioxide modification

Titanium dioxide is an n-type semiconductor with a large band gap, 3.2 eV, and adsorption in only the UV wavelength, <400 nm. Also, electrons and holes from photogeneration are recombined easily. Numerous methods have been made to improve these weak points of titanium dioxide. Doping with metal and/or non-metal elements to enlarge light adsorption and to suppress the electron-hole recombination have been reported frequently. This dissertation will focused on only three main elements to modify titanium dioxide i.e. silicon, nitrogen, and carbon.

2.4.1 Nitrogen modification

Recently, research showed that doping causes narrowing of the titanium dioxide band gap and results in carrier recombination [105, 144]. Doping titanium dioxide with elements such as nitrogen, carbon, and sulphur results in red-shift of the absorption edge, and are effective in enhancing the photocatalytic activity. The study of visible light activity for photocatalytic activity of nitrogen-doped titanium dioxide through first-principles calculations was reported [105]. They concluded that nitrogen doping improves the optical properties, and photocatalytic activity in both liquid and gas phase mediums. The predicted effects of doping on the band gap structure of titanium dioxide was reported by creating localized states and narrowing the band gap [105]. Moreover, the influence on photocatalytic activity of titanium dioxide by nitrogen substitution through DFT calculations was investigated [145]. They reported that the N *2p* localized states just above the O *2p* valence band caused red shift and blue shift in anatase and rutile, respectively.

Many researchers have studied the defect structure by theoretical analysis. According to the DOS calculations, nitrogen acts as the best dopant because of mixing its *p* states with O *2p*, states which causes band-gap narrowing [34]. The decrease of the band gap of titanium dioxide by the incorporation of nitrogen in the titanium dioxide lattice due to the formation of a new N 2p band above the O 2p valence band which was proposed in energy level diagrams in **Figure 2.3**.
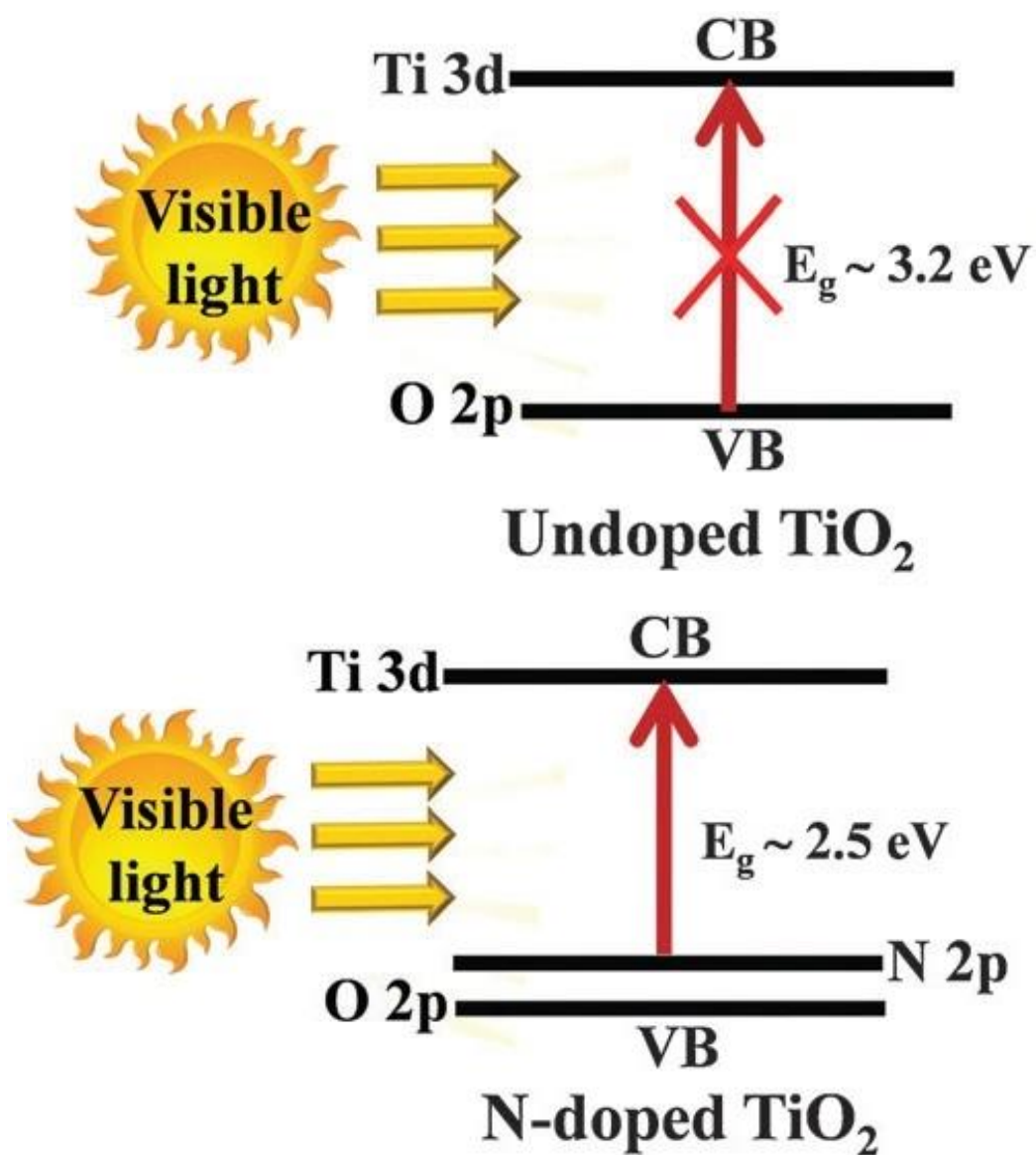
Figure 2.3 *Energy level diagrams of nitrogen-doped titanium dioxide compared to undoped titanium dioxide*

The possible reaction mechanism for the photocatalytic degradation of organic pollutants by nitrogen-doped titanium dioxide under visible light irradiation was shown in **Figure 2.4**, which showed the generation of electrons and holes in the conduction band and valence band, respectively, under visible light irradiation. Nitrogen doped titanium dioxide induces significant improvements in the optical adsorption and photocatalytic properties in the visible light region.
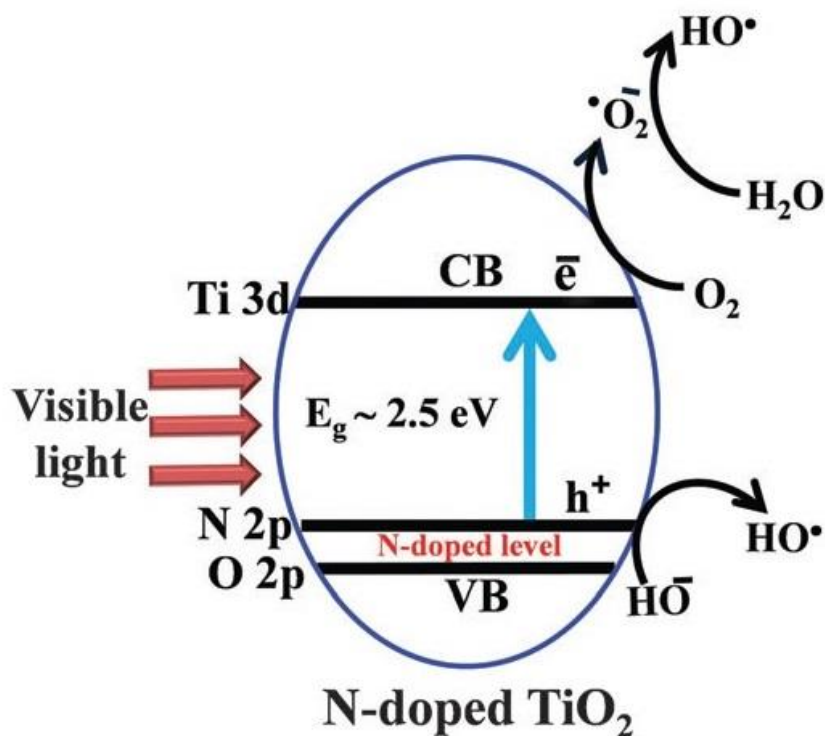
Figure 2.4 The possible reaction mechanism for the photocatalytic degradation of organic pollutants by nitrogen-doped titanium dioxide under visible light irradiation.

Despite, the literatures of the mode of nitrogen doping in titanium dioxide structure proposed either substitution or interstitial, which both play an essential role for its visible light photocatalytic activity. Substitution doping nitrogen leads to surface modification by the interactive forces, while interstitution doping nitrogen affects the titanium dioxide lattice structure [146]. The incorporation of nitrogen doped titanium dioxide was first reported by using a first principle calculation method [147]. The possible incorporation included both substitution and interstitial nitrogen [148]. Substitution doping nitrogen reduces the band gap but less that that achieve by interstitial doping nitrogen as proposed in **Figure 2.5**. Many studies have shown that an incorporation of both substitution and interstitial doping nitrogen generally occurs, and both play a crucial role in visible light photocatalysis.
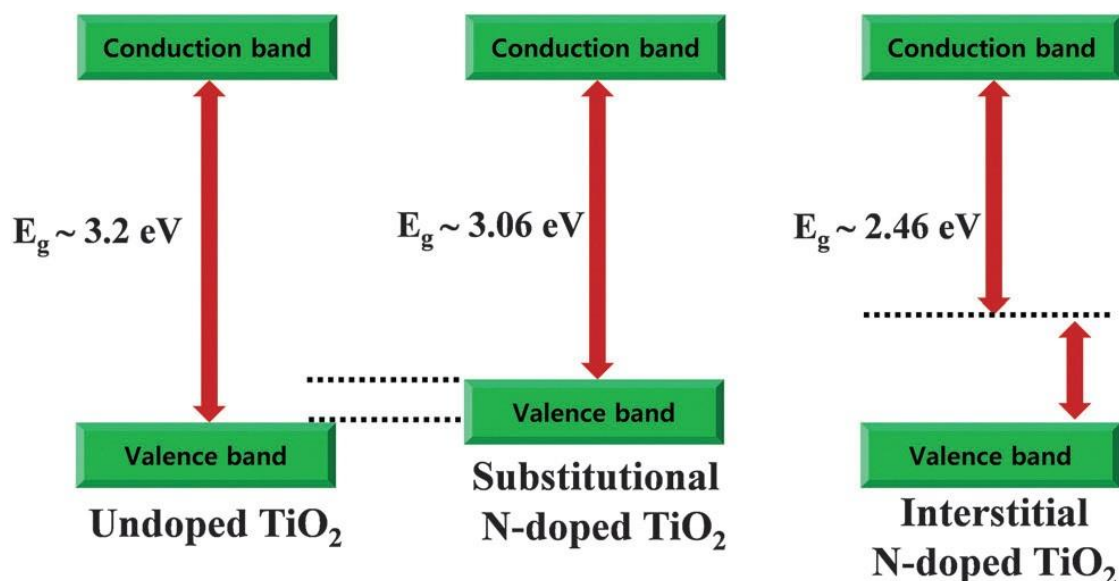
Figure 2.5 *Schematic diagram showing the valence and conduction bands of undoped and nitrogen-doped titanium dioxide*

Recently, the doping of nitrogen into titanium dioxide lattices have used both physical and chemical methods, which include solvothermal method, sol-gel method, flame spray pyrolysis, sputtering and ball milling. The most commonly used and efficient method is the synthesis of nitrogen doped titanium dioxide in a nitrogen environment. **Table 2.2** lists the various synthesis methods for preparing nitrogen-doped titanium dioxide and the sources of nitrogen for photocatalysis applications.

The different types of the titanium dioxide precursor and the nitrogen sources might also result in the different of physical and chemical properties. Most of publications of nitrogen-doped titanium dioxide have confirmed its visible light photocatalytic activity. However, the loss of nitrogen-doped titanium dioxide due to annealing may also be one of the most important concern and that results in decreased photocatalytic activity. Therefore, in order to prepare nitrogen-doped titanium dioxide with high photocatalytic efficiency, the annealing in nitrogen atmosphere in synthesis method should be studied in such a way that avoids the loss of nitrogen. The various titanium dioxide methods for producing nitrogen-doped titanium dioxide by annealing under nitrogen atmosphere have been published such as, atmospheric pressure plasma [149], electrospinning [150], polymeric precursor

method [151], radio frequency magnetron sputtering [152], and sol-gel [153]. After the author searched the literatures, the annealing of titanium dioxide under nitrogen atmosphere that prepared by solvothermal method has not been done yet.

Table 2.2 *The various synthesis methods for preparing nitrogen-doped titanium dioxide and the sources of nitrogen for photocatalysis applications.*

Preparation method	Nitrogen source	Ref.
Anodic oxidation	TiN alloy	[154]
Atomic layer deposition	Ammonia (NH_3)	[155]
Ball milling	Ammonia (NH_3)	[156]
Chemical vapour deposition	Ammonia (NH_3)	[157]
Electrospinning	Ammonium acetate ($C_2H_7NO_2$)	[158]
Hydrothermal	Urea (CH_4N_2O)	[159]
Microemulsion	Triethylamine ($C_6H_{15}N$)	[160]
Microwave	Ammonia (NH_3)	[161]
Sol-gel	Ammonia (NH_3)	[162]
Solvothermal	Ethylenediamine ($C_2H_8N_2$)	[163]
Sputtering	Nitrogen gas	[164]

2.4.2 Nitrogen-Silicon modification

In recent years, some groups have made an attempt to improve the photocatalytic activity of titanium dioxide and extend its optical absorption to visible-light region by preparing silicon-doped titanium dioxide [165-168]. It has been reported that silicon-doped titanium dioxide photocatalysts were an effective way to improve the photocatalytic capability, thermal stability, quantum-sized effect, good surface wettability and mechanic strength [169]. For example, the publication reported that a small amount of silicon-dopant could improve the photocatalytic activity of titanium

dioxide [165]. It has been suggested that the substitution of silicon may favour photocatalytic activity and the optical absorption is broadening to longer wavelength by UV–vis diffuse reflectance spectra measurement [166]. Modification with silicon showed large surface areas and superior thermal stabilities by insertion of the distorted octahedral vacant sites of the titanium dioxide structure [170, 171]. Silicon-doping has an effect on the photocatalytic activity by increasing the surface area and crystallinity through embedding amorphous silica into titanium dioxide [172]. The silicon doping effects on the electronic structures and optical properties of titanium dioxide have been studied by spin-polarized density functional theory calculation based on the plane-wave method [173]. The results indicate that the substitution by silicon has a band gap narrowing of about 0.25 and the decrease of electron transition energy from the valence band to conduction band may be responsible for the visible-light optical absorption properties.

However, it is generally believed that doping with two anion acceptors would repel each other. In particular, the effects of nitrogen-silicon-codoped titanium dioxide found that hybridization between the codoped states and O *2p* orbitals leads to broadening of the valence band and improvement in mobility of holes by first principles calculation [174]. **Figure 2.6** showed the plausible locations of nitrogen and silicon atoms in titanium dioxide structure after codoping process [175].
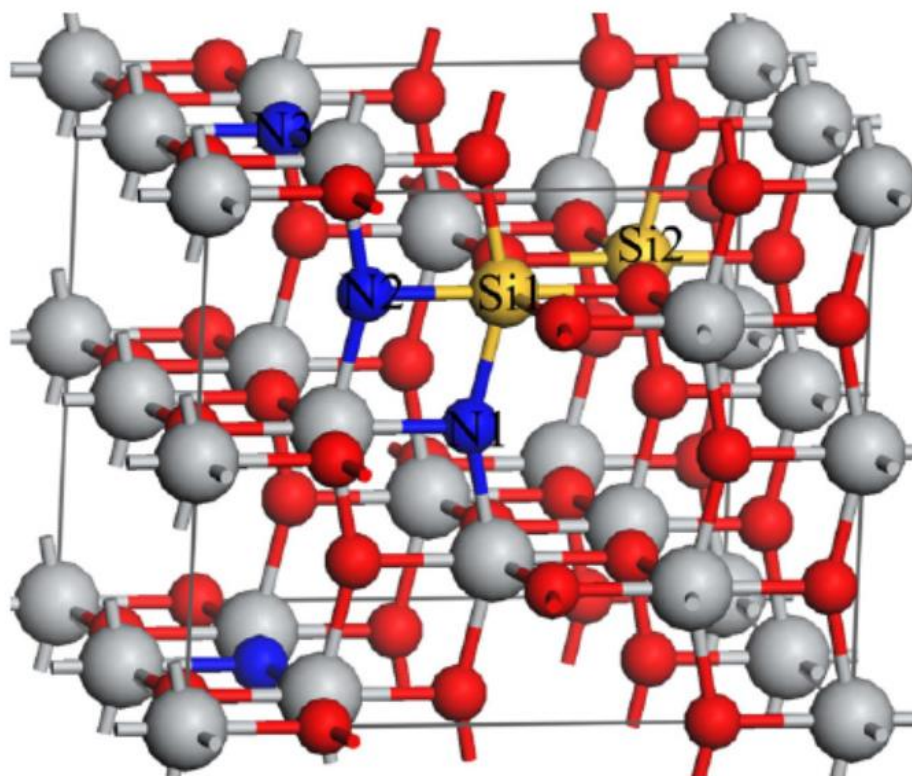
Figure 2.6 *Plausible locations of nitrogen and silicon atoms in titanium dioxide structure. The N ions' doping sites are marked by N1, N2 and N3 while Si ions' doping sites are denoted by Si1 and Si2. The grey, red, blue and yellow spheres represent Ti, O, N and Si atoms, respectively [175].*

2.4.3 Modification by amino-silane

Surface modification with alkylsilanes is one of the most commonly used methods to prepare monolayers on oxides. Reactions of organosilanes with OH-bearing surfaces have found use in widely diverse areas. The main advantage of using silanes for monolayer formation on oxidic surfaces is the rapid formation of a covalent linkage between the substrate and the anchoring group [176, 177]. This covalent bond stabilizes the monolayer, and also allows for easy further chemical modification without compromising the integrity of the monolayer.

The initial hydrolysis of Si-Cl or Si-OR bonds thus generates the hydroxysilane that makes self-assembly monolayer (SAM) possible. This step is probably the most critical and controls the final quality and morphology of the SAM. The frequently

experienced difficulties in reproducibly making high-quality monolayers relate to this step, as incomplete hydrolysis or excessive hydrolysis result in incomplete monolayers or formation of polysiloxanes on the surface, respectively. This also means that surfaces that do not contain adsorbed water molecules react poorly, like metal oxides without –OH groups, or silicon, carbon, and organic polymers, which explains their position on the silane reactivity scale indicated in **Figure 2.7**. If an insufficient density of surface -OH groups is a problem, then plasma activation will form sufficient hydroxy moieties for the formation of highly stable high-quality monolayers, even on plastics such as poly(methylmethacrylate (PMMA) and polystyrene.
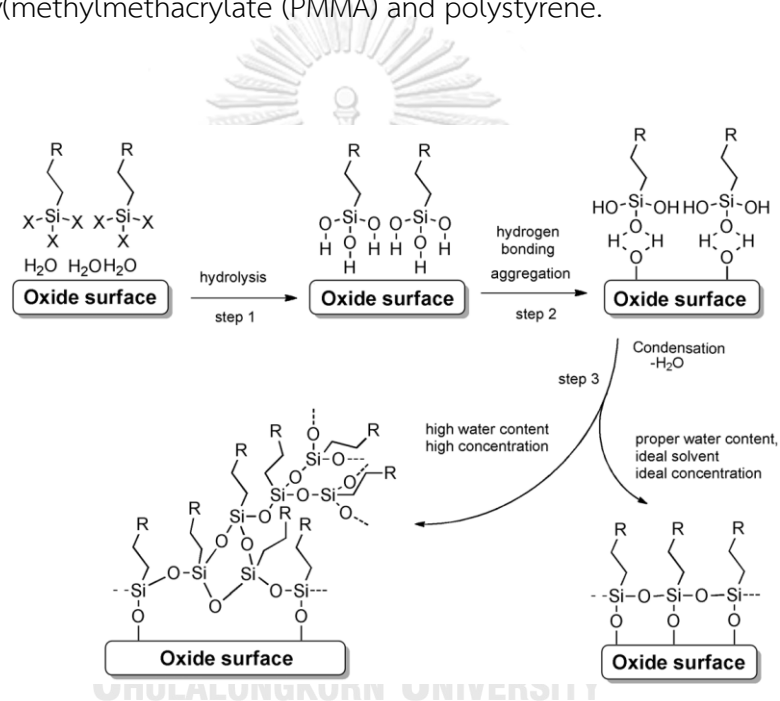
Figure 2.7 Three-step mechanism for monolayer formation by silanes on OH terminated surfaces [178].

The different ways in which silanes can be bound to the surface can be distinguished by a variety of techniques. Residual chloride or methoxide moieties would typically be recognizable by for example, IR or X-ray photoelectron spectroscopy (XPS). For the direct observation of the interfacial Si-O bond formation, IR spectroscopy has been shown to be especially useful. Self-assembled monolayer (SAM) formation on SiO_x can be monitored by the longitudinal optical (LO) absorption band that arises from the vibrations perpendicular to the surface of Si-O bonds at the

SAM/SiO$_2$ interface. In particular, this analysis of the 950 to 1255 cm^{-1} range that includes surface bound and internally cross-linked Si-O-Si vibrational modes, can distinguish between silanes that form a strong chemisorbed bond to the surface and weakly adsorbed polysilanols [179].

2.4.4 Atom Transfer Radical Polymerization (ATRP)

Atom transfer radical polymerization (ATRP) is an example of a reversible-deactivation radical polymerization. Like its counterpart, ATRA or atom transfer radical addition, it is a means of forming a carbon-carbon bond through a transition metal catalyst. As the name implies, the atom transfer step is the key step in the reaction responsible for uniform polymer chain growth. ATRP was independently discovered in 1995 [180].

ATRP usually employs a transition metal complex as the catalyst with an alkyl halide as the initiator (R-X). Various transition metal complexes, namely those of Cu, Fe, Ru, Ni, Os, etc., have been employed as catalysts for ATRP. In an ATRP process, the dormant species is activated by the transition metal complex to generate radicals via one electron transfer process. Simultaneously the transition metal is oxidized to higher oxidation state. This reversible process rapidly establishes an equilibrium that is predominately shifted to the side with very low radical concentrations. The number of polymer chains is determined by the number of initiators. Each growing chain has the same probability to propagate with monomers to form living/dormant polymer chains. As a result, polymers with similar molecular weights and narrow molecular weight distribution can be prepared.

ATRP reactions are very robust in that they are tolerant of many functional groups like allyl, amino, epoxy, hydroxy and vinyl groups present in either the monomer or the initiator. ATRP methods are also advantageous due to the ease of preparation, commercially available and inexpensive catalysts (copper complexes), pyridine based ligands and initiators (alkyl halides).

CHAPTER III

EXPERIMENTAL

3.1 Catalyst Preparation

3.1.1 Nitrogen-Silicon-codoped titanium dioxide via solvothermal method

Synthesis of titanium dioxide and nitrogen-silicon-codoped titanium dioxide was carried out by a solvothermal method using titanium (IV) n-butoxide (TNB, Aldrich) as a titanium source. The silicon-doped titanium dioxide was prepared by adding an appropriate amount of tetraethylorthosilicate (TEOS, Aldrich) into the starting solution of 15 g TNB as a silicon precursor. The precursor solution was dissolved in 100 ml of 1,4-butanediol (Aldrich) in a test tube and then placed in 300 ml autoclave. The gap between the test tube and the autoclave wall was filled with 30 ml of the 1,4-butanediol. The autoclave was purged completely using nitrogen before being heated up to 573 K at a rate of 2.5 K/min. The autoclave was held at that temperature for 2 hours. After the autoclave was cooled to room temperature, the product powders obtained in the test tube were washed repeatedly with methanol and dried in air. The powder was annealed in different atmospheric gas flows including oxygen, air, and nitrogen at 723 K for 2 hours to obtain nitrogen-silicon-codoped titanium dioxide in this experiment.

3.1.2 Nitrogen-Silicon-codoped titanium dioxide via sol-gel method

Titanium dioxide and nitrogen-silicon-codoped titanium dioxide were prepared using the sol-gel method. Titanium isopropoxide (Aldrich Chemical, Milwaukee, WI) was employed as a titanium precursor. First 14.4 ml of concentrated nitric acid was added to 2,000 ml of de-ionized (DI) water. While the acidic solution was stirred, 166.8 ml of titanium isopropoxide was added slowly. The suspensions were stirred continuously at room temperature for 3 days until clear sol was obtained. After that, the sol was dialyzed in a cellulose membrane with a molecular weight cut-off 3,500 Daltons (spectrum Companies, Gardena, CA). The dialysis tubing was washed in DI water, which

was changed daily for 3-4 days until the pH of the water reached 3.5. In order to prepare the silicon-doped titanium dioxide, the sol of titanium dioxide and tetraethyl orthosilicate (TEOS) was mixed and the mixture was stirred continuously at room temperature for 2 hours. The dialyzed sol was dried at 383 K to remove the solvent. The resulting gel was then grounded. Finally, the obtained samples were annealed in different gas flows including oxygen, air, and nitrogen at 723 K for 2 hours to obtain nitrogen-silicon-codoped titanium dioxide in this experiment.

3.1.3 Modification of titanium dioxide by APTES

In this experiment, the concentrations of 3-aminopropyltriethoxysilane (APTES, >98% purity from Fluka) in anhydrous toluene (>99.5% purity from Fisher Chemical) were investigated at 0.1, 1.0, and 10 mM. Typically, 7.0 g of titanium dioxide powder (Commercial Degussa P25 catalyst from AEROXIDE®) was dispersed in 75 mL of APTES solution using Teflon reactor and stirred at room temperature for an hour. After that, the Teflon reactor was heated at 373 K for 12 h, and then the powder was washed with toluene once and dichloromethane (from Carlo Erba) twice for removing any residual chemicals. Finally, powder was dried in oven at 383 K for 12 hr. The powder nomenclatures were represented as 0.1 mM APTES-TiO$_2$, 1.0 mM APTES-TiO$_2$ and 100 mM APTES-TiO$_2$ respectively.

3.1.4 Carbon-doped titanium dioxide thin films via sputtering method

In this part the carbon-doped titanium dioxide thin films were prepared using a Teer Coatings UDP350 reactive pDC magnetron sputtering system (Teer Coatings Ltd., Droitwich, UK), without additional heating applied to the substrate. A schematic diagram of the rig is shown in **Figure 3.1**. In brief, the sputtering rig was fitted with a 300 mm x 100 mm directly cooled titanium metal target (99.5% purity) mounted onto a type II unbalanced planar magnetron, installed through the chamber wall. The titanium metal target was driven in pulsed DC mode using a dual channel power supply (Advanced Energy Pinnacle Plus, Fort Collins, CO, USA), at 100 kHz pulse frequency,

and a duty cycle of 50%. The base pressure of the vacuum chamber before sputtering was 2.0×10^{-5} mbar or lower. All titanium dioxide films were deposited onto soda lime glass substrate materials. The substrates were ultrasonically pre-cleaned in propanol prior to deposition (all reagents used in this work were purchased from Sigma Aldrich, unless stated otherwise) and mounted on the rotatable substrate holder at 10 cm separation from the titanium target. During the sputtering process, the substrate holder was rotated at a speed of 10 rpm. The titanium metal target power was fixed at 1000 W for each run; the target was pre-sputtered in an argon plasma for 10 min prior to the deposition process to remove any oxide layer on the target surface (with the substrates shielded from the target), and the reactive sputtering time for each run was 2 h. The deposition runs were carried out in an argon/oxygen and argon/oxygen/carbon dioxide plasma for undoped and carbon-doped titanium dioxide films, respectively. The argon flow was controlled by a mass flow controller and set at 15 sccm. The oxygen flow was controlled by optical emission monitoring (OEM) at three different set points of 25%, 30%, and 35% of the full metal signal (FMS). To vary the carbon concentration, the carbon dioxide flow rate was varied by the mass flow controller at different flows of 2.5, 5, and 7 sccm. The coatings were post-deposition isothermally annealed for 30 min at 873 K in air for crystal structure development and then allowed to cool gradually in air for 10–12 h to avoid the formation of thermal stresses in the coatings.
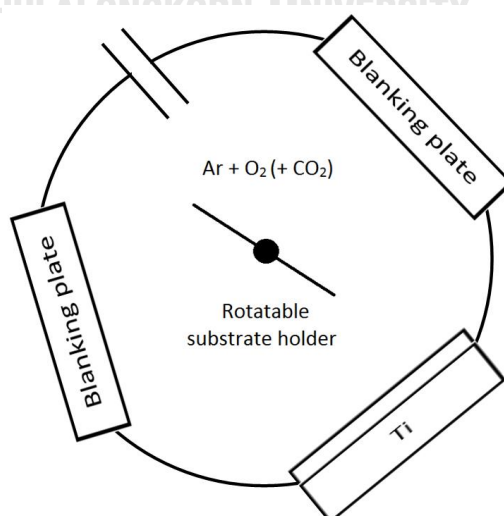
Figure 3.1 *Schematic representation of the Teer UDP350 sputtering rig.*

3.1.5 Grafting of titanium dioxide onto PMMA film via ATRP

3.1.5.1 Materials

Tetrahydrofuran (THF, Unilab) was refluxed over sodium (Na, Sigma-Aldrich) in a column under an inert gas. Triethylamine (TEA, Sigma-Aldrich) was distilled over calcium hydride (CaH$_2$, Fluka) in a column under an inert gas. Methyl methacrylate (MMA, Sigma-Aldrich) was purified with sodium hydroxide (NaOH, Merck) three times and sodium sulphate (Na$_2$SO$_4$, LobaChemie) before use. Polymethyl methacrylate films (PMMA, KTV), commercial titanium dioxide (AEROXIDE), 3-(trimethoxysilyl)propyl methacrylate (MEMO, stabilized with butylated hydroxytoluene, TCI-Tokyo), 4-hydroxybenzenethiol (4HBT, TCI-Tokyo), 4-dimethylaminopyridine (DMAP, Sigma-Aldrich), 2-bromoisobutyryl bromide (BIBB, TCI-America), dichloromethane (CH$_2$Cl$_2$, Sigma-Aldrich), sodium hydrogen carbonate (NaHCO$_3$, Sigma-Aldrich), magnesium sulphate (MgSO$_4$, Panreac), copper (I) bromide (CuBr, Sigma-Aldrich), 2,2'-bipyridyl (BPY, Sigma-Aldrich), methanol (CH$_3$OH, Qrec), sulfuric acid (H$_2$SO$_4$, Qrec), ethanol (C$_2$H$_5$OH, Merck), ammonium hydroxide (NH$_4$OH, Sigma-Aldrich), dimethyl sulfoxide (DMSO-d_6, CIL) and methylene blue (Unilab) were used without further purification.

3.1.5.2 Preparation of hydroxyl-end group by thiol-ene click Michael addition

The hydroxyl-end group on MEMO was prepared by thiol-ene click Michael addition as shown in **Figure 3.2**. 4HBT (8.6 g), MEMO (15 mL), dry THF (15mL) and purified TEA (4.5 mL) were stirred under an inert gas for 48 hours until a crude, slightly yellow product was obtained [181]. The product solution was named MEMO-OH.
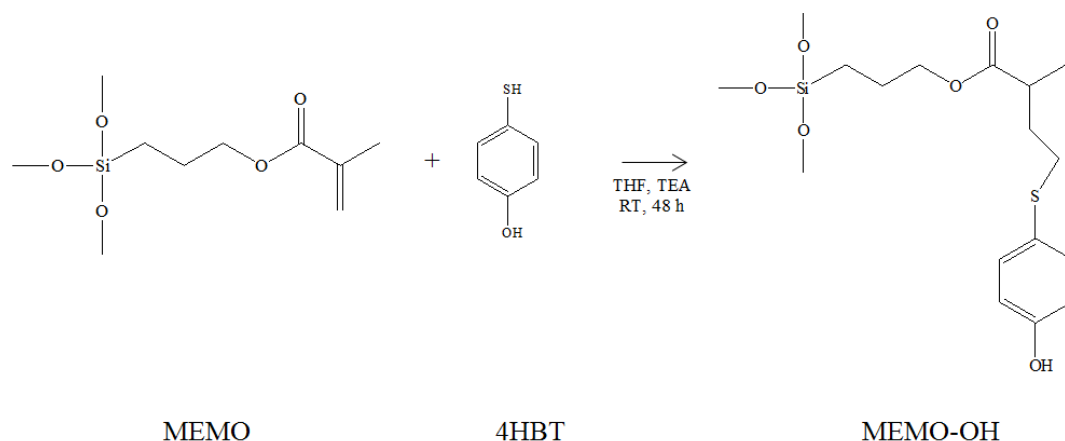
Figure 3.2 *Hydroxyl-end group by thiol-ene click Michael addition*

3.1.5.3 Preparation of bromide-end group by macroinitiator formation

The bromide-end group on MEMO was prepared by macroinitiator formation, as shown in **Figure 3.3**. The preparation of MEMO-Br was then performed after MEMO-OH was obtained. First, DMAP (0.13 g) and MEMO-OH were stirred in a two-necked, round bottom flask under an inert gas and equipped with a condenser until the DMAP was dissolved. Next, purified TEA (0.5 mL) was injected into the solution and the temperature was cooled to 273 K in an ice bath. Then, BIBB (8.1 mL) was slowly dropped into the flask by a gas tight syringe, stirred overnight and evaporated using THF until a crude, slightly white product was obtained. Next, CH_2Cl_2 (100 mL) was mixed into the crude product and dissolved until a homogeneous solution was obtained. The solution was washed with $NaHCO_3$ five times and with deionized water once. Then, the solution was dried overnight with $MgSO_4$ until the CH_2Cl_2 was evaporated and filtered [182]. The final solution was named MEMO-Br.

MEMO-OH   BIBB   MEMO-Br
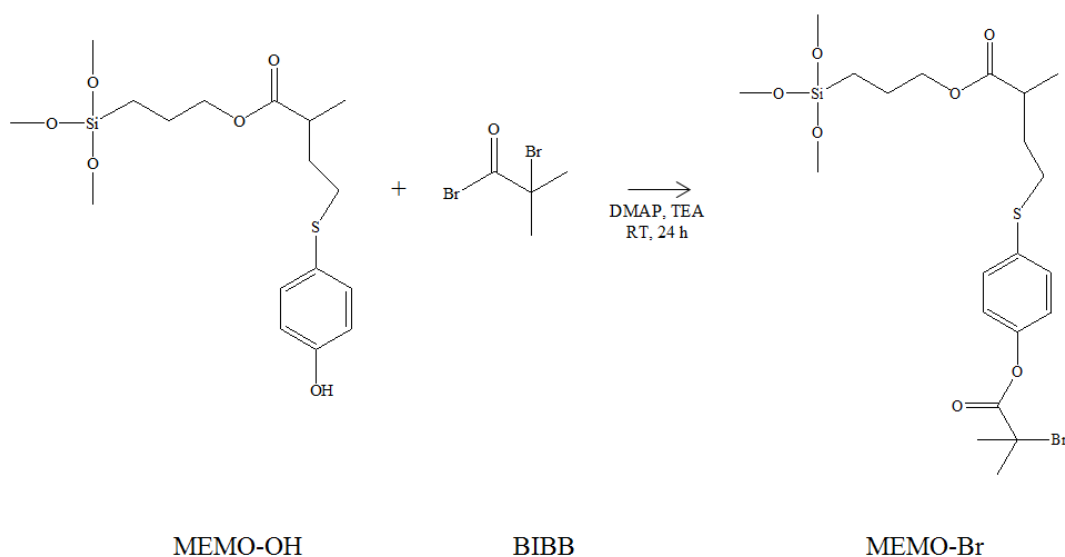
Figure 3.3 Bromide-end group by macroinitiator formation

3.1.5.4 Preparation of polymer surface initiated by ATRP

The polymer surface initiation was prepared by ATRP, as shown in **Figure 3.4**. The MEMO-Br solution was stirred with CuBr (0.24 g), BPY (0.34 g) and methanol (18 mL) under an inert gas. Then, the purified MMA was injected into the solution for 8 hours [183]. The final product was named MEMO-PMMA-Br.

MEMO-Br   MMA   MEMO-PMMA-Br
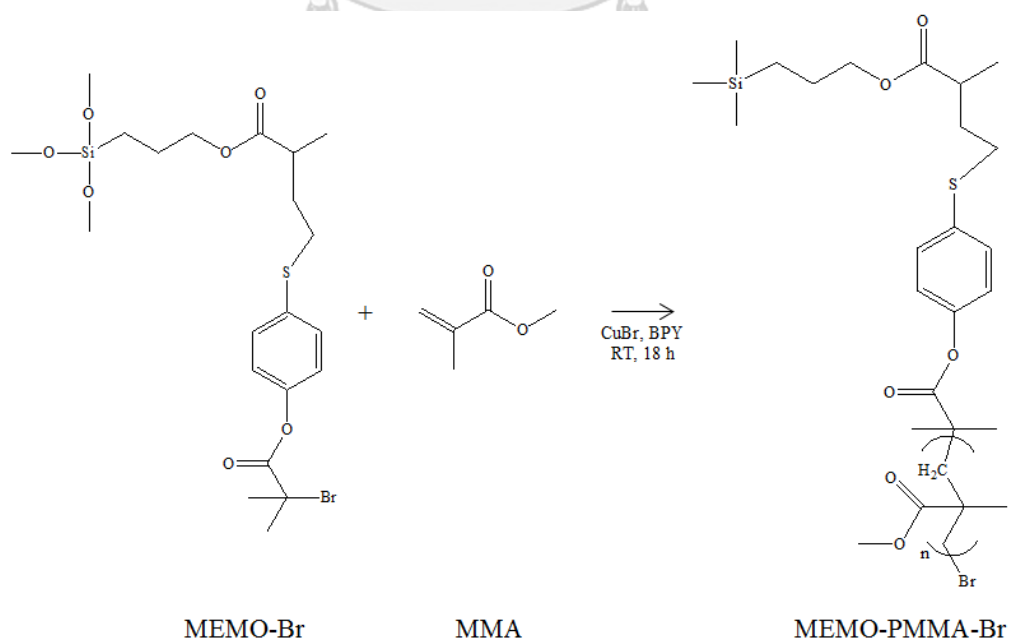
Figure 3.4 Polymer surface initiated by ATRP

3.1.5.5 Preparation of monomer grafted onto polymer film by ATRP

The MMA monomer was grafted onto the PMMA films by ATRP, as shown in **Figure 3.5**. MEMO-PMMA-Br solution (1 mL) was mixed with THF (2 mL) before being sprayed on PMMA film. Next, the PMMA film was hydrolyzed in deionized water with an adjusted pH of 2-3 with H_2SO_4 for 30 minutes before it was dried at room temperature. The PMMA film was named PMMA-g-MEMO-PMMA-OH.

MEMO-PMMA-Br   PMMA-g-MEMO-PMMA-Br
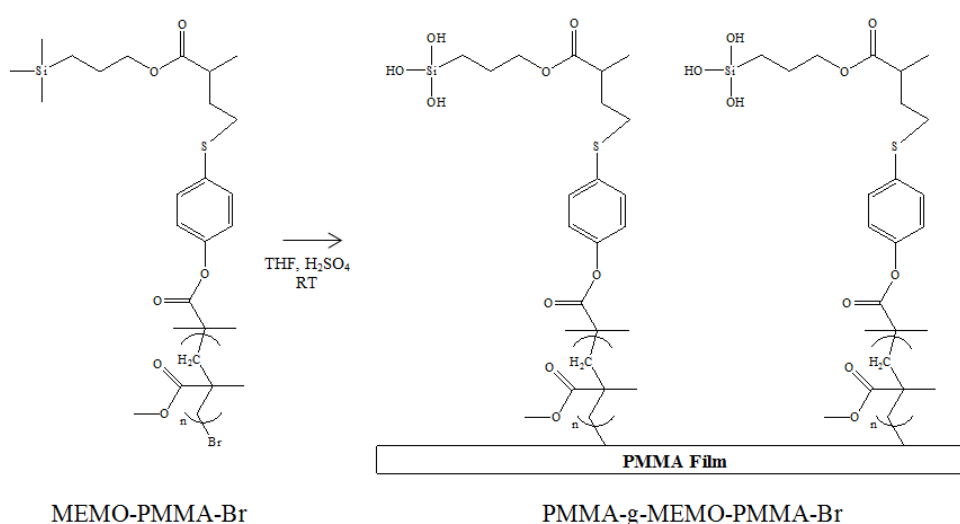
Figure 3.5 *Monomer grafted onto polymer film by ATRP*

3.1.5.6 Preparation of titanium dioxide particles grafted onto Polymer Film

Commercial titanium dioxide catalyst was sourced as a powder to graft onto the PMMA film, as shown in **Figure 3.6**. Titanium dioxide (1 g) was mixed in ethanol (100 mL) with an adjusted pH of 10-11 with NH_4OH [184]. Then, the PMMA-g-MEMO-PMMA-OH film (10 x 20 cm) was placed in the solution and sonicated one and a half hour. The film was washed with ethanol. Finally, the film was dried overnight at room temperature and named TiO_2-g-PMMA.
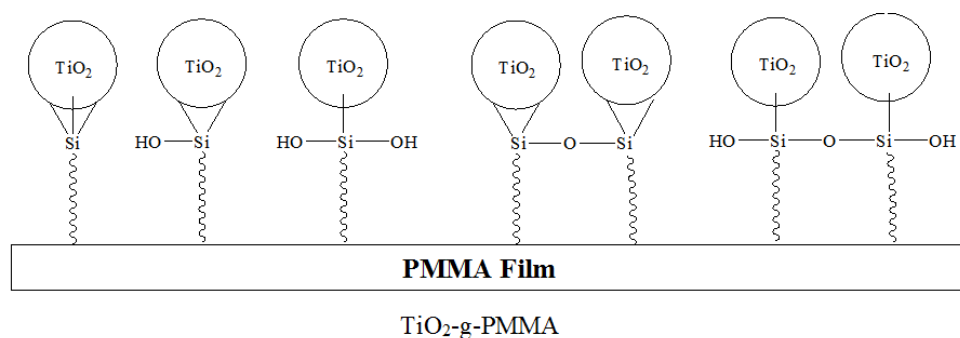
Figure 3.6 *Titanium dioxide particles grafted onto Polymer Film*

3.2 Characterisations

3.2.1 Characterisations for Section 4.1

The XRD measurements were performed with a Siemens D5000 X-ray diffractometer using Ni filtered CuKα radiation. The crystallite size (d_{XRD}) was calculated using the Scherrer equation. The XPS analysis was performed using an AMICUS photoelectron spectrometer equipped with a Mg Kα X-ray as a primary excitation and KRATOS VISION2 software. XPS elemental spectra were acquired using 0.1 eV energy step at a pass energy of 75 eV. The C *1s* line was taken as an internal standard at 285.0 eV. The morphology of the titanium dioxide particles samples were obtained using the JEOL JEM-2010 transmission electron microscope operated at 200 kV with an optical point to point resolution of 0.23 nm. EDX observation with a JSM-5410LV Scanning Microscope was employed to investigate the chemical composition of titanium dioxide. The UV-VIS was examined with VARIAN CARY 5000 instrument. The unpair electron in titanium dioxide photocatalyst was investigated by electron spin resonance (ESR) JEOL model JES-RE2X with using of DPPH for g value calibration.

3.2.2 Characterisations for Section 4.2

All powder characterizations were investigated at room temperature. The X-ray diffraction (XRD) was evaluated by D8 Advance Bruker AXS X-ray diffractometer and CuKα radiation with Ni filter. The BET surface area, pore volume, and average pore size diameter was measured through nitrogen gas adsorption using Micromeritics ASAP 2020

instrument. The ultraviolet–visible spectroscopy (UV-vis) was performed by using VARIAN CARY 5000 spectrophotometer. The X-ray photoelectron spectroscopy (XPS) was performed by using an AMICUS photoelectron spectrometer equipped with MgKα X-ray as a primary excitation and with using C *1s* as a calibration peak at 285.0 eV. The thermal gravimetric analysis (TGA) was investigated by the SDT Q600 instrument under air flow of 400 mL/min with the heating rate of 283 K/min. Photoluminescence (PL) was examined using the Perkin Elmer LS 55 and using Xenon lamp source excitation at 325 nm. Scanning electron microscopy with energy dispersive X-ray spectroscopy (SEM-EDX, model JSM-5410LV scanning microscope) was employed to investigate the elemental composition of APTES-modified titanium dioxide. Total organic carbon (TOC) of reaction was determined by using TOC-V$_{CSH}$ Shimadzu.

3.2.3 Characterisations for Section 4.3

The film thickness was measured via a Dektak™ stylus profilometer (Bruker, Billerica, MA, USA). The surface images of the coatings were obtained with scanning electron microscopy (SEM) (JEOL JSM-5410LV scanning microscope) (JEOL, Peabody, MA, USA). The micro structure and crystallinity of the thin films were investigated with a Panalytical Xpert powder X-ray diffractometer (XRD) (PANalytical Ltd., Cambridge, UK) operating with Cu Kα1 radiation at 0.154 nm in grazing incidence mode at a 3° angle of incidence, over a scan range from 20° to 70° 2θ and the accelerating voltage and applied current were 40 kV and 30 mA, respectively. The bulk composition of the thin films was characterized by energy dispersive X-ray spectroscopy (EDX, JEOL model JSM-5410LV scanning microscope) (JEOL, Peabody, MA, USA). The Ti *2p*, O *1s*, and C *1s* core levels on the surface were measured by X-ray photoelectron spectroscopy (XPS) to examine the surface composition, electron binding energy, and bonding sites on the thin films. The XPS analysis was performed using an AMICUS photoelectron spectrometer (Kratos Analytical Ltd., Manchester, UK) equipped with an Mg Kα X-ray as the primary excitation source. The binding energy was referenced to the Ag *3d* line at 368.2 eV for calibration. Curve fitting was performed using a Gaussian function with a Shirley background. The surface topography of the films was studied using atomic

force microscopy (AFM) (Veeco, Plainview, NY, USA), specifically a Veeco NanoScope IV MultiMode AFM. The transmission data of the coatings were obtained using an Ocean Optics USB4000 UV-Visible spectrometer (Ocean Optics Inc., Oxford, UK), which was used in turn to evaluate the band gap energy according to the Tauc plot method. The photoinduced wettability was evaluated at ambient temperature by analyzing the change in the water contact angles using a Theta Lite optical tensiometer (Biolin Scientific, Manchester, UK), while irradiating with UV light or visible light (identical to the light sources used for the methylene blue degradation described in the latter section). Prior to the experiments of contact angle measurements, the thin films were kept in the dark for 24 h.

3.2.4 Characterisations for Section 4.4

Fourier transform infrared spectroscopy (FT-IR) was used to measure the functional formation on a Nicolet in the range of 500-4000 cm^{-1}. The X-ray photoelectron spectroscopy (XPS) analysis was performed using an AMICUS photoelectron spectrometer equipped with an MgKα X-ray as a primary excitation source and KRATOS VISION2 software to measure the composition of elements on the polymer surface. ^{1}H NMR and ^{13}C NMR spectra using nuclear magnetic resonance spectroscopy (NMR) were recorded with a Bruker 400 Ultra Shield. The samples were dissolved in DMSO-d_6 and ran under room temperature. The differential scanning calorimetry (DSC) (SDT Q600 instruments) was used under a nitrogen flow of 400 mL/min and a heating rate of 283 K/min. Transmission electron microscopy (TEM) was obtained to investigate the morphology of particles grafted onto the polymer using the JEOL JEM-2100 electron microscope. Scanning electron microscopy with energy dispersive X-ray spectroscopy (SEM-EDX, model JSM-5410LV scanning microscope) was employed to investigate the morphology and the composition of particles grafted onto the polymer. The UV–Vis spectroscopy (VARIAN CARY 5000 instrument) was used to determine the residual colour of the methylene blue solution after the photocatalytic reaction.

3.3 Photocatalysis degradation studies

3.3.1 Photodegradation of methylene blue for nitrogen-silicon-codoped titanium dioxide

The photocatalytic degradation reaction was conducted at room temperature under UV light (Mercury Lamp 500W, Philips) and visible light (Metal halide Lamp 250W which consist of 90% visible light, Philips) with the average light intensity on the reaction beaker (pyrex). The reaction was carried out with 30 mg of catalyst dispersed in 200 ml of 20 ppm methylene blue aqueous solution. The reaction was operated with a high stirring rate (500 rpm) to avoid the mass transfer effect. Prior to irradiation, the suspensions were magnetically stirred in the dark for 15 min and 1.5 ml samples were withdrawn every 15 min. Before analysis, the aqueous samples were centrifuged to remove any suspended solid catalyst particles. The residual concentration of methylene blue was measured at 665 nm using the UV–vis spectrophotometer in liquid cuvette configuration, using DI water as reference.

3.3.2 Photodegradation of methylene blue for APTES surface modification

The 400 ml of methylene blue aqueous solution 20 ppm was carried out in reactor with 0.06 g of titanium dioxide catalyst. The suspensions were magnetically stirred in the dark for 15 minute before visible light radiation (MASTER TL-D Eco 16W/840 1SL, which consist of 97% visible light). The methylene blue decolourisation was evaluated based on the adsorption of UV-Vis spectra at 665 nm.

3.3.3 Photodegradation of methylene blue for carbon-doped titanium dioxide thin films

The photocatalytic properties of the series of thin films deposited with different carbon concentrations were evaluated under UV and visible light illumination. For photocatalytic oxidation of methylene blue, samples of the same geometrical size (1.5 × 2.5 cm^2) were immersed in 40 mL conditioning solution of methylene blue

(concentration 1.5 **μ**mol/L) in the dark at room temperature for 30 min to reach the adsorption-desorption equilibrium. The samples were then withdrawn from the conditioning solution and immersed into 40 mL of testing solution (concentration 1.5 **μ**mol/L—pre-defined experimentally to detect the photocatalytic responses of all samples in a 1-hour experiment) with continuous magnetic stirring, while being irradiated with either UV or visible light for a total time of 1 h. During irradiation, the absorbance of methylene blue at 664 nm was monitored continuously with an Ocean Optics USB4000 spectrometer for one hour. Each coating was tested both under UV and visible light; 2×15 W 352 nm Sankyo Denki BLB lamps were used as the UV light source, while visible light was simulated by combining a fluorescent light source ($2 \times$ 15 W Ushio fluorescent lamps) with a Knight Optical 395 nm long pass UV filter. A series of reference tests was performed prior to the photocatalytic activity measurements, which included tests with blank samples (soda-lime glass of the same geometrical size) under each light source, as well as tests of each sample in dark conditions, to prove that solution decolourization was caused by a photocatalytic reaction. As none of the reference tests showed more than 1% peak height decay in a 1 h experiment, their effect was neglected in further calculations.

3.3.4 Photodegradation of stearic acid for carbon-doped titanium dioxide thin films

The stearic acid decomposition test was used for verification of the dye degradation results in this work. It is generally accepted that the stearic acid photocatalytic decomposition reaction pathway has no major intermediates, therefore it can be easily monitored through IR-observable species (SA disappearance or CO_2 generation). A 0.1 M stearic acid solution in acetone was used for the test. The same sample size of the thin films, 1.5 cm $\times$ 2.5 cm, were spin-coated with 0.5 mL of stearic acid using an Osilla spin coater at 1000 rpm speed for 30 s. After spin coating the samples were kept in the dark for 1 h to ensure that the acetone had evaporated from the surfaces. Each sample was tested under both UV and visible light irradiation. The light sources used for irradiation of these samples were identical to the light sources used for the methylene blue decomposition tests.

CHAPTER IV

RESULTS AND DISCUSSIONS

4.1 Nitrogen-Silicon-codoped titanium dioxide

In this part, the nitrogen and silicon codoped on titanium dioxide powder were synthesized by two different methods, solvothermal and sol-gel. The effect of nitrogen addition by using nitrogen-containing gas at post-annealing process was the main purpose of the study. The physiochemical properties were measured by XRD, UV–vis, ESR, TEM, EDX, XPS. Moreover, a photocatalytic activity test was performed in the liquid phase photodecolourisation of methylene blue.

An overview of doping conditions for the undoped and nitrogen-silicon-codoped titanium dioxide powder are summarized in **Table 4.1**. The crystalline structure of commercial titanium dioxide P25, titanium dioxide and nitrogen-silicon-codoped titanium dioxide prepared by the solvothermal and sol-gel methods, which were annealed at different atmospheres, are given in **Figure 4.1**. All titanium dioxide synthesized samples exhibited primarily an anatase phase crystalline structure corresponding to JCPDF No. 21-1272 which appeared 2θ about 25°(major), 37°, 48°, 55°, 56°, 62°, 71°, and 75°. Moreover, a small peak of 2θ ca. 28°(major), 36°, 42°, and 57° were observed in P25 and titanium dioxide which was synthesized via the sol-gel process, indicating the rutile phase structure formation which referring to JCPDF No. 34-0180. As a result, a small shift of the XRD peaks to higher angles was only observed from nitrogen-annealed titanium dioxide. It is implied that the nitrogen atoms probably substituted into titanium dioxide crystalline leading to the distortion of TiO_6 octahedron. This result rather agreed in the EDX result (see in **Table 4.2**). Addition of a small amount of silicon did not affect the shift of 2θ in XRD pattern, but the EDX analysis indicated the element of Si atom in titanium dioxide. It can be indicated that this materials are more-likely to be a composite of titanium dioxide and silica, rather than silicon atoms distributed in titanium dioxide backbone. As a result, the partial

monolayer of silica may be coated on titanium dioxide surface, inhibiting the crystal growth since the restrict ion migration in the limited spacing [185, 186].

Table 4.1 *Summary of the doping conditions of the titanium dioxide powder*

Catalyst	Preparation method	Annealing atmosphere	Si
TiO_2_SVT_O	Solvothermal	Oxygen	-
TiO_2_SVT_A	Solvothermal	Air	-
TiO_2_SVT_N	Solvothermal	Nitrogen	-
1%Si/TiO_2_SVT_O	Solvothermal	Oxygen	1%wt
1%Si/TiO_2_SVT_A	Solvothermal	Air	1%wt
1%Si/TiO_2_SVT_N	Solvothermal	Nitrogen	1%wt
TiO_2_SG_O	Sol-gel	Oxygen	-
TiO_2_SG_A	Sol-gel	Air	-
TiO_2_SG_N	Sol-gel	Nitrogen	-
1%Si/TiO_2_SG_O	Sol-gel	Oxygen	1%wt
1%Si/TiO_2_SG_A	Sol-gel	Air	1%wt
1%Si/TiO_2_SG_N	Sol-gel	Nitrogen	1%wt
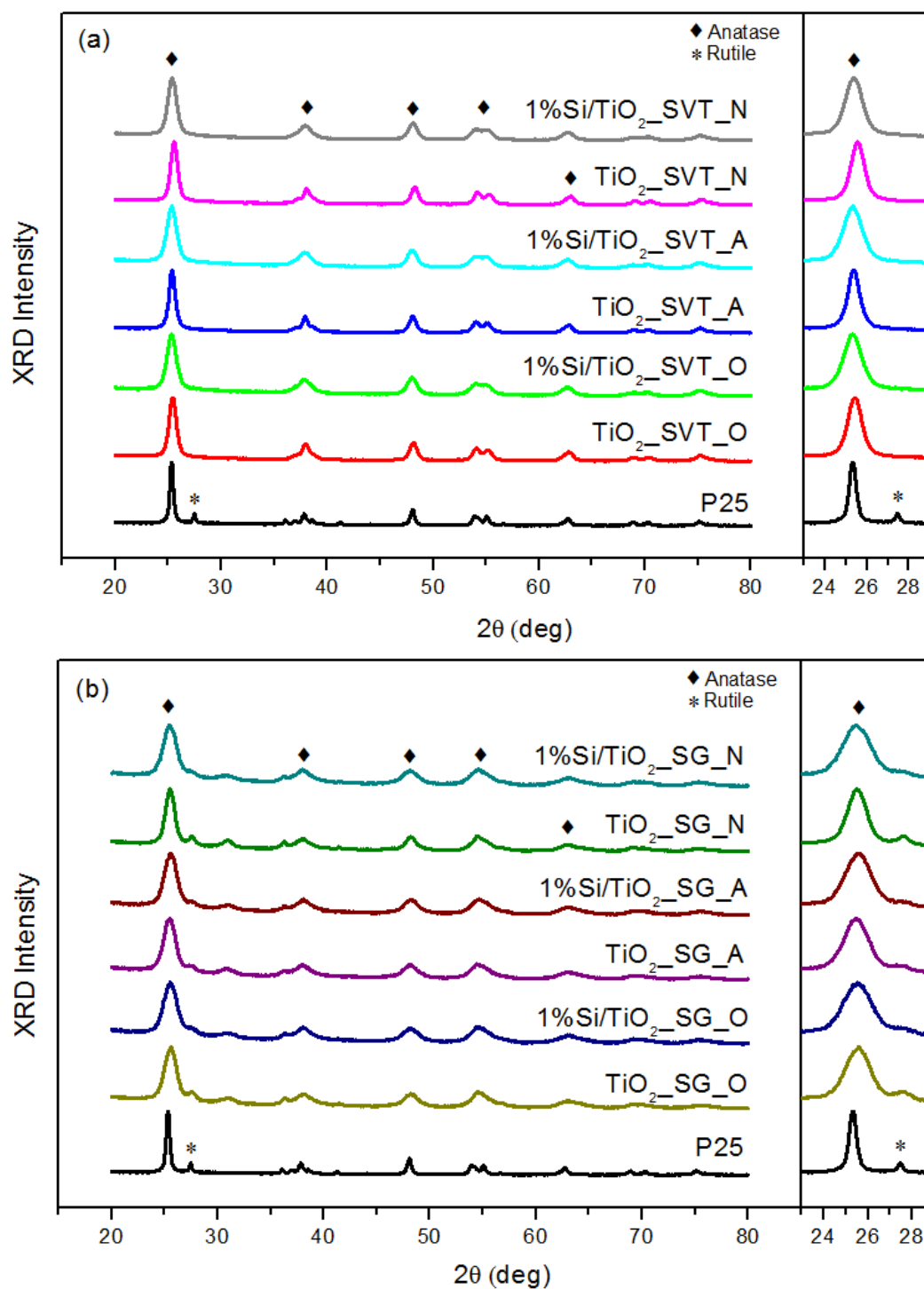
Figure 4.1 *XRD patterns of all powder samples which were prepared by (a) the solvothermal method and (b) the sol-gel method*

Table 4.2 EDX characterisation results

Catalyst	%Atomic composition				
	O	Ti	C	Si	N
P25	49.01	41.88	9.10	-	-
TiO_2_SVT_O	44.85	44.68	10.47	-	-
TiO_2_SVT_A	53.71	40.02	6.26	-	-
TiO_2_SVT_N	51.47	33.77	5.66	-	9.10
TiO_2_SG_O	54.92	39.32	5.76	-	-
TiO_2_SG_A	55.14	39.35	5.51	-	-
TiO_2_SG_N	41.27	47.12	4.86	-	6.75
1%Si/TiO_2_SVT_O	54.35	37.49	7.18	0.98	-
1%Si/TiO_2_SVT_A	56.02	36.06	6.70	1.22	-
1%Si/TiO_2_SVT_N	52.32	32.04	5.46	1.06	9.12
1%Si/TiO_2_SG_O	39.25	53.54	5.84	1.37	-
1%Si/TiO_2_SG_A	52.73	41.21	5.00	1.06	-
1%Si/TiO_2_SG_N	47.00	40.04	4.51	0.81	7.64

Table 4.3 summarize the crystallite size and phase contents of the all samples were calculated by their XRD patterns according to the methods of the Debye–Scherrer equation [187] and Spurr [188], respectively. The addition of small amounts of silicon resulted in a decrease of the crystallite size of the solvothermal and sol-gel derived titanium dioxide from 11 to 8 nm and 7 to 5 nm, respectively. Moreover, the partial monolayer of silicon also reduced the percentage of rutile content in sol-gel made catalysts that decreased from around 15% to 10%. The result is well confirmed that the addition of silica could effectively retard the growth of particles [186]. The silicon-titanium linkage had high thermal stability, which resulted in the suppression both of

the phase transformation from anatase to rutile and the growth of the titanium dioxide particles. On the other hand, the annealing gas did not alter the phase structure and the crystallite size of the samples.

Table 4.3 XRD characterization results

Catalyst	Anatase crystallite size (nm)	Phase Content (%)	
		Anatase	Rutile
P25	20.4	83.6	16.4
TiO_2_SVT_O	10.2	100.0	0
TiO_2_SVT_A	11.7	100.0	0
TiO_2_SVT_N	10.3	100.0	0
TiO_2_SG_O	6.7	85.8	14.2
TiO_2_SG_A	6.2	90.5	9.5
TiO_2_SG_N	8.1	86.3	13.7
1%Si/TiO_2_SVT_O	7.6	100.0	0
1%Si/TiO_2_SVT_A	7.6	100.0	0
1%Si/TiO_2_SVT_N	8.0	100.0	0
1%Si/TiO_2_SG_O	5.6	89.0	11.0
1%Si/TiO_2_SG_A	6.0	91.1	8.9
1%Si/TiO_2_SG_N	5.9	91.3	8.7

Figure 4.2 shows the TEM micrographs of all the titanium dioxide and nitrogen-silicon-codoped titanium dioxide catalysts prepared by the solvothermal and sol-gel methods. The catalyst particles were found to be spherical with an average size of around 5 to 15 nm. The particle sizes of titanium dioxide were gradually decreased due to the prevention of crystal growth by the silicon additives. These particle sizes, observed from TEM images, were consistent with the titanium dioxide crystallite size calculated from the XRD line broadening, indicating that the titanium dioxide obtained via both methods was single crystalline.
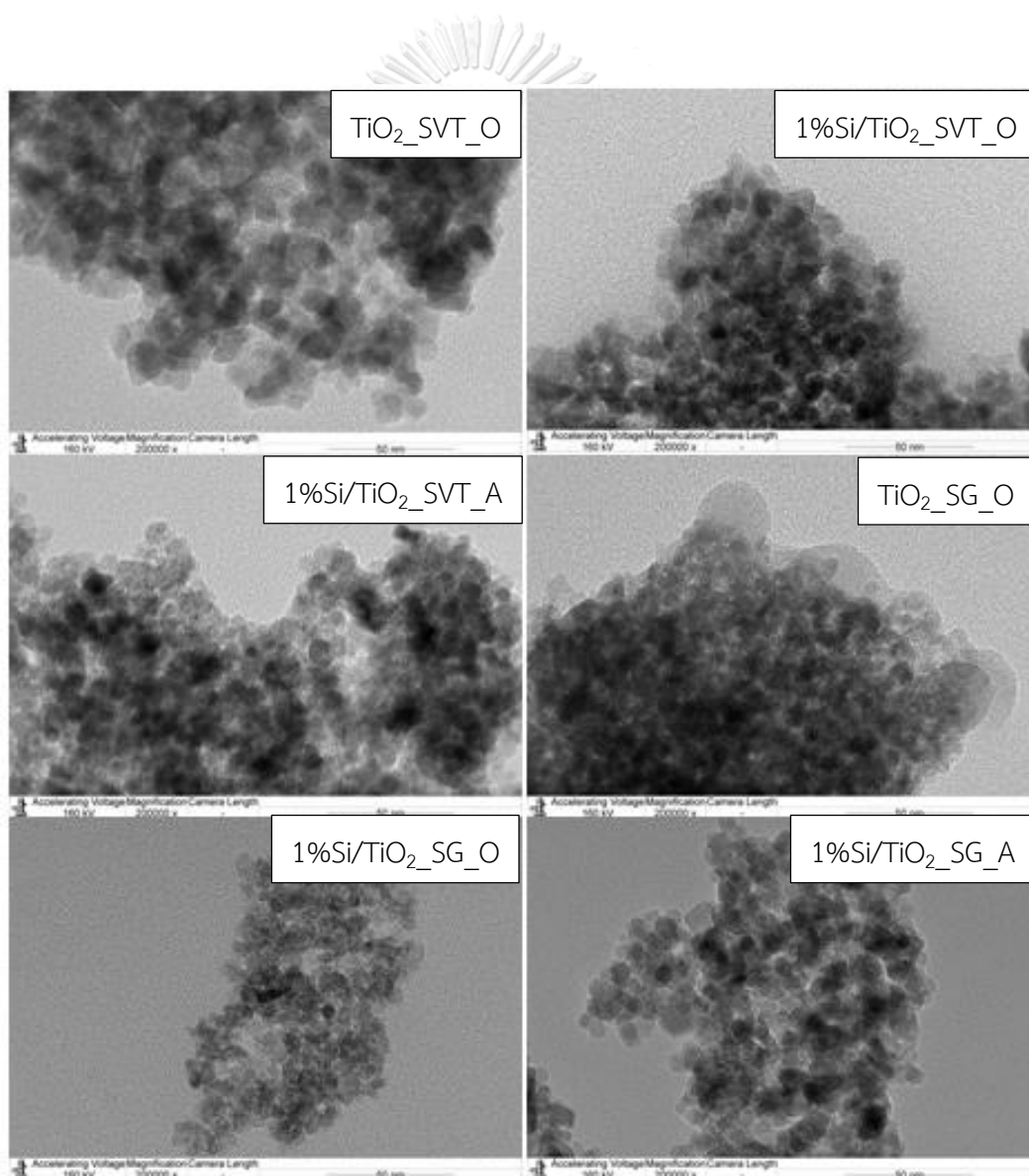
Figure 4.2 TEM micrographs of selected powder samples

The UV-Vis absorbance spectra of the commercial P25, titanium dioxide and nitrogen-silicon-codoped titanium dioxide prepared by using the solvothermal and sol-gel methods after annealing at various atmospheres are demonstrated in **Figure 4.3**. As a result in UV spectra, all titanium dioxide samples produced by the sol-gel and solvothermal methods exhibited absorption intensity lower than P25, but in visible spectra, these samples evidenced more intense absorption than P25. Especially, the annealing in nitrogen atmosphere showed higher absorption than ones. Moreover, the titanium dioxide continuously decreased the band edge absorption about 380 nm, thus resulting insignificant the band gap energy. A slightly red-shift appeared in the all titanium dioxide which annealed in nitrogen atmosphere. The larger red-shift can be attributed to the electron-hole pair transferring between the conduction band (CB) and/or the valance band (VB) of titanium dioxide photocatalyst.

XPS is a useful technique to determine the composition of the sample on its surface and electronic states. The elemental scans for Ti $2p$ of the all titanium dioxide and nitrogen-silicon-codoped titanium dioxide catalysts are illustrated in **Figure 4.4**. The peaks located at 457.5 and 463.2 eV assigned to Ti^{3+} $2p_{3/2}$ and Ti^{3+} $2p_{1/2}$, respectively, while the other peaks at 458.6 and 464.3 eV referred to Ti^{4+} $2p_{3/2}$ and Ti^{4+} $2p_{1/2}$, respectively (as depicted in **Figure 4.4**e and **Table 4.4**). In general the oxygen species can be investigated by XPS analysis. **Figure 4.4**f illustrates the deconvolution of O $1s$ of titanium dioxide photocatalyst. Three peaks in the XPS spectrum were observed around 530.3, 532.1, and 533.1 eV that related to the lattice oxygen, the chemisorption oxygen and the hydroxyl oxygen species [189], respectively. As a result, not only the different annealing atmospheres but also the partial monolayer of silicon coated on titanium dioxide affected the shifting of binding energy, thus partially reducing of Ti^{4+} to Ti^{3+}. The reduction of Ti^{4+} to Ti^{3+} of titanium dioxide leading to the formation of oxygen deficiencies. It should be noted that the existence of Ti^{3+} is essentially a defective state and acts as the electron-hole trapping to promote charge separation, and suppresses the recombination of electron–hole pairs, which promotes the photocatalytic activity. Moreover, these samples also exhibited the XPS shifting to the higher binding energy of O $1s$ (demonstrated in **Figure 4.4**b and d).
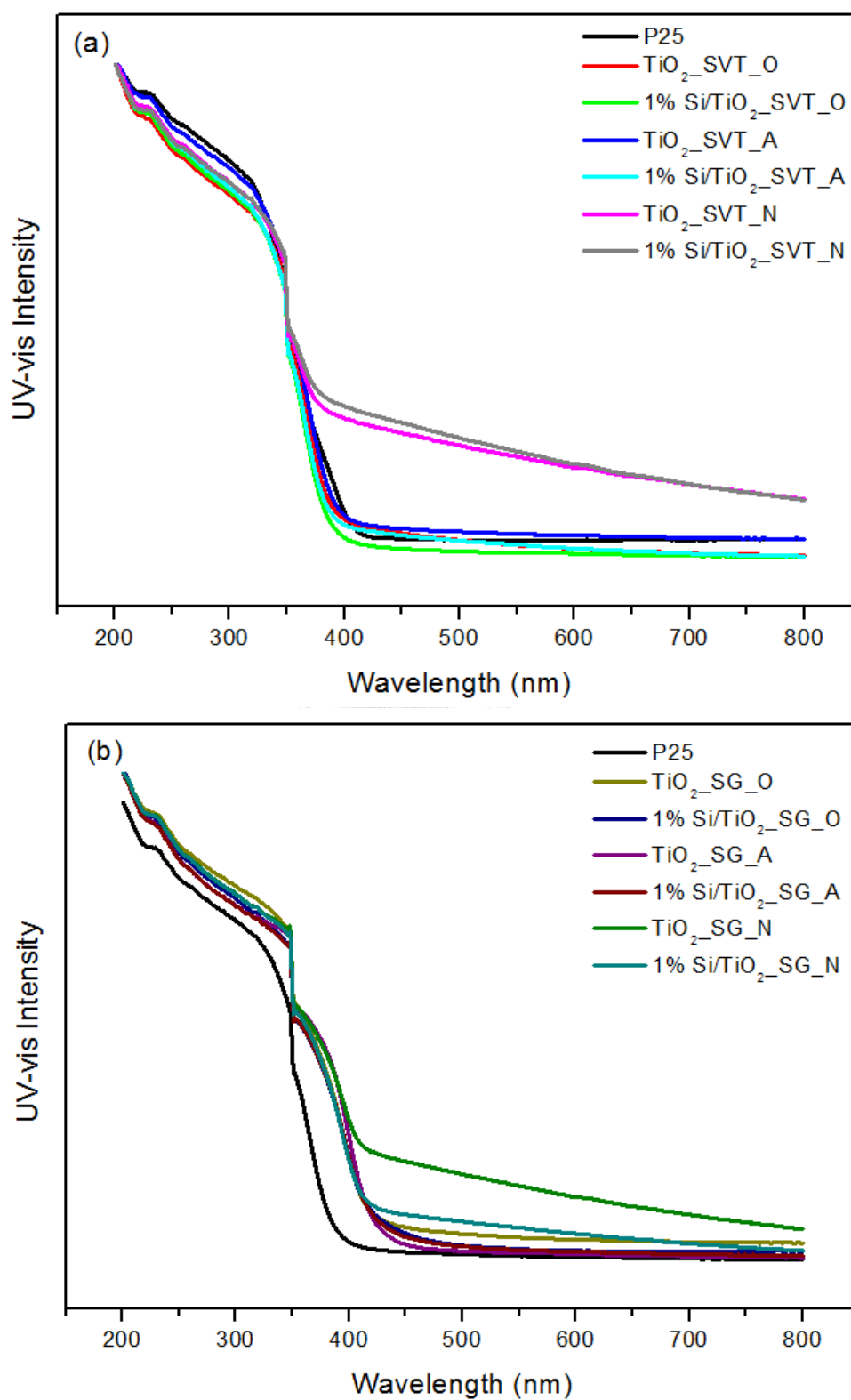
Figure 4.3 *UV–Vis absorbance spectra of all powder samples which were prepared by (a) the solvothermal method and (b) the sol-gel method*
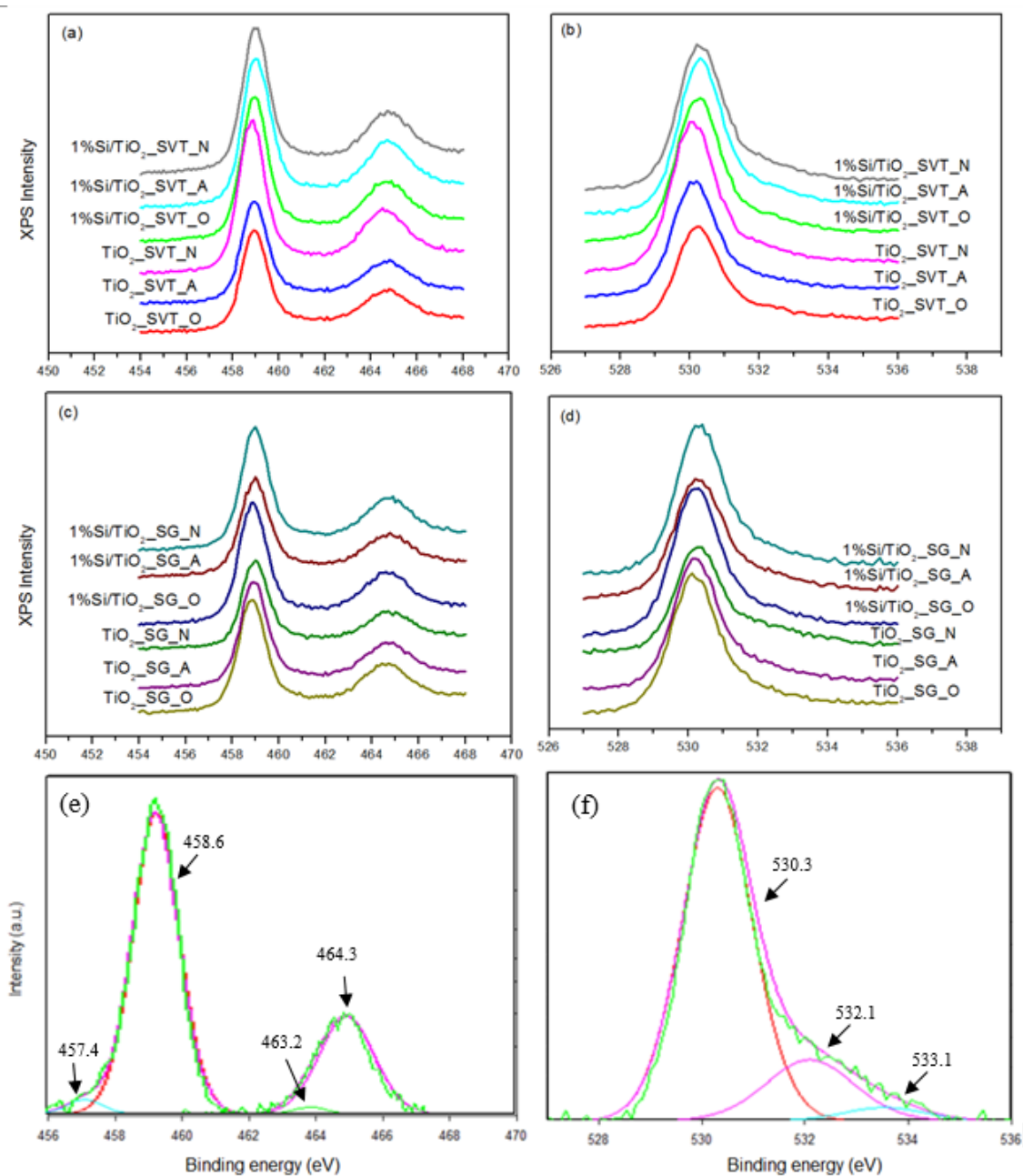
Figure 4.4 *XPS results of (a) Ti 2p (b) O 1s for solvothermal powder samples, (c) Ti 2p (d) O 1s for sol-gel powder samples, and (e) Ti 2p and (f) O 1s are the deconvolution*

Table 4.4 *XPS binding energies (eV) and FWHM of all powder samples*

Catalyst	XPS results (eV)			
	Ti *2p* peak		O *1s* peak	
	B.E. (eV)	FWHM	B.E. (eV)	FWHM
P25	-	-	-	-
TiO_2_SVT_O	458.9	1.4	530.2	1.4
TiO_2_SVT_A	458.8	1.2	530.2	1.5
TiO_2_SVT_N	458.6	1.3	530.0	1.5
TiO_2_SG_O	458.8	1.4	530.1	1.6
TiO_2_SG_A	458.9	1.4	530.2	1.6
TiO_2_SG_N	458.6	1.3	530.4	1.6
1%Si/TiO_2_SVT_O	459.0	1.3	530.3	1.5
1%Si/TiO_2_SVT_A	458.4	1.4	529.7	1.5
1%Si/TiO_2_SVT_N	458.9	1.3	530.2	1.6
1%Si/TiO_2_SG_O	458.9	1.4	530.3	1.6
1%Si/TiO_2_SG_A	459.0	1.4	530.2	1.7
1%Si/TiO_2_SG_N	459.0	1.3	530.4	1.6

The ESR spectra of the P25, titanium dioxide and nitrogen-silicon-codoped titanium dioxide catalysts, prepared by using the solvothermal and sol-gel methods after annealing at various atmospheres detected at room temperature, are shown in **Figure 4.5**. The ESR spectrum exhibited a sharp signal at g = 1.989 and a broadening signal at about g = 2.001. These signals correspond to the Ti^{3+} cations formed on the titanium dioxide surface [190, 191], and the resonance of oxygen centred surface hole trapping sites (O^{2-} species) [192], respectively. As the result, the sharp signal at g around 1.989 became stronger as the result of the lower oxygen concentration. In contrast,

the intensity of a big broad signal at g = 2.001 became lower and disappeared on the sample annealed with the nitrogen flow. The more intense sharp signal indicates that the amounts of Ti^{3+} on the surface of titanium dioxide increased after annealing with the nitrogen flow. This result was in good agreement with the XPS spectra.
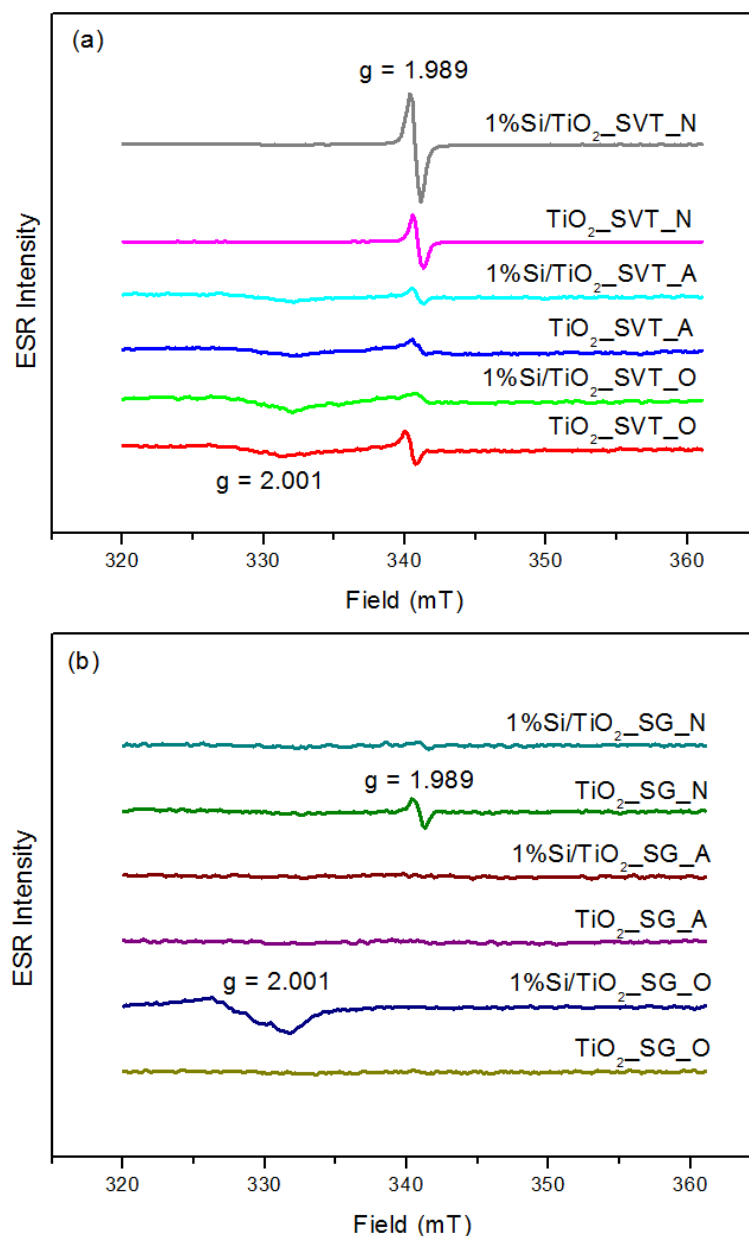
Figure 4.5 *ESR spectra results of all powder samples which were prepared by (a) the solvothermal method and (b) the sol-gel method*

The catalytic performances in liquid phase were investigated using the photodecolourisation of methylene blue under UV and visible light irradiation as illustrated in **Figure 4.6**. **Figure 4.6** demonstrates the catalytic activity of titanium dioxide and the partial monolayer of silicon on titanium dioxide photocatalyst that produced by solvothermal and sol-gel methods, respectively, under UV-light irradiation. The photodecolourisation rate of methylene blue improved in the following order nitrogen > air > oxygen. This could be attributed to the increase of Ti^{3+} after annealing under depletion of oxygen flows as reported in the ESR spectra and XPS results. Moreover, the partial monolayer of silicon can improve the anatase phase stability. Since, the photocatalytic activity of the anatase phase was higher than the rutile form due to the higher adsorption affinity of the organic dye molecules and lower rates of electron-hole recombination [78, 193, 194].

The photocatalytic performances of all photocatalysts under visible light irradiation are shown **Figure 4.7**. The photocatalytic activity of P25 and all pure titanium dioxide annealed by air and oxygen decreased as the changing of the light source but the sol-gel catalyst still maintained high photocatalytic activity due to the red shift of the band-gap energy, as seen in the UV-Vis result. In the case of the solvothermal catalyst, a similar trend is obtained when this is compared to the reaction under UV irradiation. The nitrogen-silicon-codoped titanium dioxide prepared by solvothermal still exhibited the highest activity. As a result, the higher anatase stability, increasing of the Ti^{3+} surface sites and the red shift of the band-gap energy to visible regions promotes the photocatalytic activity.
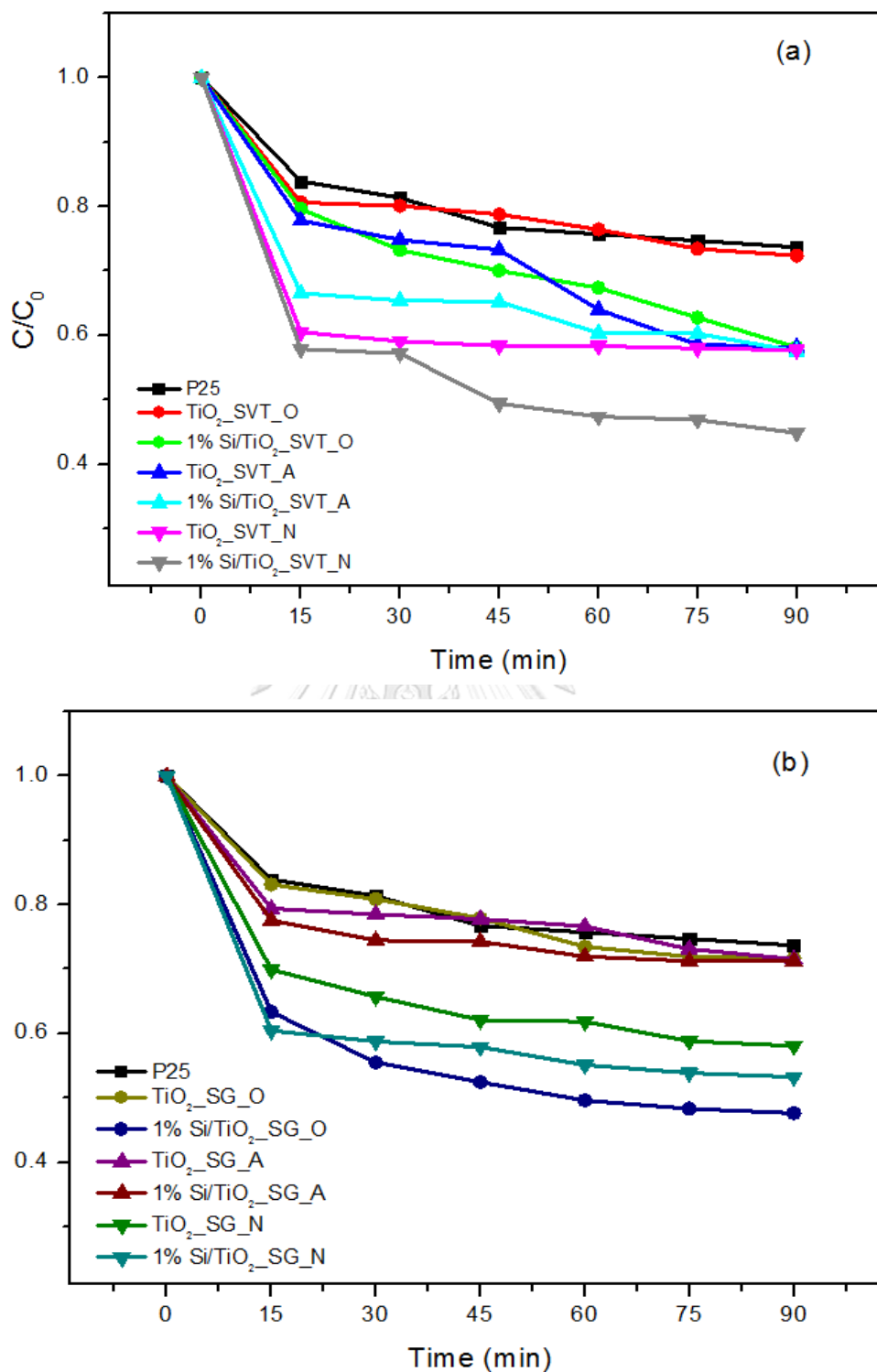
Figure 4.6 *Catalytic performances for methylene blue photodecolourisation under UV light irradiation of all samples powder which were prepared by (a) solvothermal (b) sol-gel method*
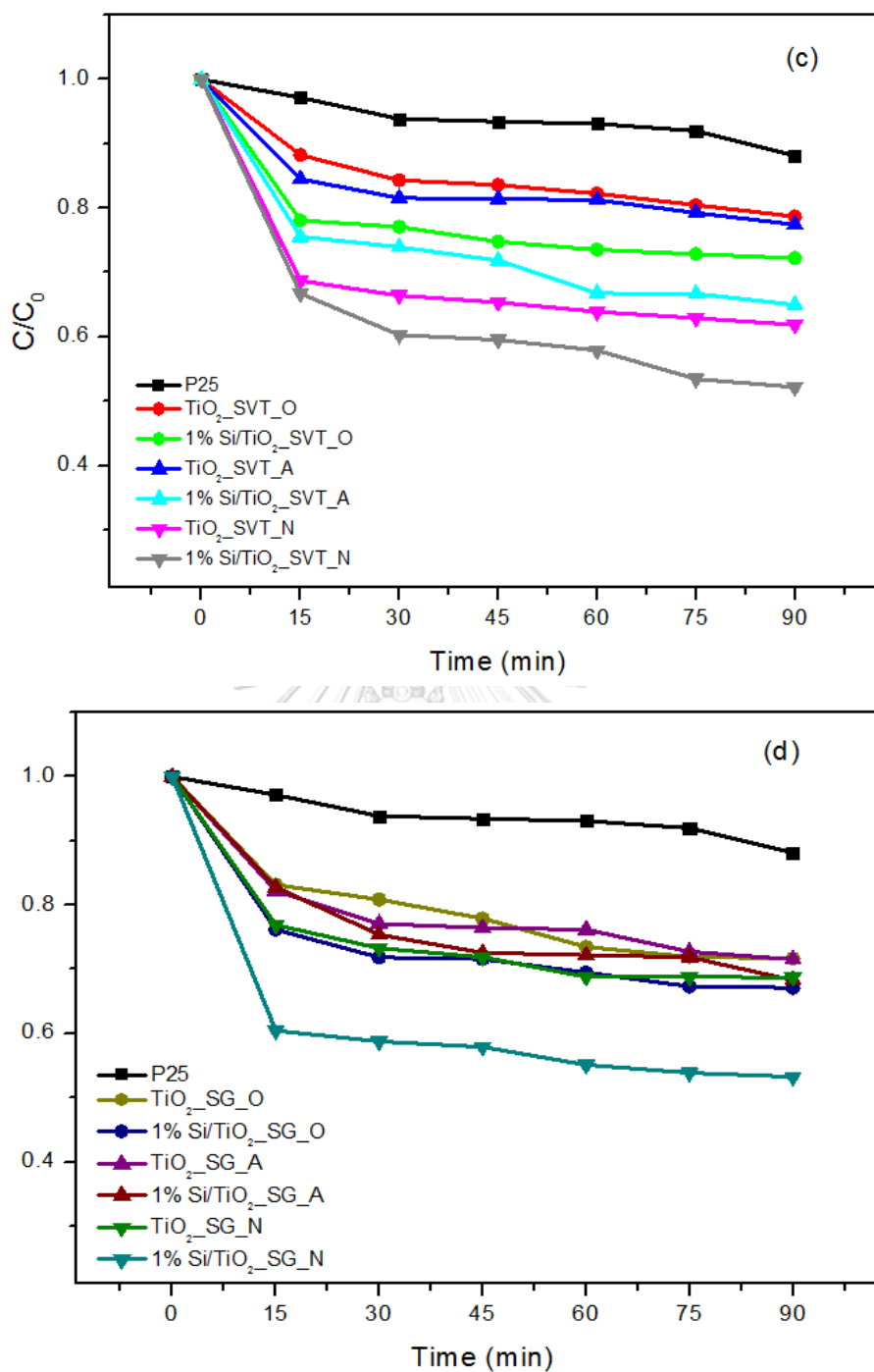
Figure 4.7 Catalytic performances for methylene blue photodecolourisation under visible light irradiation of all prepared powder samples prepared by (c) solvothermal (d) sol-gel method

However, a different trend was found after tests using visible light irradiation. The catalytic activity of undoped titanium dioxide increased in the order of solvothermal > sol-gel methods. This result was probably due to the higher red shift of the solvothermal-catalyst when compared with the P25 and sol-gel-catalyst. After the addition of silicon, the catalytic performance of the catalysts was improved but the changing of the calcination environment did not improve the photocatalytic activity of the sol-gel-catalyst, except for $1\%Si/TiO_2\_SG\_N$. This result could be due to the small change in band gap energy after treatment with different gases, as can be seen in UV-Vis result.

4.2 Modification of titanium dioxide by aminopropyltriethoxysilane (APTES)

This part aims to investigate the effect of APTES concentration on the commercial titanium dioxide P25 catalysts modified by hydrothermal method. The characteristics and catalytic properties of photocatalysts were investigated by various techniques such as XRD, N_2 physisorption, UV-vis, XPS, TGA, PL, and SEM-EDX. Moreover, the catalytic performance of catalysts was evaluated in liquid-phase photodecolourisation of methylene blue and TOC.

The specific surface area was calculated by employing the Brunauer–Emmett–Teller (BET) adsorption model. Adsorption isotherms of pristine titanium dioxide and APTES-modified titanium dioxide are presented in **Figure 4.8**. All samples exhibited typical *Type IV* adsorption behaviour and *Type H1* hysteresis loop in accordance with the IUPAC classification. The pore volume and pore diameter, calculated by the BJH method, are summarized in **Table 4.5**. All APTES- modified titanium dioxide were an insignificant changes in BET surface area compared to pristine titanium dioxide. However, APTES-modified titanium dioxide were noteworthy in both pore volume and pore diameter. It is implied that rate of photocatalytic reaction can be increased due to the enhancing adsorption of reaction and rapid diffusion of products [195]. Typically, a high *c*-value indicated a strong interaction of the nitrogen molecules on the titanium dioxide surface due to the presence of hydrophilic molecules on the titanium dioxide surface. In another word, a low *c*-value represented the hydrophobic surface [196-199]. As a result, it can be demonstrated that the APTES-modified titanium dioxide surfaces are performing an essential role in surface properties such as changing from hydrophilic to hydrophobic. It can be observed that the hydrophobic surface increased with increasing the APTES concentrations.
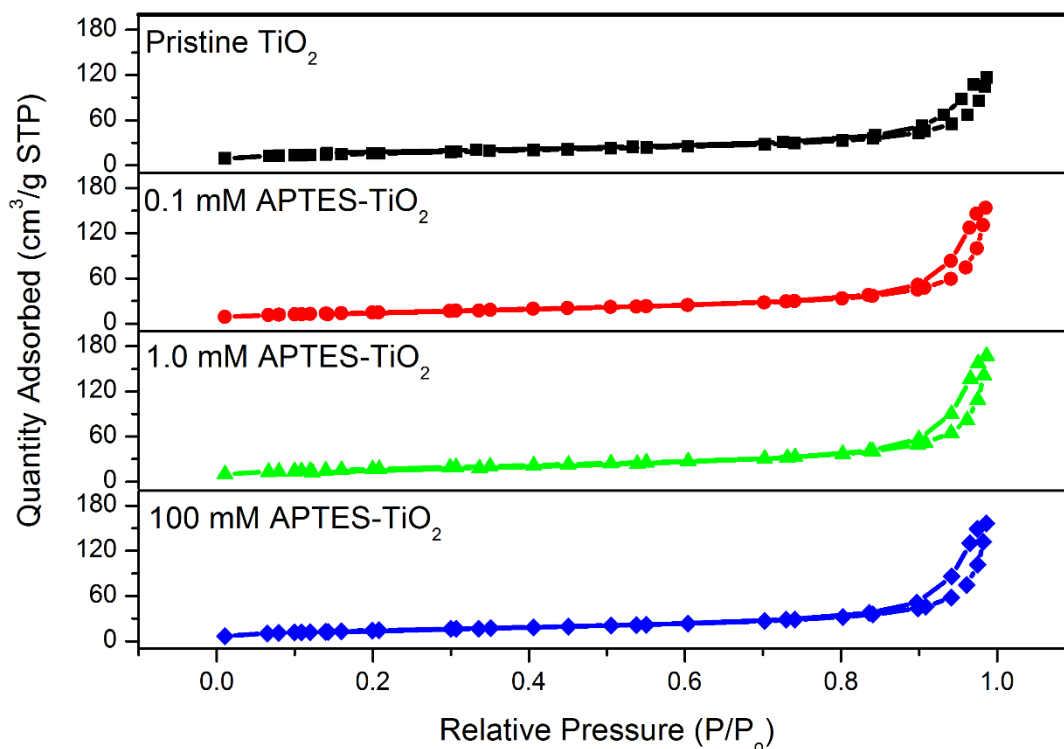
Figure 4.8 *N$_2$ adsorption-desorption isotherms of pristine titanium dioxide and APTES-modified titanium dioxide*

Table 4.5 *Summarisation of the properties of pristine titanium dioxide and modified titanium dioxide*

Sample	Surface area (m²/g)	Pore volume[b] (cm²/g)	Pore size[b] (nm)	c-value[b]
Pristine TiO$_2$	57	0.17	11.6	97
0.1 mM APTES-TiO$_2$	53	0.23	17.1	94
1.0 mM APTES-TiO$_2$	60	0.24	16.2	93
100 mM APTES-TiO$_2$	54	0.23	17.2	51

[a]Calculation based on Bragg's law using XRD peaks

[b]Calculation based on N$_2$ physisorption isotherm

Moreover, the hydrophobic property of titanium dioxide surfaces may be evaluated by the thermal gravimetric analysis (TGA). **Figure 4.9** reveals the weight loss of pristine titanium dioxide and APTES-modified titanium dioxide. There are three stages of weight loss, the first stage weight loss below at 393 K that attributed to the physical adsorption of hydroxyl groups. The second stage weight loss around 393 K to 573 K assigned to the weak chemisorbed of hydroxyl group [200]. The last one, weight loss in range of 573 K to 873 K indicated to the strong chemisorption of hydroxyl group [201, 202]. The APTES modification on titanium dioxide surface can reduce weight loss as an effect of hydrophobic surface property [203, 204].
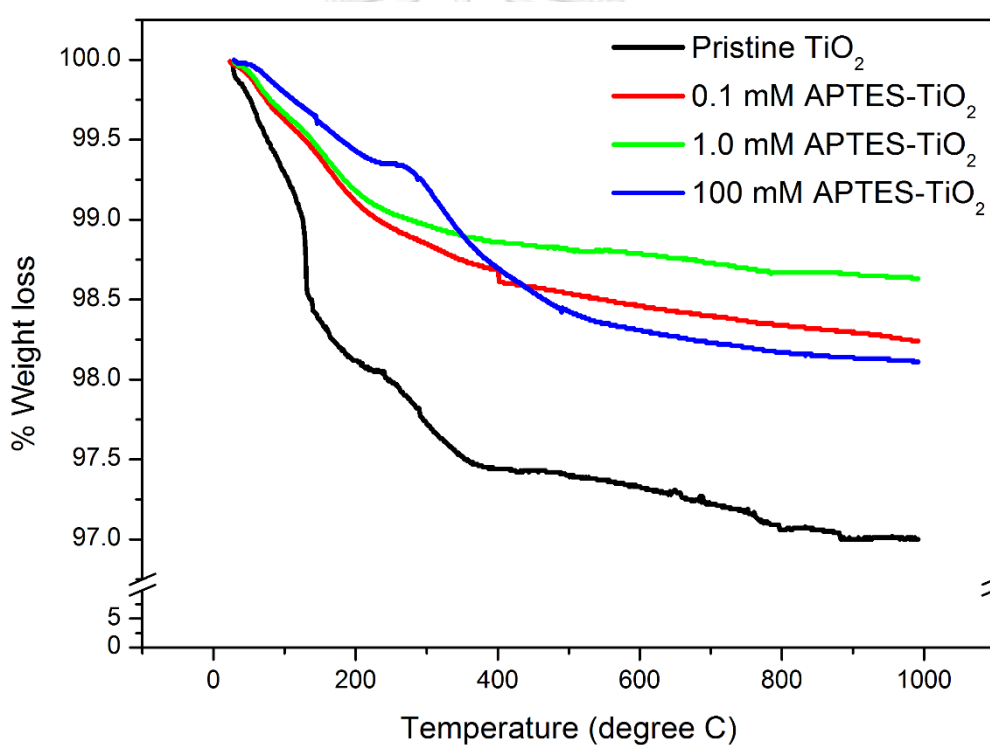
Figure 4.9 TGA of pristine titanium dioxide and APTES-modified titanium dioxide

In order to corroborate that the modification of titanium dioxide with APTES can improve hydrophobic properties, the surface analysis needs to be investigated by X-ray photoelectron (XPS) analysis. Three species of oxygen disclosed in titanium dioxide surface, for instance, the lattice oxygen (O_L), the oxygen chemisorption (O_C), and the oxygen physisorption in hydroxyl groups (O_H), which are located around 529.6, 531.8 and 533.4 eV, respectively [205-207] (as displayed in **Figure 4.10**). As a result in **Table 4.6**, the lattice oxygen of pristine titanium dioxide showed higher than APTES-modified titanium dioxide. Moreover, the oxygen chemisorption and the oxygen physisorption of APTES-modified titanium dioxide decreased with increasing the APTES contents.
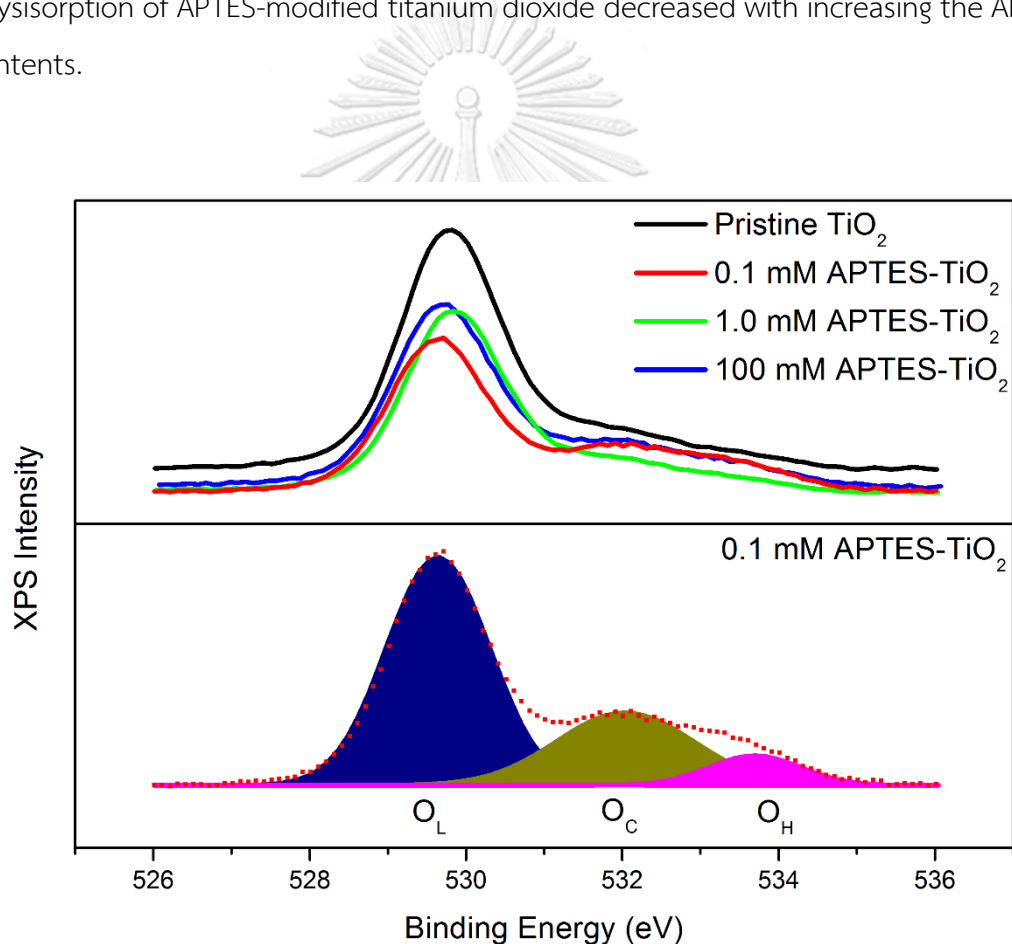
Figure 4.10 *O 1s XPS spectra of pristine titanium dioxide and APTES-modified titanium dioxide*

Table 4.6 *The percentage of oxygen and nitrogen atomic species on titanium dioxide surface from XPS analysis*

Sample	O $1s$			N $1s$	
	O_L	O_C	O_H	NH_2	NH_3^+
Pristine TiO$_2$	79	17	4	-	-
0.1 mM APTES-TiO$_2$	65	27	8	62	38
1.0 mM APTES-TiO$_2$	71	22	7	66	34
100 mM APTES-TiO$_2$	69	24	7	69	31

Furthermore, the amine functional groups are projecting away from the oxide surface can describe the hydrophobic property. **Figure 4.11** illustrates the deconvolution of N $1s$. The amine group of APTES-modified titanium dioxide exhibited two functional species, i.e. free terminal amine (NH_2) and protonated amine (NH_3^+) that is observed at about 399.9 and 401.8 eV [208-210], respectively. This result is rather evidenced that the free terminal amine (NH_2) acting as a hydrophobic property increased with increasing the concentration of APTES [89, 211-214]. There is somewhat agreed that APTES-modified titanium dioxide surface can improve hydrophobic property of the oxide surface. The existence of hydrogen bonding between amine groups and residual silanols can form the protonated amine (NH_3^+) tails, thus promoting proton transfer on the titanium dioxide surface [215].
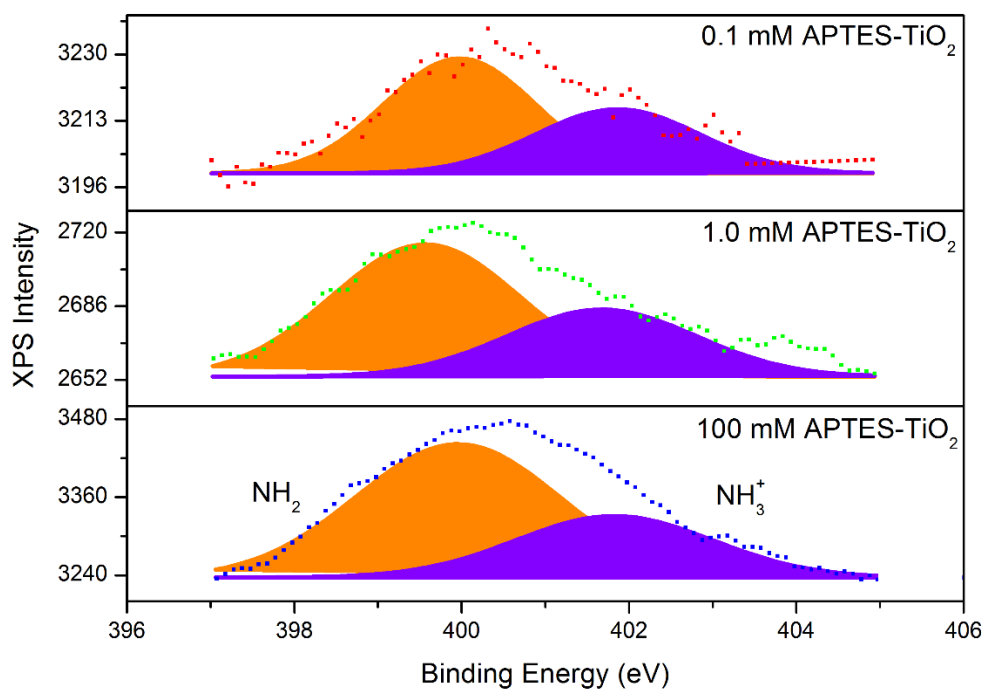
Figure 4.11 N 1s XPS spectra of pristine titanium dioxide and APTES-modified titanium dioxide

In addition, the linkage of Ti-O-Si can demonstrate the amount of APTES contents coverage on the titanium dioxide surface. The result given in **Figure 4.12**, the presence of Ti-O-Si linkage appeared about 101.1 eV [216], while the $Si-O_{(4-\delta)}$ ($1 \leq \delta \leq 3$) located around 102.5 eV [217]. Amount of Ti-O-Si linkages increased corresponding to the higher APTES concentrations, as reported in **Table 4.7.** However, APTES-modified titanium dioxide surface insignificantly affected titanium species. The Ti^{4+} appeared at 458.4 and 464.2 eV, while Ti^{3+} evidenced about 457.2 and 462.9 eV [218, 219] (as depicted in **Figure 4.13**).
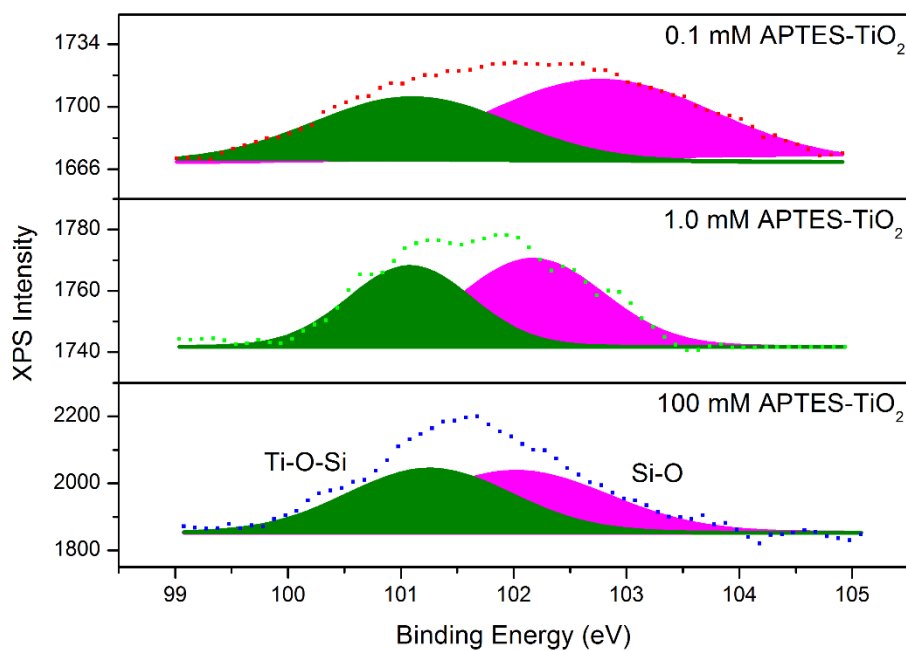
Figure 4.12 Si 2p XPS spectra of pristine titanium dioxide and APTES-modified titanium dioxide

Table 4.7 The percentage of silicon and titanium atomic species on titanium dioxide surface from XPS analysis

Sample	Si 2p		Ti 2p	
	Ti-O-Si	Si-O$_{(4-\delta)}$	Ti^{3+}	Ti^{4+}
Pristine TiO$_2$	-	-	11	89
0.1 mM APTES-TiO$_2$	41	59	12	88
1.0 mM APTES-TiO$_2$	44	56	10	90
100 mM APTES-TiO$_2$	48	52	12	88
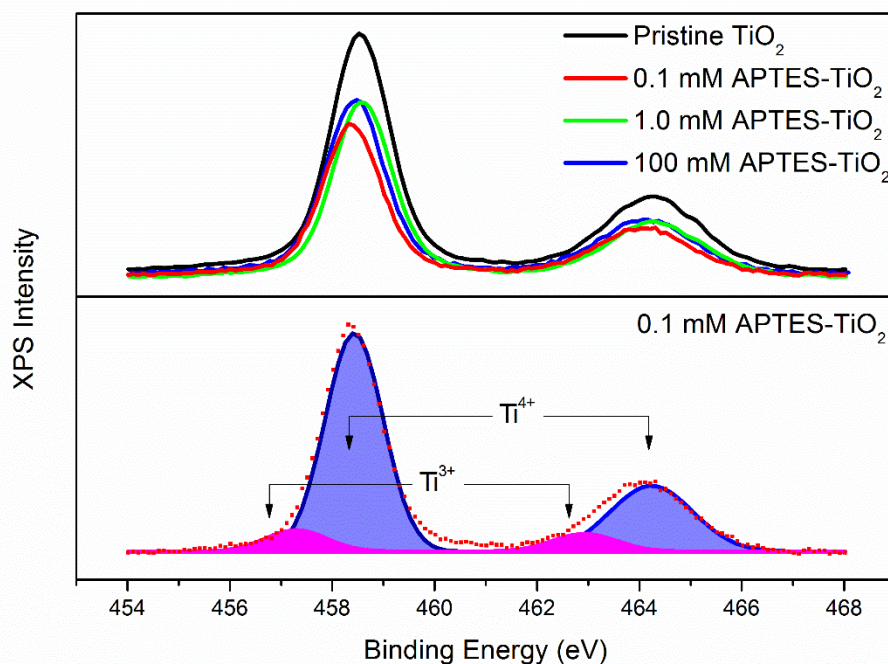
Figure 4.13 *Ti 2p XPS spectra of pristine titanium dioxide and APTES-modified titanium dioxide*

The coverage of Si-O covalent bonding on titanium dioxide surface can be confirmed by X-ray diffraction (XRD). The normalized X-ray diffraction patterns of pristine titanium dioxide and APTES-modified titanium dioxide are shown in **Figure 4.14**. All samples were obtained primarily in the anatase phase, which referred to Joint Committee on Powder Diffraction Standard (JCPDS) card No. 21-1272. Moreover, a small peak of 2θ at 27° (major), 36°, 41°, and 57° were associated with the rutile phase, according to JCPDS card No. 21-1276. As a result, the XRD patterns of all APTES-modified titanium dioxide appeared a slightly shifted to lower 2θ angles, thus slightly changing the lattice parameter. However, the lattice parameter and the c/a ratio are insignificant differences in APTES modification (see in **Table 4.8**). The slight change of lattice parameter confirms the functionalization of the APTES covalently attached on Ti-O surface formed part of monolayer and/or multilayer coverage on metal oxide surface [220], leading to the slight distortion of TiO_6 octahedral [221]. On the other hand, the surface modification by APTES did not alter the phase structure and the crystallite size of the titanium dioxide which were around 17-19 nm.
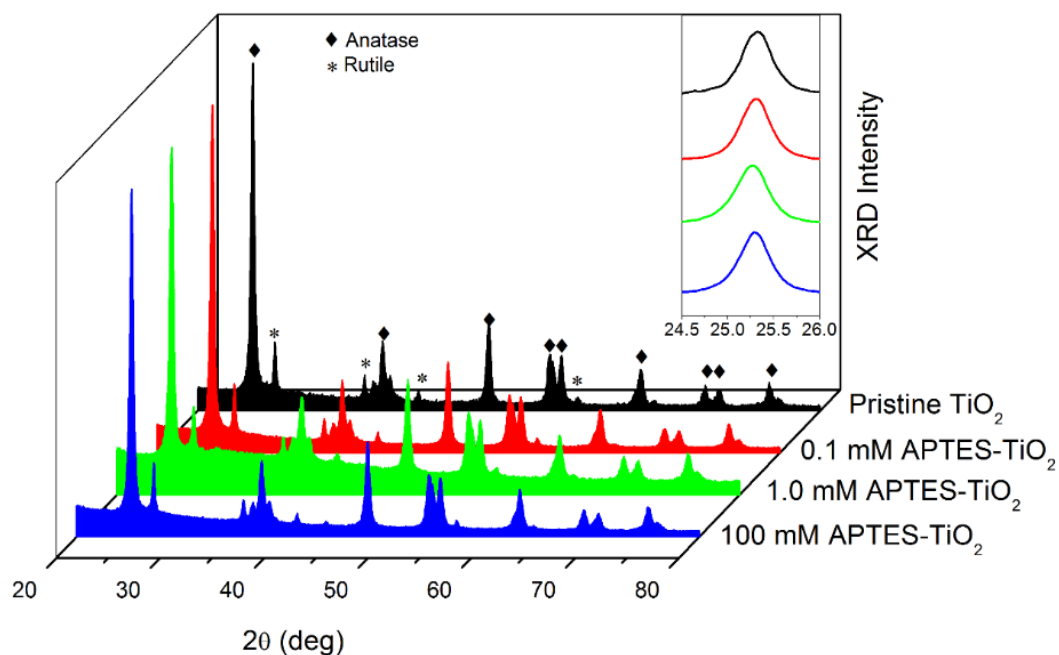
Figure 4.14 XRD patterns of pristine titanium dioxide and APTES-modified titanium dioxide

Table 4.8 Summarization the crystal properties of pristine titanium dioxide and modified titanium dioxide

Sample	Crystallite size (nm)	Lattice Parameter		
		a (nm)	c (nm)	c/a
Pristine TiO$_2$	19	0.3786	0.9507	2.511
0.1 mM APTES-TiO$_2$	18	0.3788	0.8525	2.515
1.0 mM APTES-TiO$_2$	17	0.3790	0.9539	2.517
100 mM APTES-TiO$_2$	18	0.3788	0.9550	2.521

[*]Calculation based on Bragg's law using XRD peaks

The indirect band gap is demonstrated in **Figure 4.15** and **Table 4.8**. It can be seen that APTES-modified titanium dioxide exhibited significantly lower indirect band gap energy than pristine titanium dioxide. Therefore Si-N can be raised to intermediate states within the band gap, thus decreasing band gap energy [222]. Moreover, this result corresponded to the red-shift of titanium dioxide surface modification with APTES in UV-vis absorption spectra. It implies that the nearer indirect band gap can simplify excitation of an electron from the maximum valence band up to the minimum conduction band under visible light irradiation, resulting in increasing the photocatalytic activity [223, 224]. Moreover, the optical absorptions can directly determine the electronic structure of material. The coordinated vibration of atoms in TiO_6 octahedral due to the distortion of the crystalline structure can generate the phonon emission and rapidly decay by thermalisation (as seen in **Table 4.9**). The increasing of phonon energy of APTES-modified titanium dioxide can introduce the localized state in titanium dioxide.
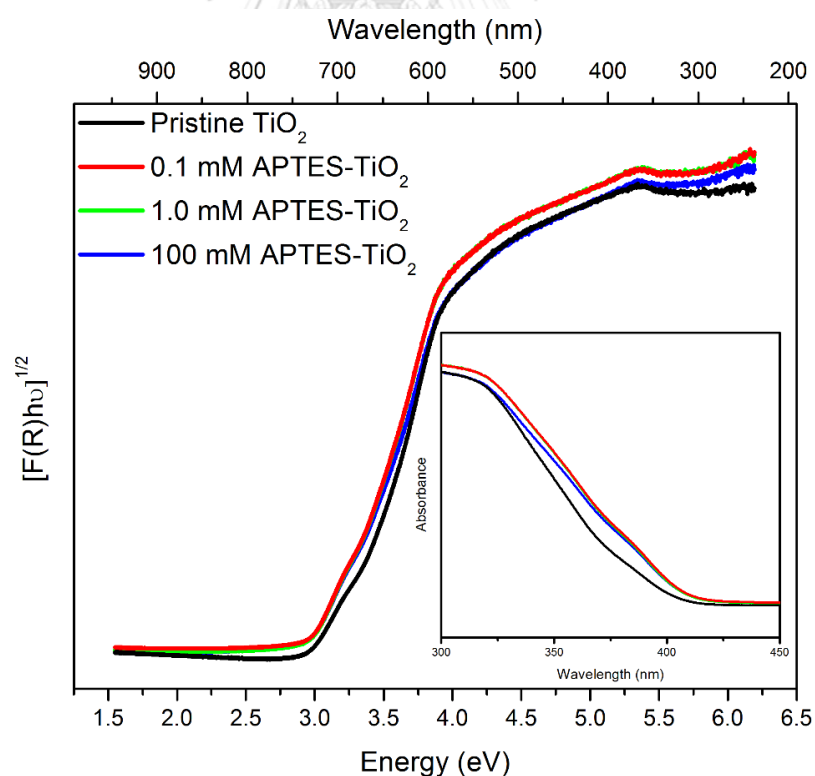
Figure 4.15 *Indirect band gap and UV-vis absorption spectra of pristine titanium dioxide and APTES-modified titanium dioxide*

Table 4.9 *Summarization the properties values of pristine titanium dioxide and modified titanium dioxide*

Sample	Band gap[a] (eV)	Phonon energy[b] (eV)
Pristine TiO$_2$	3.22	0.66
0.1 mM APTES-TiO$_2$	3.10	0.78
1.0 mM APTES-TiO$_2$	3.10	0.78
100 mM APTES-TiO$_2$	3.14	0.74

[a]Calculation based on UV-vis spectrum

[b]Calculation based on the different binding energy of UV-vis highest peak and PL spectra
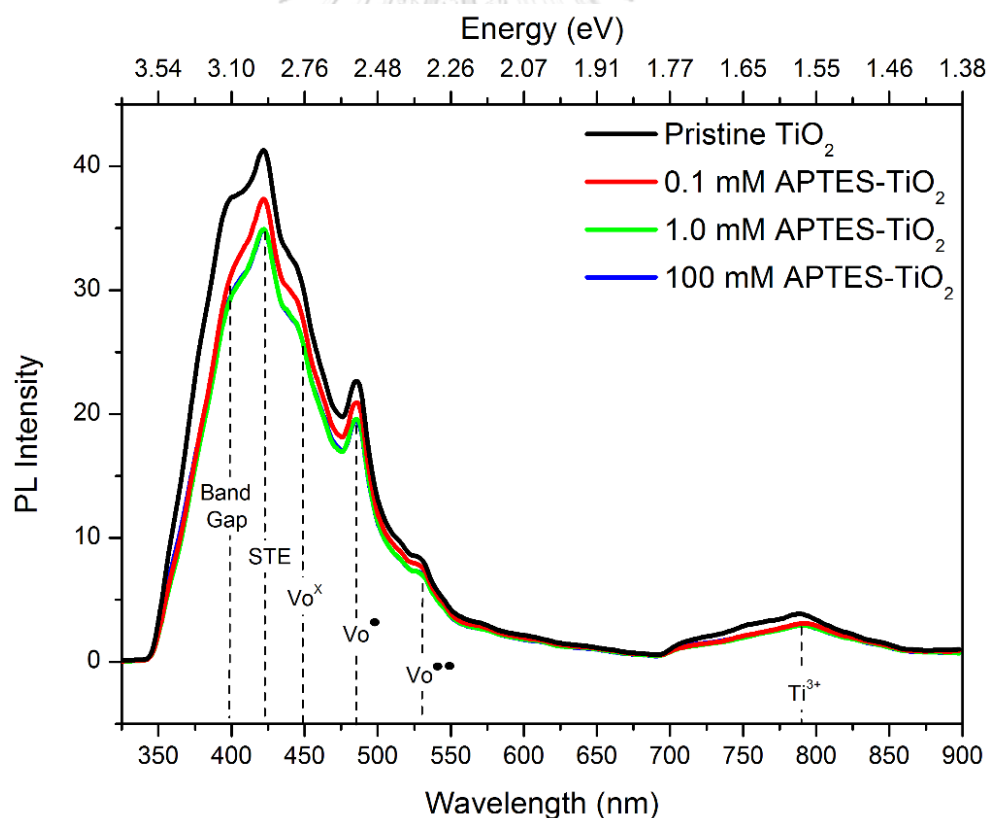
Figure 4.16 *PL spectra of pristine titanium dioxide and APTES-modified titanium dioxide*

Figure 4.16 demonstrates the photoluminescence (PL) spectra. As a result, the APTES modified-titanium dioxide revealed lower intensity of PL spectra than pristine titanium dioxide. It indicated that the monolayer and/or multilayer of Si-O on surface of titanium dioxide can reduce the recombination process [225]. Moreover, six peaks appeared in PL spectra at about 3.10, 2.92, 2.76, 2.55, 2.34, and 1.57 eV that described to the optical band gap due to the light-induced relaxation of hydrophilic particles [226, 227], the self-trapped excitons (STE) of TiO_6 octahedral [228], the neutral oxygen vacancies (V_O^x) [229], the singly ionized oxygen vacancies ($V_O^{\bullet}$) [229], the doubly ionized oxygen vacancies ($V_O^{\bullet\bullet}$) [229], and the interstitial of Ti^{3+}, respectively.

Both lighting and catalyst are especially for photoreactions. The electron-hole pairs are generated by light from catalytically active species. The partial electrons-holes can be recombined, causing defect chemistry in structure i.e. $[V_O^Z]$ and $[V_{Ti}^X]$. After theirs creation these electrons-holes can transfer charge carriers to reach the surface. The electron can be absorbed and react with oxygen molecules by the reduction process in conduction band, while the hole can be oxidized with water and other products via the oxidation process in the valence band. The bulk composition and morphology on APTES-modified titanium dioxide and pristine titanium dioxide was also characterized by SEM-EDX, shown in **Figure 4.17** and **Table 4.10**. The SEM reveals the spherical of all APTES-modified titanium dioxide particles. The EDX result corresponds to the different concentration of APTES.
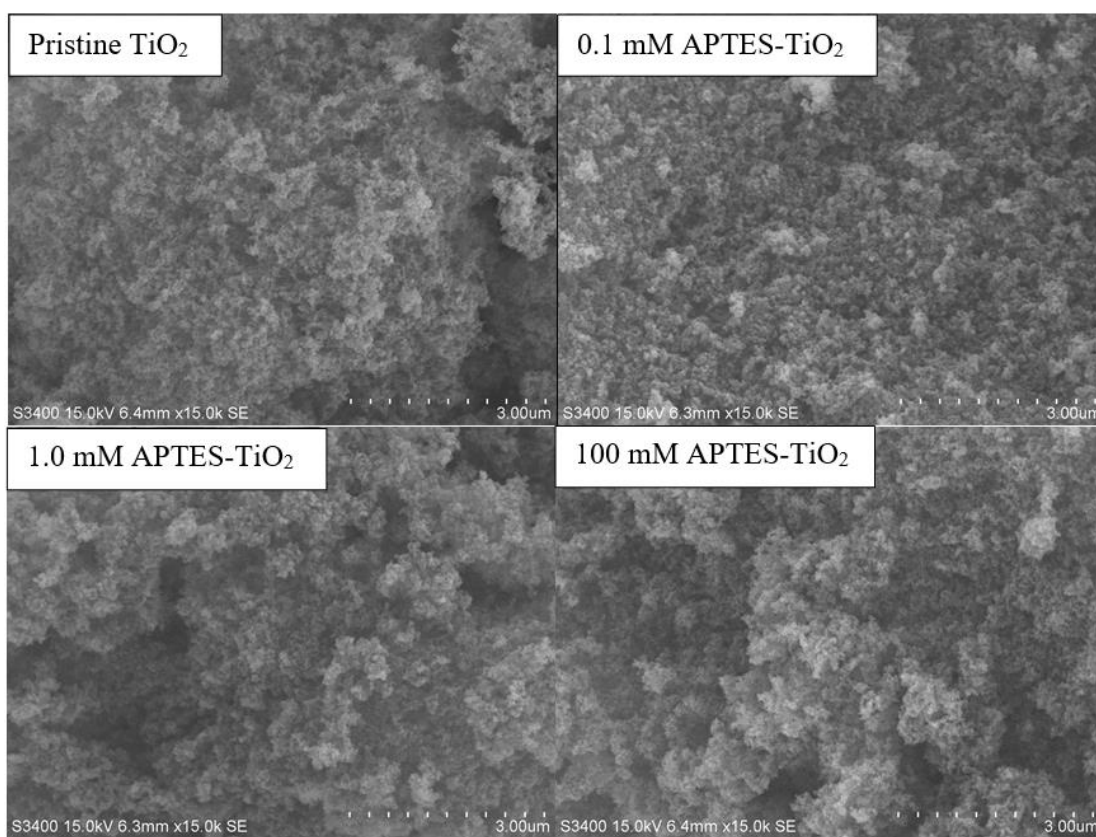
Figure 4.17 *SEM images of pristine titanium dioxide and APTES-modified titanium dioxide*

Table 4.10 *Summarization of each atomic surface from SEM-EDX analysis of pristine titanium dioxide and modified titanium dioxide*

Sample	C	N	O	Si	Ti
Pristine TiO$_2$	1.6	nd	28.4	nd	70.0
0.1 mM APTES-TiO$_2$	3.2	3.8	28.8	0.2	64.0
1.0 mM APTES-TiO$_2$	3.3	4.5	31.3	0.5	60.4
100 mM APTES-TiO$_2$	3.8	5.0	36.1	0.9	54.2

The methylene blue decolourisation activity under visible light irradiation is illustrated in **Figure 4.18**. The results showed that the photocatalytic activity of photolysis (blank test) was similar to result of pristine titanium dioxide; however, the methylene blue photobleaching of the APTES-modified titanium dioxide were higher than pristine titanium dioxide.
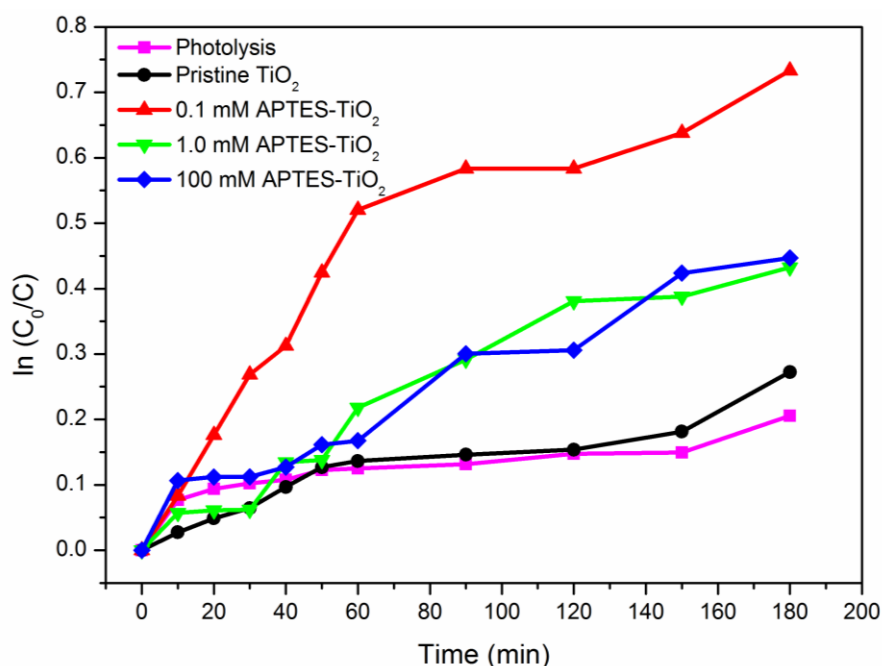
Figure 4.18 *Photocatalytic decolourisation of methylene blue of pristine titanium dioxide and APTES-modified titanium dioxide*

The decolourisation percentage of methylene blue is shown in **Figure 4.19**. It can be seen that 0.1 mM APTES-modified titanium dioxide shows the highest percentage of decolourisation (52%) > 1.0 mM APTES-modified titanium dioxide (36%) ≈ 100 mM APTES-modified titanium dioxide (35%) > pristine titanium dioxide (24%) > photolysis (19%). The stability of APTES-modified titanium dioxide have been discussing in many works. This experimental conditions indicates that the monolayer or multilayer is formed after 8 h that remains stable on the surface of titanium dioxide [230]. Moreover, during surface modification, the attachment is a competing reaction with primary bonding to render stable Ti–O–Si bonds [231]. In water, there is no

decrease of the amount of grafted APTES-modified titanium dioxide. It can be implied that the grafted layer is hydrolytically and reproducible which stable in water [232].
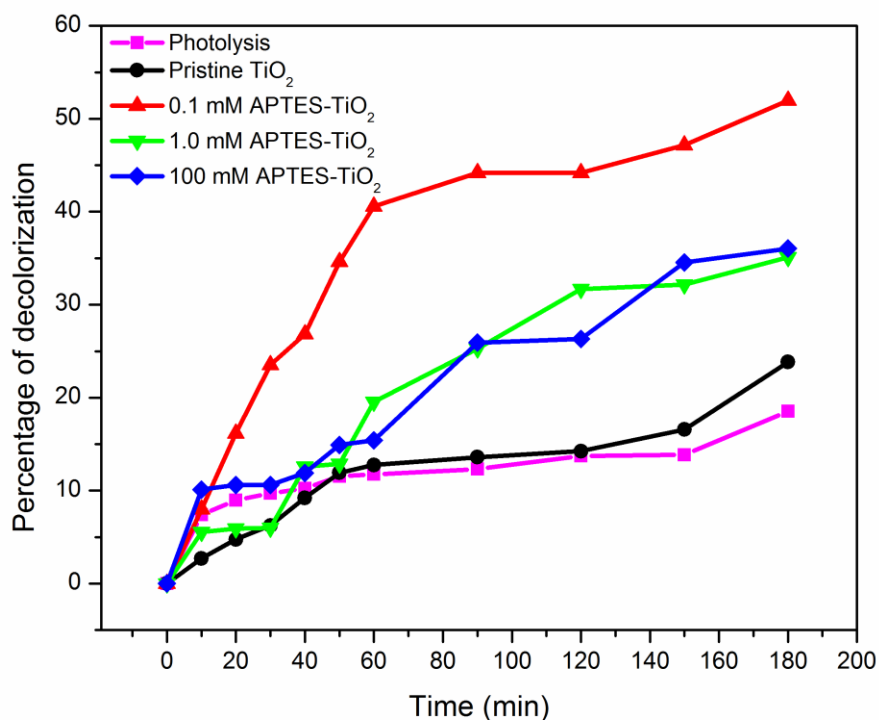
Figure 4.19 *Percentage of photodecolourisation of methylene blue of pristine titanium dioxide and APTES-modified titanium dioxide*

The degradation mechanism of methylene blue was reported by many researchers. The photocatalytic degradation of methylene blue is tested by GC-MS analysis. GC-MS analysis shows the several molecules and several single ring structures are formed [233]. It is believed that the final products of this reaction consists of CO_2, and H_2O [234]. The residual of total organic carbon (TOC) in methylene blue solutions during an illumination period was presented in **Figure 4.20**. In the case of reaction under pristine titanium dioxide after 180 mins of irradiation, the removal of TOC only reached 3.34%. However, the removal of TOC of APTES-modified titanium dioxide was almost 22.80% for 0.1 mM APTES. It can be seen that the decolourisation of methylene blue by photocatalysis also produced TOC disappearance.
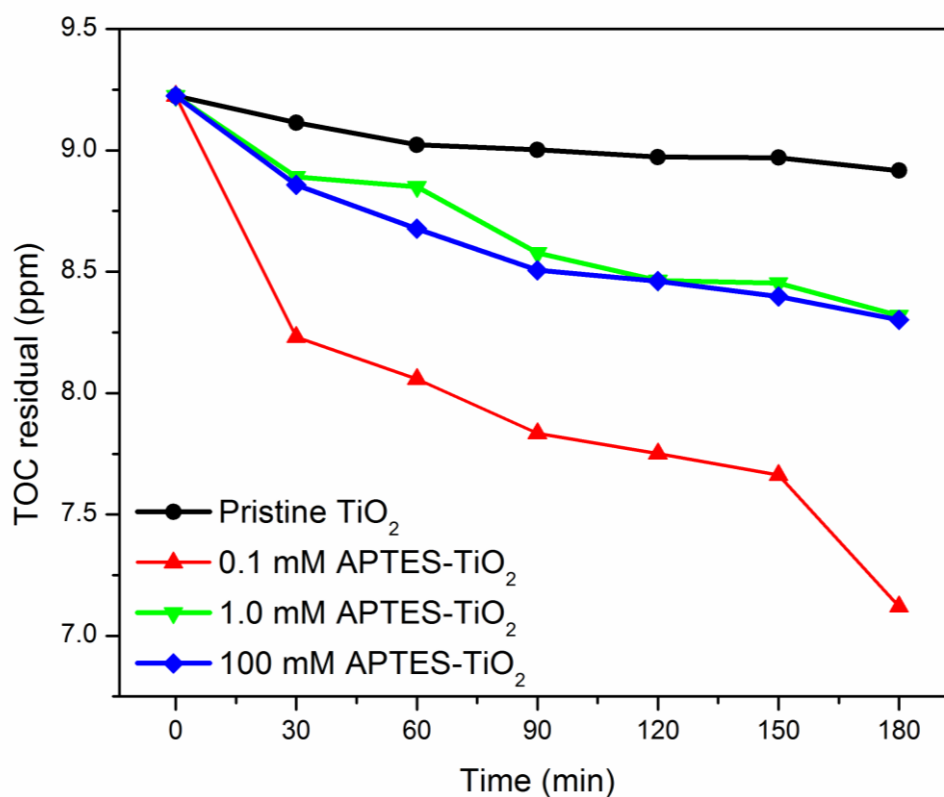
Figure 4.20 *TOC residual of photodecolourisation of methylene blue of pristine titanium dioxide and APTES modified titanium dioxide*

As above results, the APTES behaves as nitrogen-silicon-codoped in titanium dioxide that can generate intermediate level between valence band and conduction band, thus not only reducing in the band gap but also restraining the electron-hole recombination. Moreover, the monolayer and/or multilayer of amino-silane can increase the oxygen chemisorption on titanium dioxide surface, leading to improvements in the photocatalytic activity. Additional, more hydrophobicity of titanium dioxide photocatalyst can retard the photocatalytic reaction as a result less protonated amine (NH_3^+). Therefore, the suitable of APTES concentration for methylene blue photobleaching under visible light irradiation was 0.1 mM APTES-titanium dioxide which exhibited the highest photocatalytic activity.

4.3 Modification of thin film by carbon via magnetron sputtering

In this part, the carbon deposited on titanium dioxide thin film catalysts were synthesized by magnetron sputtering using carbon dioxide as a carbon source and tested in the liquid phase photodecolourisation of methylene blue. Typically, carbon modified titanium dioxide based catalysts have attracted much attention for photocatalysis applications. This part reveals the morphological, physical, chemical, and photocatalytic properties by using various means of characterization.

An overview of deposition conditions, thickness information, and compositional results for the undoped and carbon-doped titanium dioxide thin film coatings are summarized in **Table 4.11**. In terms of visual appearance, all coatings were uniform and optically transparent, with no visual signs of stresses. The colour of the coatings varied from colourless (for undoped titanium dioxide samples) to pale yellow (for coatings deposited at low flow rates of carbon dioxide) and pale brown (for coatings deposited at high carbon dioxide flow rates). It was observed that the thickness of the carbon-doped films was considerably greater than that of the undoped titanium dioxide thin films; also, a gradual increase of coating thickness was observed with increasing carbon dioxide flow rate. The thickness difference between the corresponding coatings of the arrays deposited at 25% and 30% optical emission monitoring (OEM) set points was minimal, while array coatings at 35% OEM signal were considerably thicker, both in the case of undoped and carbon-doped samples. As established from earlier work, using a 25% OEM set point resulted in a titanium-to-oxygen ratio close to the stoichiometric 2:1. For undoped coatings deposited at higher OEM set points, the ratio of Ti:O was slightly higher. Carbon content in the doped coatings varied from 4 to 6.4 wt %. Unsurprisingly, coatings deposited at higher OEM set points (i.e., lower O_2 content) were characterized with higher carbon content, as titanium preferentially reacts with oxygen, and creating oxygen deficiencies promotes carbon incorporation. Similar trends were seen as the carbon dioxide flow was increased.

Table 4.11 *Summary of the deposition conditions, thickness, and compositional properties of undoped and carbon-doped titanium dioxide thin films on glass substrate*

Sample ID	OEM Setpoint, % FMS	CO_2 Flow, sccm	Thickness, nm[a]	Ti, at. %[b]	O, at. %[b]	C, at. %[b]
T25	25	-	490	34.9	65.1	-
T25C2.5	25	2.5	820	32.9	62.5	4.5
T25C5	25	5	860	32.9	61.6	5.0
T25C7	25	7	870	35.2	59.4	5.5
T30	30	-	510	40.9	59.1	-
T30C2.5	30	2.5	820	33.9	62.0	4.1
T30C5	30	5	870	33.5	60.8	5.3
T30C7	30	7	910	35.8	58.6	5.6
T35	35	-	600	40.2	59.8	-
T35C2.5	35	2.5	840	33.6	60.7	4.7
T35C5	35	5	1300	34.1	59.8	6.1
T35C7	35	7	1500	36.7	56.9	6.4

[a] Stylus profilometry results

[b] energy dispersive X-ray spectroscopy (EDX) results

Examples of SEM images for carbon-doped titanium dioxide and undoped titanium dioxide thin films deposited at 35% OEM set point are shown in **Figure 4.21**. It is evident that all films were characterized with relatively smooth surfaces consisting of small densely packed grains, as typically observed for titanium dioxide and doped titanium dioxide films deposited by reactive magnetron sputtering [109, 235]; no obvious defects could be seen on the film surfaces.
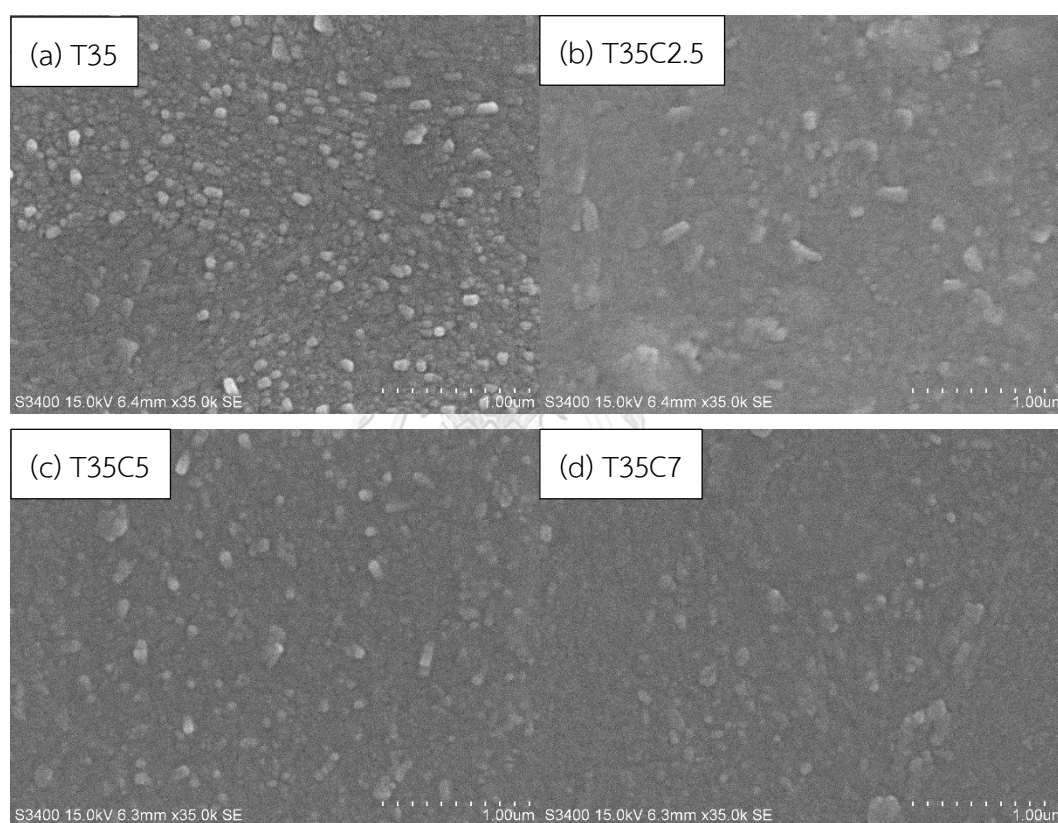
Figure 4.21 *Scanning electron microscopy (SEM) images of selected titanium dioxide and carbon-doped titanium dioxide coatings deposited on glass substrate (a) T35; (b) T35C2.5; (c) T35C5; (d) T35C7.*

Morphological properties of the coatings (surface area and surface roughness) were studied with atomic force microscopy (AFM); the data on surface area and surface roughness values are presented in **Table 4.12**. The surface area of all deposited films was around 900 μm^2; the variations of surface area between different samples was <1% for undoped and carbon-doped coatings. The roughness of the films obtained by AFM showed that coatings deposited at higher carbon dioxide flow rates were characterized with higher roughness values.

Table 4.12 *Summary of the surface properties by AFM characterisation of undoped and carbon-doped titanium dioxide films on glass substrate*

Sample ID	Surface Roughness, nm	Surface Area, μm^2
T25	5.7	902
T25C2.5	6.0	901
T25C5	4.2	901
T25C7	13.0	902
T30	6.0	901
T30C2.5	5.8	901
T30C5	5.8	901
T30C7	10.0	902
T35	6.2	911
T35C2.5	12.8	902
T35C5	11.0	902
T35C7	12.4	902

Examples of AFM images for carbon-doped titanium dioxide and undoped titanium dioxide thin films deposited at 35% OEM set point are shown in **Figure 4.22**. The differences in the surface topography of the films, from relatively smooth to the dense domains as a result of increasing carbon dioxide flow. Despite the considerable difference in film thicknesses, similar values of surface area mean that the photocatalytic performance of the samples could be compared directly, rather than being normalized per unit of surface area, as is typically done when comparing the photocatalytic activity of samples with largely different surface areas [236].

(a) T35C2.5
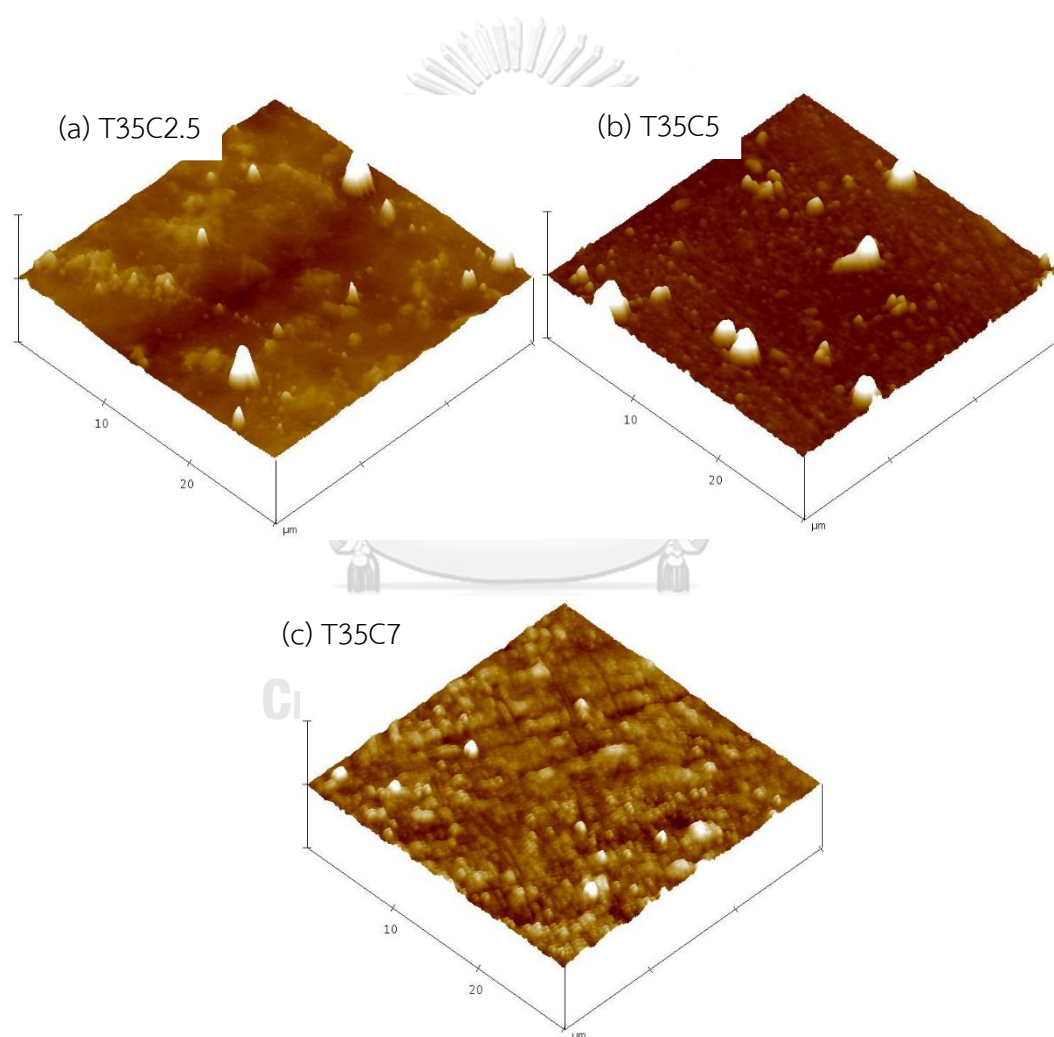
(b) T35C5

(c) T35C7

Figure 4.22 *AFM images of selected carbon-doped coatings deposited on glass substrate (a) T35C2.5; (b) T35C5; (c) T35C7.*

X-ray diffraction (XRD) analysis was employed to characterize the crystal structure of the undoped and carbon-doped thin films fabricated in this study. The XRD patterns of all samples before annealing were indicative of amorphous or weakly crystalline structures. After annealing, all samples were crystalline; sharp peaks observed at 2θ ca. 25.3°, 37.7°, 48.0°, 55.0°, and 68.8°on the diffraction patterns of all the analysed samples can be identified as titanium dioxide anatase phase peaks (crystallographic card number 96-900-8215). **Figure 4.23** shows the XRD patterns of undoped and carbon-doped titanium dioxide thin films deposited at 25% OEM set point after isothermal annealing in air at 873 K.
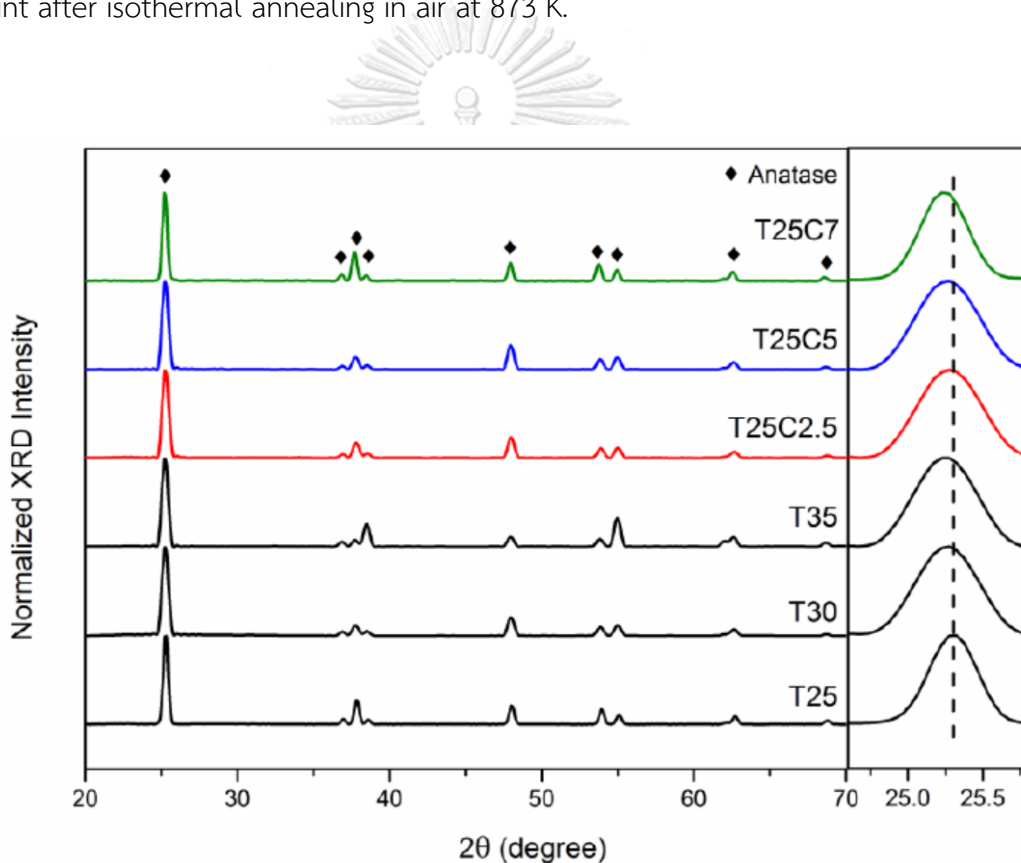
Figure 4.23   X-ray diffraction (XRD) patterns of selected carbon-doped and undoped titanium dioxide coatings (25% optical emission monitoring (OEM) set point) deposited on glass substrates and annealed at 873 K.

No peaks that could be attributed to the other titanium dioxide crystal phases (rutile and brookite) were seen on the diffraction patterns. It can be seen that for the films produced at higher flows of carbon dioxide, the peaks were shifted to slightly lower values; this can be indicative of crystal lattice deformation as the result of carbon introduction. This shift is typically explained by the lattice distortion of titanium dioxide due to internal stress (carbon inclusion in this case), which caused the expansion of the unit cell volume [237]. Overall, the carbon incorporation in titanium dioxide does not cause any crystal phase transformations of titanium dioxide, as all deposited films were in the anatase phase with a (101) preferred orientation, regardless of the OEM set point and carbon dioxide flow variations.

To examine the species and the bonding states of all elements in the deposited undoped and carbon-doped titanium dioxide thin films, XPS spectra were recorded and deconvoluted. The XPS survey scans of all samples showed the presence of titanium and oxygen; a carbon peak was also seen for all carbon-doped titanium dioxide thin films (**Figure 4.24**). Gaussian functions were used to deconvolute the Ti *2p*, O *1s*, and C *1s* spectra. Ratios of titanium/oxygen on the surface calculated based on the XPS data were in good correlation with the bulk composition of the coatings estimated based on the EDX data (given in **Table 4.11**).
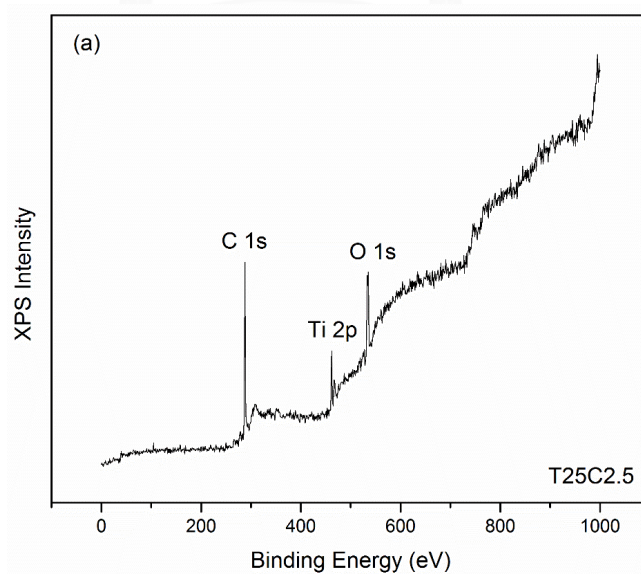
Figure 4.24 *X-ray photoelectron spectroscopy (XPS) results of selected C-doped samples: (a) Survey spectrum (sample T25C2.5)*
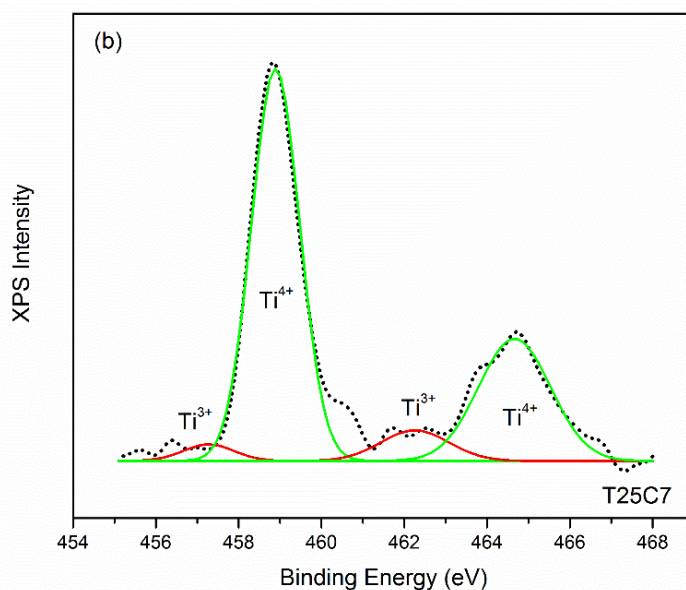
Figure 4.25 *X-ray photoelectron spectroscopy (XPS) results of selected C-doped samples: Ti 2p spectrum (sample T25C7)*

Figure 4.25 shows an example of a high resolution XPS spectra for Ti *2p* (sample T25C7). The two strong peaks at binding energies of 458.8 and 456.4 eV were observed for all titanium dioxide thin films and can be assigned to Ti^{4+} $2p_{3/2}$ and Ti^{4+} $2p_{1/2}$, respectively [238]. Interestingly, for the films deposited at higher carbon dioxide flows (5 and 7 sccm) the presence of Ti^{3+} can be seen on the XPS spectra—Ti^{3+} $2p_{3/2}$ and Ti^{3+} $2p_{1/2}$ at 457.3 and 462.3 eV, respectively. At the same time, no evidence of the presence of Ti^{3+} could be seen on the XPS spectra of the undoped and carbon-doped titanium dioxide thin films deposited at a low (2.5 sccm) flow of carbon dioxide. To quantify the observed effect, the ratio of Ti^{3+}/Ti^{4+} was calculated for each sample (given in **Table 4.13**). Apparently, the ratio of the Ti^{3+} to Ti^{4+} states increased with increasing the carbon dioxide flow rate. Ti^{3+} is typically reported as a surface defect of titanium dioxide that plays an important role for photocatalysis and the photoinduced hydrophilicity phenomenon. It can also act as an active site for oxygen desorption, prevent the electron-hole recombination process, and enhance visible light activity [239, 240]. The Ti *3d* peak at 455 eV that is typically assigned to Ti–C bonds could not be detected, but the existence of Ti-C bonds was confirmed on the high resolution C *1s* spectrum [241].

Table 4.13 *Summary of the surface properties by XPS characterisation of undoped and carbon-doped titanium dioxide films on glass substrate.*

Sample ID	Ti^{3+}/Ti^{4+}	Ti–C, at. %	C–O, at. %	Ti–C–O, at. %
T25	-	-	-	-
T25C2.5	-	0.06	0.28	0.28
T25C5	0.02	0.09	0.72	0.39
T25C7	0.03	0.18	0.34	0.48
T30	-	-	-	-
T30C2.5	-	0.08	0.39	0.16
T30C5	0.02	0.13	0.55	0.42
T30C7	0.04	0.27	0.49	0.34
T35	-	-	-	-
T35C2.5	-	0.11	0.37	0.51
T35C5	0.02	0.18	0.74	0.32
T35C7	0.06	0.31	0.49	0.46

Figure 4.26 shows an example of the high resolution O *1s* spectrum (sample T25C7) and its deconvolution into three peaks. The peak at 530.2 eV is assigned to the lattice oxygen of titanium dioxide [242], while two other peaks at 532.1 and 534.6 eV correspond to C–O and C=O bonds, respectively [243]. For all carbon-doped titanium dioxide thin films, the binding energies exhibited a slight positive shift, which can be explained by carbon incorporation into the titanium dioxide lattice [244].
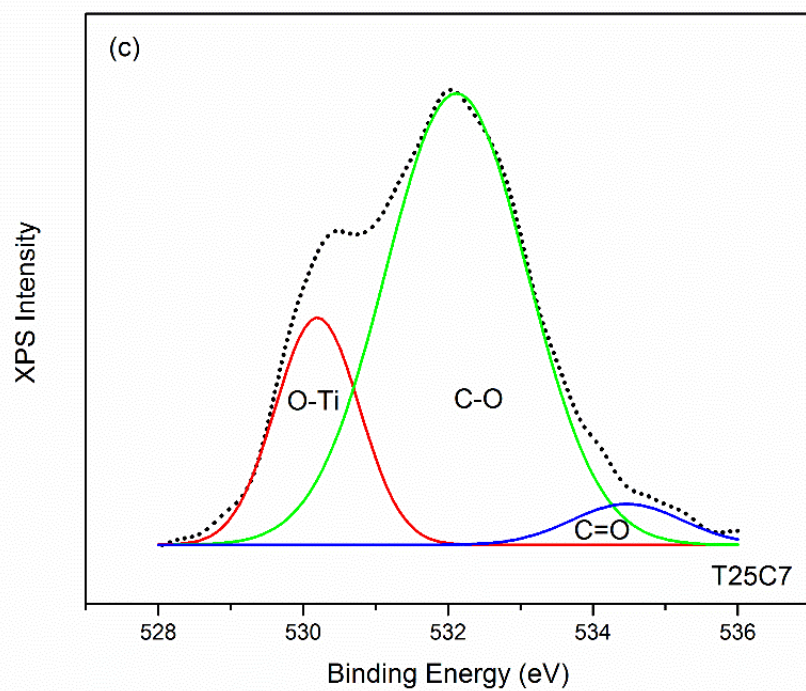
Figure 4.26 *X-ray photoelectron spectroscopy (XPS) results of selected C-doped samples: c) O 1s spectrum (sample T25C7)*
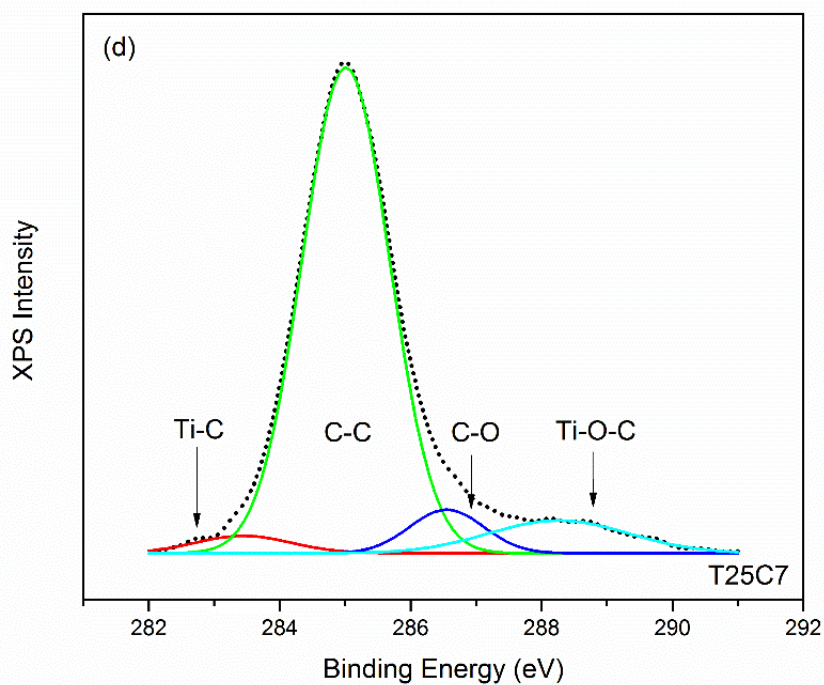
Figure 4.27 *X-ray photoelectron spectroscopy (XPS) results of selected C-doped samples: (d) C 1s spectrum (sample T25C7).*

Figure 4.27 shows an example of the high resolution C *1s* XPS profile of the carbon-doped titanium dioxide thin film (sample T25C7) deconvoluted into four peaks. The major broad peak at 285 eV is typically assigned to contaminant hydrocarbons (C–C) [245]. It is often reported that this peak disappears with increasing Ar$^+$ etching time during the XPS measurement [246]. Contaminant carbon species are typically believed to not contribute to the visible light photocatalytic activity, however several works suggest that carbon may exist in the grain boundaries of titanium dioxide and therefore acts as a photosensitizer [247, 248]. The peak at 283.4 eV corresponding to the titanium-carbon bond (Ti–C) [249] was observed for all carbon-doped titanium dioxide thin films. The presence of this peak indicates the substitution of oxygen atoms by carbon atoms as the result of carbon-doping (substitutional doping). The Ti–C bonding percentage was estimated using the relative areas of the peak at 283.4 eV and is shown in **Table 4.13**. This confirms the presence of carbon bonded in the titanium dioxide matrix. It can be concluded that the carbon atoms were substituted in some lattice oxygen sites not only at the surface but also in the bulk region, and the carbon concentration was increased with increasing carbon dioxide flow rate. Two peaks at 286.6 eV and 288.3 eV can be attributed to the oxygen bound species, C–O and Ti–C–O, respectively, confirming the fact that some carbon was incorporated into the titanium dioxide lattice in place of Ti atoms (interstitial doping) [107]. The atomic percentage of C doping in place of Ti atoms was estimated using the relative areas of the peaks at 288.3 eV and is given in **Table 4.13**. Reportedly, carbon substitution of both oxygen and titanium atoms, as well as the presence of the carbonate species (C–O) can contribute to enhanced visible light photocatalytic activity through band gap narrowing [104].

Optical band gaps of undoped and carbon-doped titanium dioxide thin films were calculated using the Tauc plot method, by plotting $(\alpha h\nu)^{1/2}$ as a function of $h\nu$ and extrapolating the linear region to the abscissa (where α is the absorbance coefficient, h is Plank's constant, ν is the frequency of vibration) [250]. Graphical examples of the band gap calculation of selected samples are given in **Figure 4.28** (films deposited at 35% OEM set point). Calculated band gap values of all the coatings

studied are given in **Table 4.14**, along with the other analytical results. According to the calculation results, band gap values of undoped titanium dioxide thin films deposited at 25%, 30%, and 35% OEM set point values were 3.22, 3.20, and 3.18 eV, respectively. These numbers are in good agreement with the data typically reported for anatase titanium dioxide (ca. 3.2 eV). It is obvious from the data presented that increasing the carbon dioxide flow rate, along with increasing the OEM set point resulted in remarkable red shifts of the absorbance edge. The large shift in band gap towards the visible light region (up to 1.2 eV—for sample T35C5, compared to undoped titanium dioxide) is due to the inclusion of carbon into the titanium dioxide crystal lattice and subsequent band gap narrowing. Despite the different positions of the carbon atoms that may occur as a result of carbon-doping (incorporation in the titanium dioxide structure as Ti–C, Ti–C–O, and carbonate species), it is generally accepted that band gap narrowing is a result of the existence of mid-gap state(s) caused by mixing of the C *2p* and O *2p* states [104].
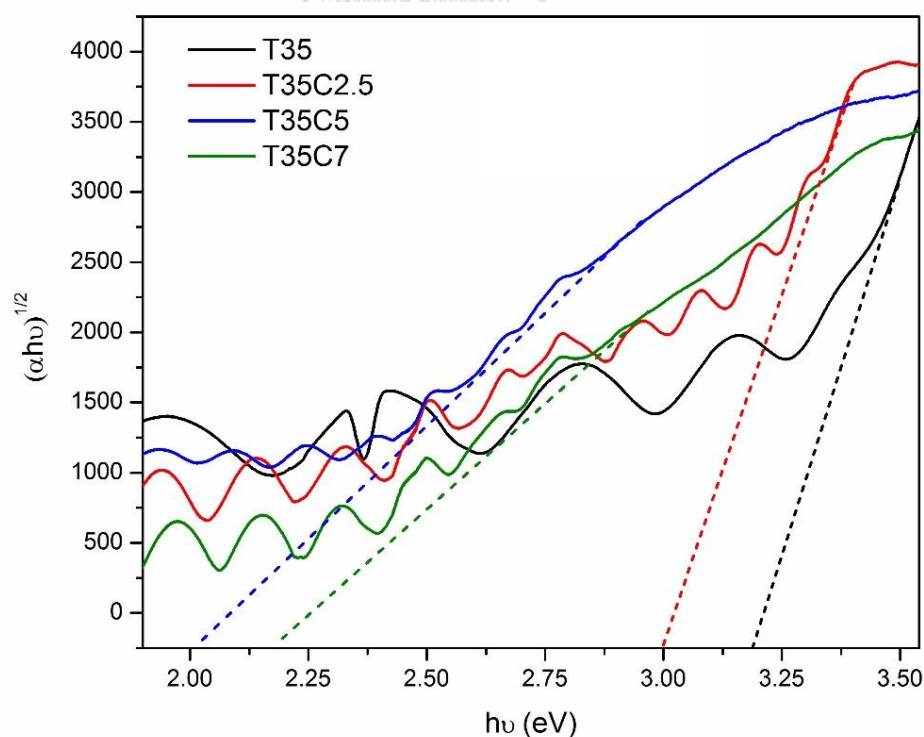
Figure 4.28 *Examples of band gap calculations for selected carbon-doped and undoped titanium dioxide samples (deposited at 35% OEM set point).*

Table 4.14 Summary of the band gap values by transmittance calculation of undoped and carbon-doped titanium dioxide films on glass substrate.

Sample ID	Band Gap, eV
T25	3.22
T25C2.5	3.13
T25C5	3.15
T25C7	3.08
T30	3.20
T30C2.5	3.04
T30C5	3.05
T30C7	2.63
T35	3.18
T35C2.5	3.00
T35C5	2.02
T35C7	3.22

Titanium dioxide-based surfaces are known for their ability to exhibit reversible wettability behaviour, becoming superhydrophilic upon sub-band gap photoexcitation and returning to their original wettability as the irradiation stops [251, 252]. Water droplet contact angle (CA) measurements were performed here to study the wettability of the thin films upon UV and visible light irradiation; the results are given in **Table 4.15**.

Table 4.15 Results of wettability measurements of carbon-doped and undoped titanium dioxide coatings annealed at 873 K.

Sample ID	Initial CA, deg.	CA after 1 h UV, deg.	CA after 1 h vis, deg.
T25	92	18	55
T25C2.5	60	10	15
T25C5	11	~0	~0
T25C7	11	~0	~0
T30	53	13	20
T30C2.5	58	13	16
T30C5	11	~0	~0
T30C7	10	~0	~0
T35	54	10	22
T35C2.5	63	12	14
T35C5	10	~0	~0
T35C7	10	~0	~0

It can be seen that the undoped titanium dioxide coatings and coatings produced at 2.5 sccm carbon dioxide flow rate showed the highest values of contact angle both before and after irradiation. Thus, the contact angle values of sample T25 change from 92° to 18° and 55° after 60 min of UV and visible irradiation, respectively. While the initial contact angles of the undoped samples T30 and T35 were lower compared to T25 (53°), neither of these samples reached a superhydrophilic state after 1 h of irradiation. Whilst the initial values of the carbon-doped thin films produced at 2.5 sccm carbon dioxide flow rate were comparable to those of undoped titanium dioxide, the contact angle reduction under both UV and visible light irradiation was greater in this case. At the same time, wettability properties of the carbon-doped coatings produced at higher flow rates of carbon dioxide (5 and 7 sccm) were remarkably different. These coatings exhibited superhydrophilicity (contact angle ca. 10°) prior to the light irradiation, with perfect wettability (a zero contact angle) after irradiation with either UV or visible light. However, this phenomenon was unsurprising, considering the presence of Ti^{3+} states observed with XPS for these samples. It is a frequently reported fact that an increased number of Ti^{3+} states on the surface results in considerably higher hydrophilicity [253]. Therefore, the lowest contact angle values both prior to and after irradiation in this study were observed for the samples that earlier showed the presence of Ti^{3+} states on their surfaces.

To investigate the effect of carbon-doping on the photocatalytic activity of titanium dioxide thin films, two types of photocatalytic tests were used in this work; namely the decomposition of methylene blue and stearic acid. The methylene blue decomposition reaction was approximated to pseudo first order kinetics and the reaction constants for the samples studied are given in **Table 4.16**.

Table 4.16 Results of photodecolourisation of methylene blue tests of carbon-doped and undoped titanium dioxide

Sample ID	Kinetic constant, $k \times 10^5$, s^{-1}	
	under UV light	under visible light
T25	1.8	0.5
T25C2.5	1.8	1.5
T25C5	1.3	1.0
T25C7	1.4	0.8
T30	1.4	0.9
T30C2.5	0.8	0.9
T30C5	0.7	1.5
T30C7	0.8	1.4
T35	1.4	0.9
T35C2.5	0.9	1.0
T35C5	1.0	2.1
T35C7	1.4	2.0

Examples of methylene blue decay rates for the selected samples under UV and visible light irradiation are shown in **Figure 4.29**. The results under UV light irradiation are shown in **Figure 4.29**a. According to the Lambert—Beer law, the concentration of the dye is proportional to the absorbance decay. The apparent first order rate constant, k_a, was used as a quantitative characterization of the photocatalytic degradation rate of MB. Values for k_a were found from the gradient of the graph of $A_t/A_{t=0}$ versus experiment time ($A_{t=0}$ and A_t are the peak absorbance values of the methylene blue solution at 664 nm at time 0 and time of experiment, respectively). The methylene blue degradation rate constants for undoped titanium dioxide thin films were around $1.4–1.8 \times 10^{-5}$ s^{-1}. As can be seen from the data presented in **Table 4.16**, carbon doping did not help to improve UV light photocatalytic activity in this case; the rate constants of all carbon-doped samples were equal to or lower than those of the undoped titanium dioxide samples.

Figure 4.29b shows the selected methylene blue photocatalytic degradation under visible light irradiation. All undoped titanium dioxide thin films showed low rates of methylene blue decay under visible light irradiation with kinetic constants below 1 $\times 10^{-5}$ s^{-1}, and no significant variation of the kinetic constant values was seen for undoped titanium dioxide coatings produced at different OEM set points. However, the carbon-doped samples showed higher photocatalytic activity under visible light irradiation. Generally, the ability to photodegrade methylene blue under visible light irradiation increased with increasing OEM set point along with increasing carbon dioxide flow rate. Of the samples studied, the highest methylene blue decay rates under visible light irradiation were seen for samples T35C5 and T35C7. Given that the band gap value is indicative of light absorbance, it is no surprise that samples T35C5 and T35C7 with the lowest band gap values (and consequently the highest visible light absorbance) proved the most active under visible light conditions.
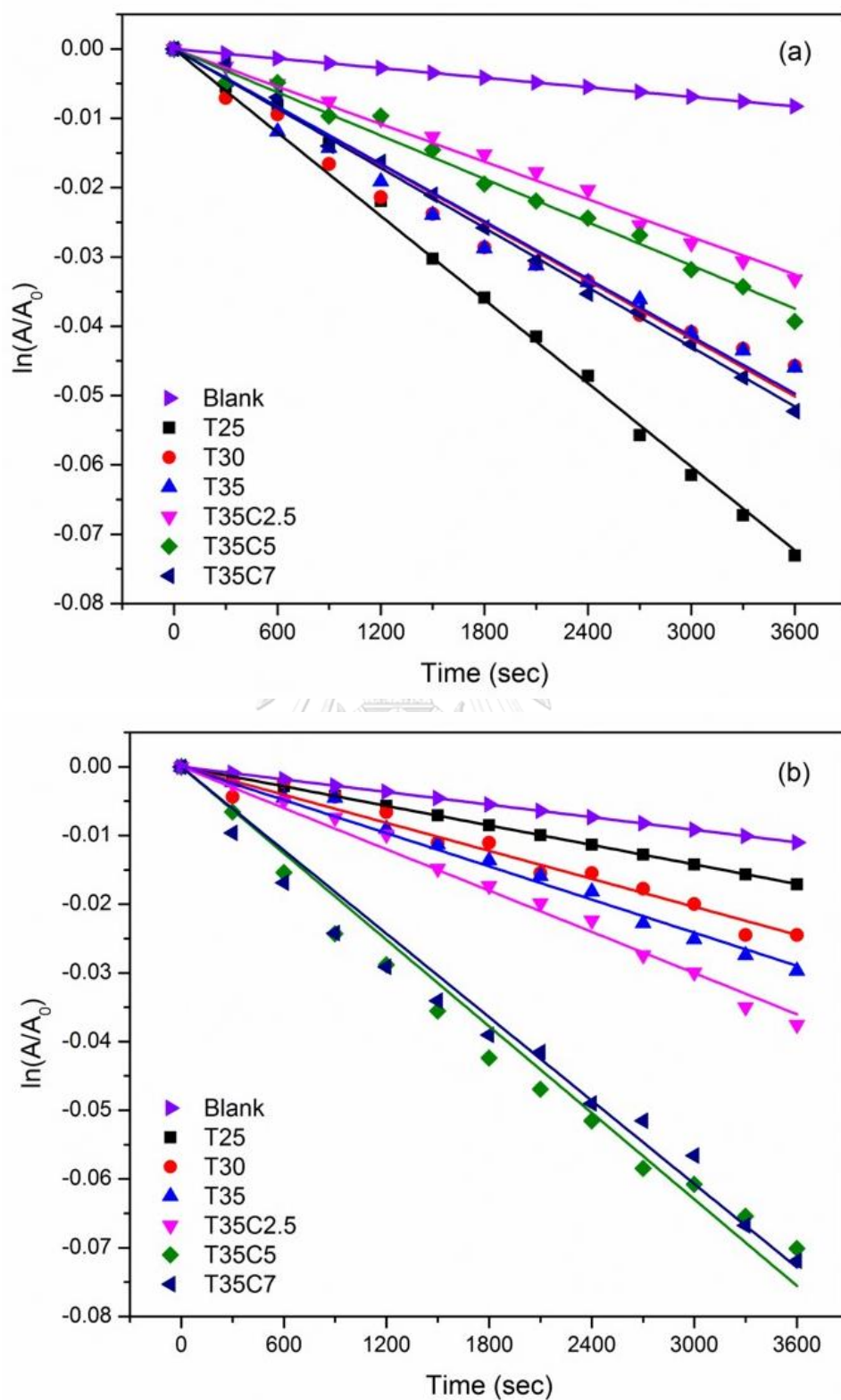
Figure 4.29 *Kinetics plot of selected thin films of methylene blue decolourisation under (a) UV and (b) visible light irradiation.*

Photocatalytic degradation of stearic acid, a common model pollutant for assessing self-cleaning properties of photocatalytic coatings, was monitored with FTIR through the disappearance of stearic acid absorbance peaks. Reaction rate constants were calculated for the quantitative characterisation of the degradation process under UV and visible light (presented in **Table 4.17**).

Table 4.17 Results of photodegradation of stearic acid tests of carbon-doped and undoped titanium dioxide

Sample ID	Kinetic constant, k × 10² , A cm⁻¹ h⁻¹	
	under UV light	under visible light
T25	4.0	0.4
T25C2.5	0.8	0.6
T25C5	1.1	0.3
T25C7	1.0	0.2
T30	1.6	0.7
T30C2.5	1.2	0.1
T30C5	1.3	0.2
T30C7	0.7	0.2
T35	2.3	0.9
T35C2.5	0.4	0.1
T35C5	0.9	0.3
T35C7	1.3	0.6

As the stearic acid has three strong absorption peaks at 2958, 2923, and 2853 cm^{-1}, the model pollutant decomposition was monitored here by Fourier transform infrared spectroscopy (FTIR), using a Perkin Elmer Spectrum Two IR spectrometer (Perkin Elmer, Waltham, MA, USA), in the range 2700–3000 cm^{-1} every 24 h. FTIR spectra were collected in absorbance mode and the amount of stearic acid on the surface of each sample was evaluated through the integrated area under the corresponding FTIR absorbance spectrum. Prior to the experiments with photocatalytic surfaces, the test was carried out on pieces of uncoated glass. As no significant stearic acid peak reduction was detected on plain glass under either of the two light sources used, it can be concluded that stearic acid films were stable under both UV and visible light. Examples of the decay of the integrated area under the stearic acid absorbance spectrum for selected samples are given in **Figure 4.30**. From the data presented in **Table 4.17**, it is obvious that the highest degradation rates under UV light were recorded for undoped titanium dioxide thin films, and in particular for T25. It is obvious that carbon doping had a detrimental effect on the coatings' ability to degrade stearic acid. No improvement of photocatalytic activity for carbon-doped coatings could be seen under visible light either. While selected carbon-doped coatings outperformed sample T25, the overall rates of stearic acid degradation under visible light remained rather low.
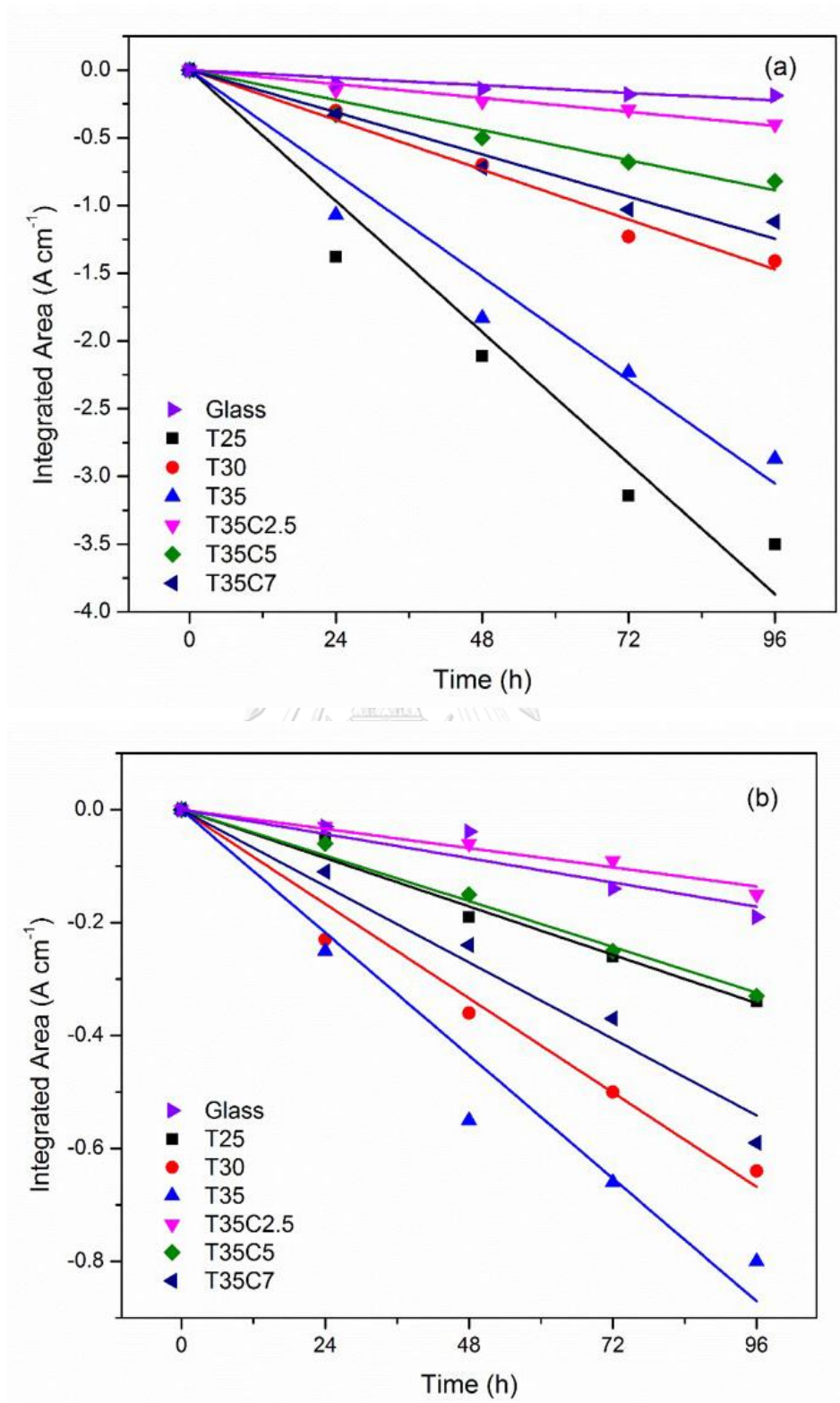
Figure 4.30 *Plots of the integrated area changes of the FTIR spectra of the stearic acid peaks (3000–2700 cm^{-1}) for selected carbon-doped and undoped titanium dioxide samples under: (a) UV light irradiation; (b) visible light irradiation.*

Two types of photocatalytic tests were used in this work to cross-verify whether the incorporation of carbon into the titanium dioxide lattice had a positive effect on photocatalytic activity. The stearic acid test was also used because the suitability of the dye degradation test is often questioned as a method for the determination of visible light activity [254]. Though no direct correlation between quantitative results of these two testing methods was found here, both sets of results were indicative of the fact that carbon-doping had a rather detrimental effect on the UV light photocatalytic activity of the samples, while improvement of the visible light activity was found only for two samples of the array (T35C5 and T35C7). As for visible light induced stearic acid degradation, the overall low levels of photocatalytic activity seen under visible light makes it difficult to quantify the activity precisely. Despite the fact that authors often report the correlation between the results of different photocatalytic tests [255, 256], the examples of non-correlative results are also often reported [99]. This is evidence of the fact that some model pollutants can be decomposed much more easily than others.

Despite the widely published information that carbon doping is an efficient method of enhancement of UV and introduction of visible light photocatalytic activity, the present work confirms the fact that the properties of a photocatalytic material depend greatly on the production method, phase composition of titanium dioxide, position of carbon in titanium dioxide lattice, etc. It is frequently stressed in the literature that the exact mechanism of the enhancement of titanium dioxide photocatalytic properties via carbon-doping is not yet fully understood [104]. The majority of the work reporting significant improvements of photocatalytic activity for carbon-doped titanium dioxide thin films report carbon found either in the interstitial [257, 258] or in substitutional [111, 259] position, while all of the carbon-doped films deposited in the present work reveal carbon in both positions in the same film. Similar results observed for nitrogen-doped samples may suggest that the presence of dopants in both positions may cancel out the effect, as compared to the samples where the dopant is found only in one of the positions [260]. It is also frequently mentioned in the literature that, for doped titanium dioxide, excessive dopant may act

as recombination sites, therefore lowering the photocatalytic activity. We assume that this hypothesis was the reason for the lower overall photocatalytic activity of the carbon-doped coatings produced here, as compared to undoped titanium dioxide. This suggestion is supported by the fact that the UV-induced activity of carbon-doped photocatalysts for all samples was lower than that for undoped titanium dioxide. Consequently, it may be concluded that the use of carbon-doped photocatalysts produced via magnetron sputtering with carbon dioxide gas as the source of carbon is practical, only when the extension of the absorption spectrum into the visible range is more important than the efficient use of UV photons, and when the pollutants are relatively easy degradable [99].

4.4 Grafting of titanium dioxide on PMMA film via ATRP

In this part, the grafting of titanium dioxide on PMMA film via ATRP in order to increase the reusability process has been investigated and catalytic performances of for photodecolourisation of methylene blue under UV light irradiation was studied.

The completion of hydroxyl-end group by thiol-ene click Michael addition was monitored by the transmittance of FT-IR. **Figure 4.31** shows the transmittance spectra of all chemicals in the **Figure 3.2**. After the thiol-ene click Michael addition between MEMO and 4HBT, the peak at 2841 cm^{-1} which referred to the methoxy group (R-O-CH_3) in MEMO was found in MEMO-OH [261]. The broaden peak at 2560 cm^{-1}, referring to the thiol group (R-SH) stretch vibrational peak, was found in 4HBT but disappears completely in MEMO-OH [262]. The peak at 1637 cm^{-1}, which referred to carbon-carbon double bonds (-C=C-) in MEMO, disappeared completely in MEMO-OH [262]. The hydroxyl group (-OH) stretch between 3100-3500 cm^{-1} was present in the product [263].
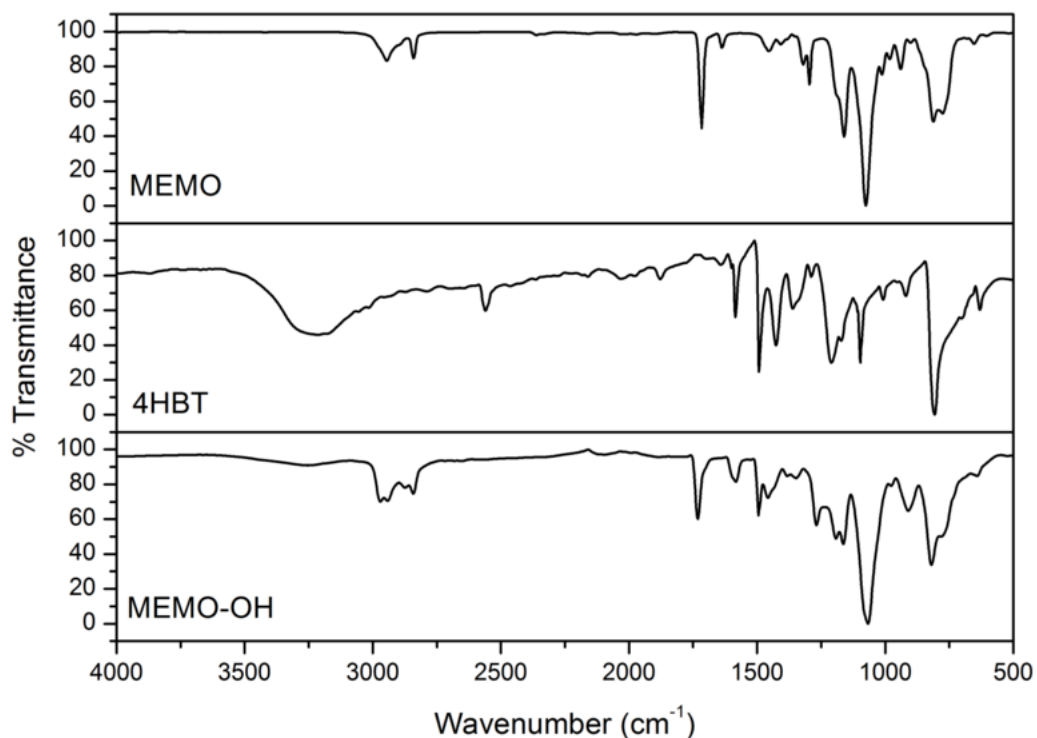
Figure 4.31 *The FT-IR spectra of reactants and product in Figure 3.2*

The structure of MEMO-OH was confirmed in **Figure 4.32** by ^{1}H NMR spectrum. The solvent DMSO-d_6 was used as the reference spectrum at 2.50 ppm [264]. The characteristic signal at around 2.9 ppm and 6.6-7.3 ppm is assigned to the newly formed proton carbon-sulphur (-C-S-) linkage and aromatic ring [265, 266], respectively. The proton in hydroxyl-end group showed a broad signal peak at 4.1 ppm which showed the presence of hydroxyl on MEMO-OH [267].
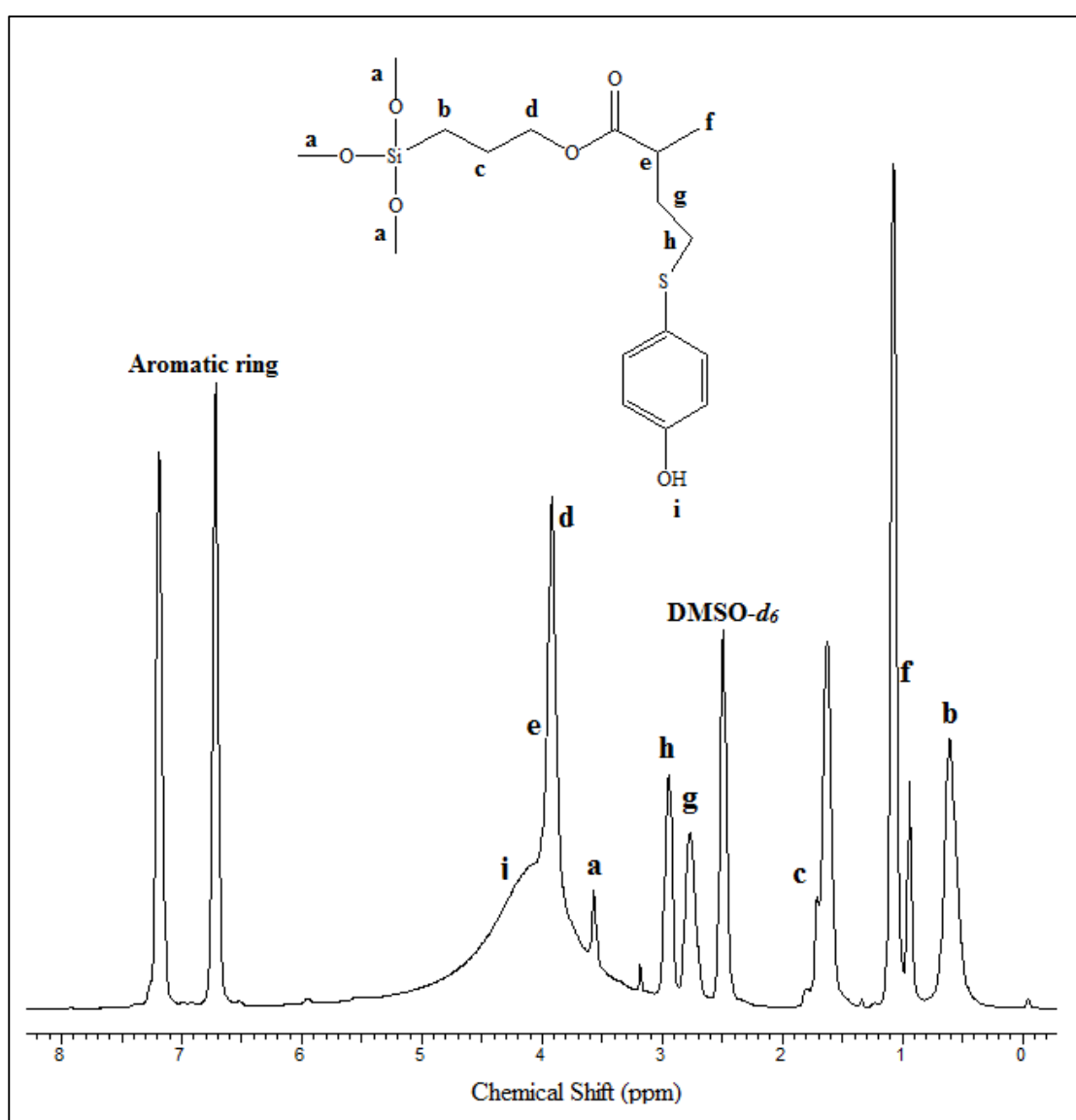
Figure 4.32 ^{1}H NMR signal spectra of MEMO-OH

The macroinitiator formation was used at the second step to form the bromide end group of MEMO-OH with a BIBB. The structure of MEMO-Br was identified by ^{1}H NMR signal spectra, which dissolved in DMSO-d_6 and was used as the reference spectrum at 2.5 ppm, is displayed in **Figure 4.33**. The ^{1}H NMR spectra of MEMO-Br shows the absence of peak of hydroxyl-end group at 4.1 ppm and the peak at 1.9 ppm is assigned to methyl terminal group (-CH$_3$) in the MEMO-Br was detected [267, 268]. It indicates that the hydroxyl-end group in the MEMO-OH was linked with the BIBB at this position where Br occurred.
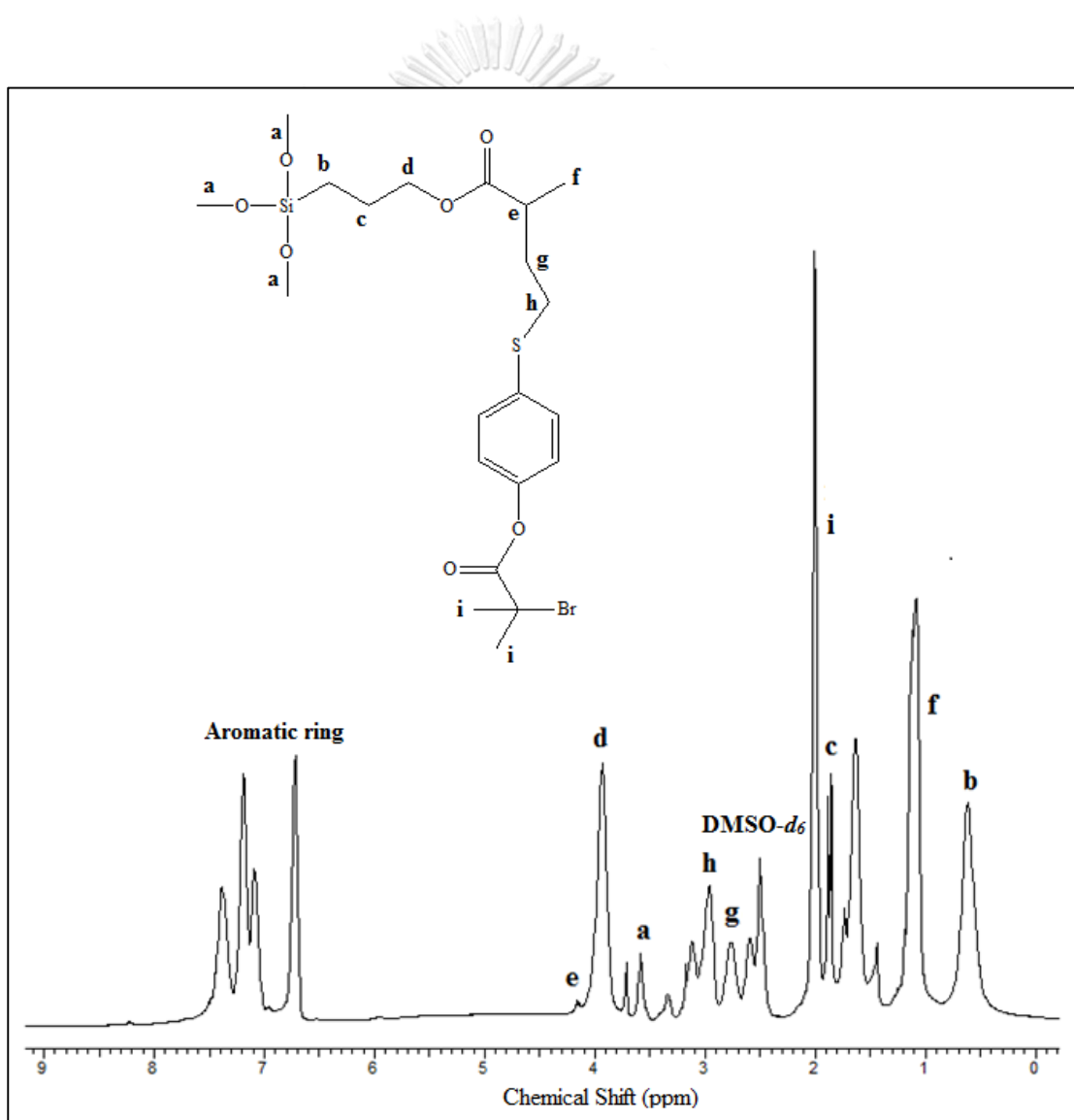
Figure 4.33 ^{1}H NMR signal spectra of MEMO-Br

The structure of MEMO-Br was also identified by the ^{13}C NMR signal spectra which dissolved in DMSO-d_6. The solvent DMSO-d_6 was used as the reference spectrum at 39.52 ppm [269], as displayed in **Figure 4.34**. The ^{13}C NMR spectra of MEMO-Br shows the carbon signal of carbon-silica linkage (-C-Si-), methyl terminal group occupied with oxygen (-O-CH$_3$), carbon-carbon linkage (-C-C-), carbon on different position in the aromatic ring and carbon doubled bond oxygen (-C=O-) at 8, 57, 66, 110-160 and 170 ppm [270-274], respectively. The methyl terminal group of BIBB appeared at the 31 ppm signal in MEMO-Br [275].
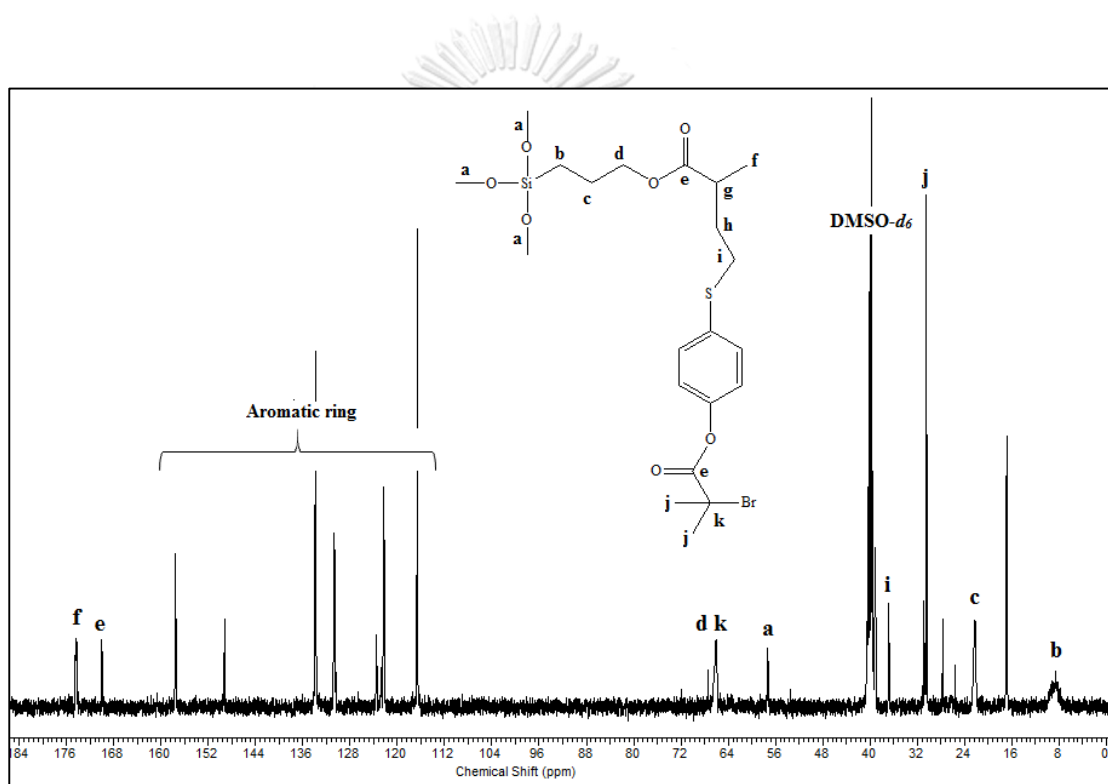
Figure 4.34 ^{13}C NMR signal spectra of MEMO-Br

For the next step, the polymer surface initiated was prepared by ATRP with MMA monomer. The MEMO-PMMA-Br was characterized by ^{13}C NMR signal spectra and is shown in **Figure 4.35**. The new signal was found at 52 ppm which indicated the three carbons linkage (-C-C-C-) from the MMA monomers to PMMA chains [276]. Then, the MEMO-PMMA-Br was sprayed on PMMA films and hydrolysed to change the methyl terminal groups to hydroxyl-end groups.
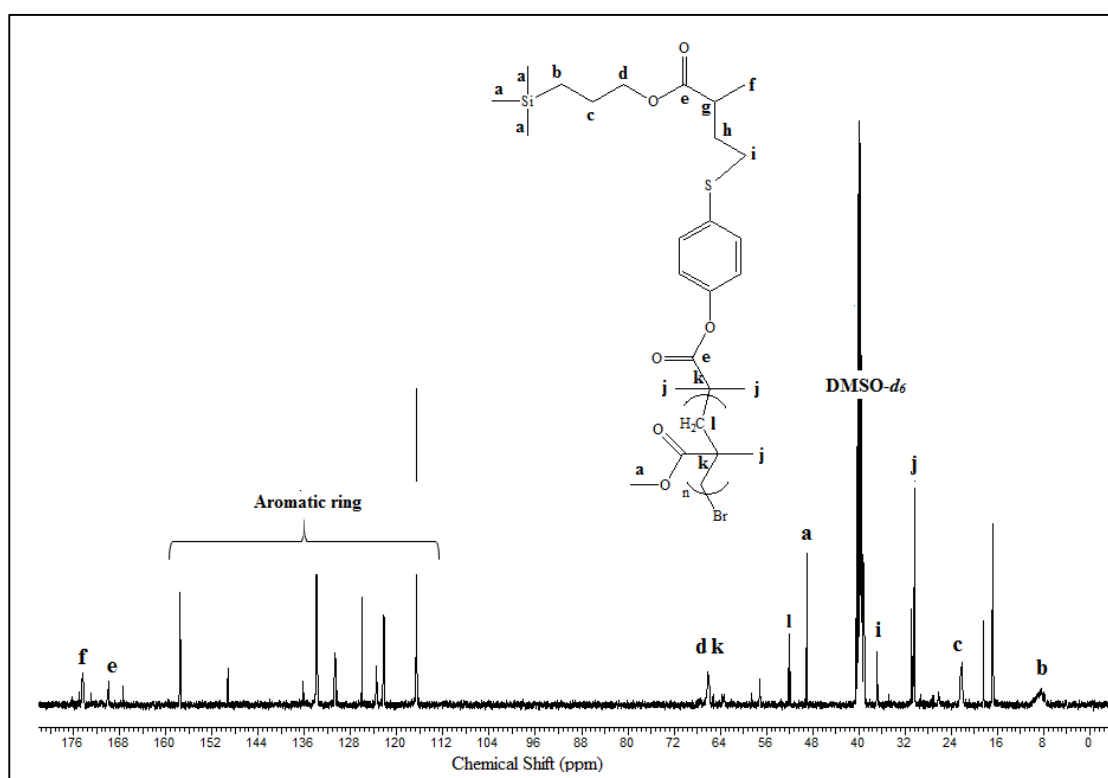
Figure 4.35 *^{13}C NMR signal spectra of MEMO-PMMA-Br*

The function on the surface of hydrolysed PMMA-g-MEMO-PMMA-Br was compared with blank PMMA film by FT-IR spectra in **Figure 4.36**. The hydrolysed PMMA films showed the presence of the reflectance of silicon hydroxyl group (-Si-OH), carbon double bonded with oxygen (-C=O-) and carbon-oxygen linkage (-C-O-) from ester at wavenumber 3360, 1713 and 1240 cm^{-1} [277-279], respectively. It implied that BIBB and MEMO were successfully linked and hydrolysed on the PMMA film.
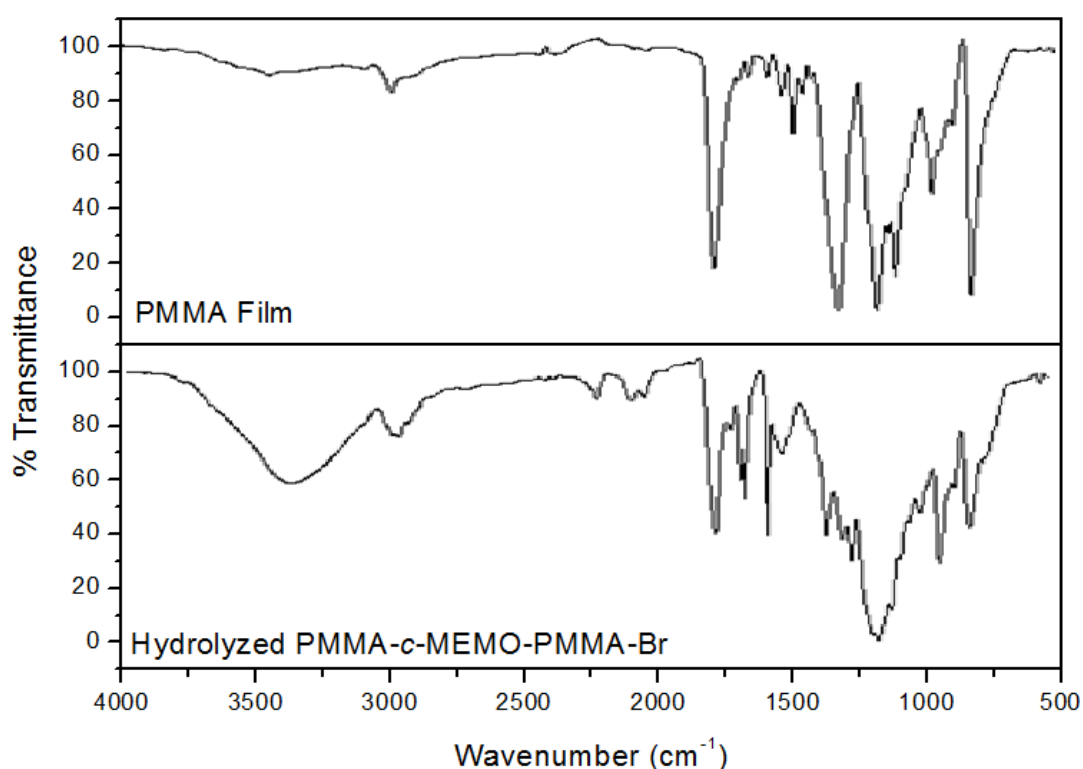
Figure 4.36 *FT-IR spectra of blank PMMA and hydrolysed of PMMA-g-MEMO-PMMA-Br*

The glass transition temperature of blank PMMA and PMMA-g-MEMO-PMMA-Br before hydrolysation was investigated by DSC signal. **Figure 4.37** shows the results of the glass transition temperature of blank PMMA at 563 K and PMMA-g-MEMO-PMMA-Br at 569 K. There is no significant change in glass transition temperature. It seems that the prepared liquid solution that was sprayed on the blank PMMA film did not change the properties of the PMMA film.
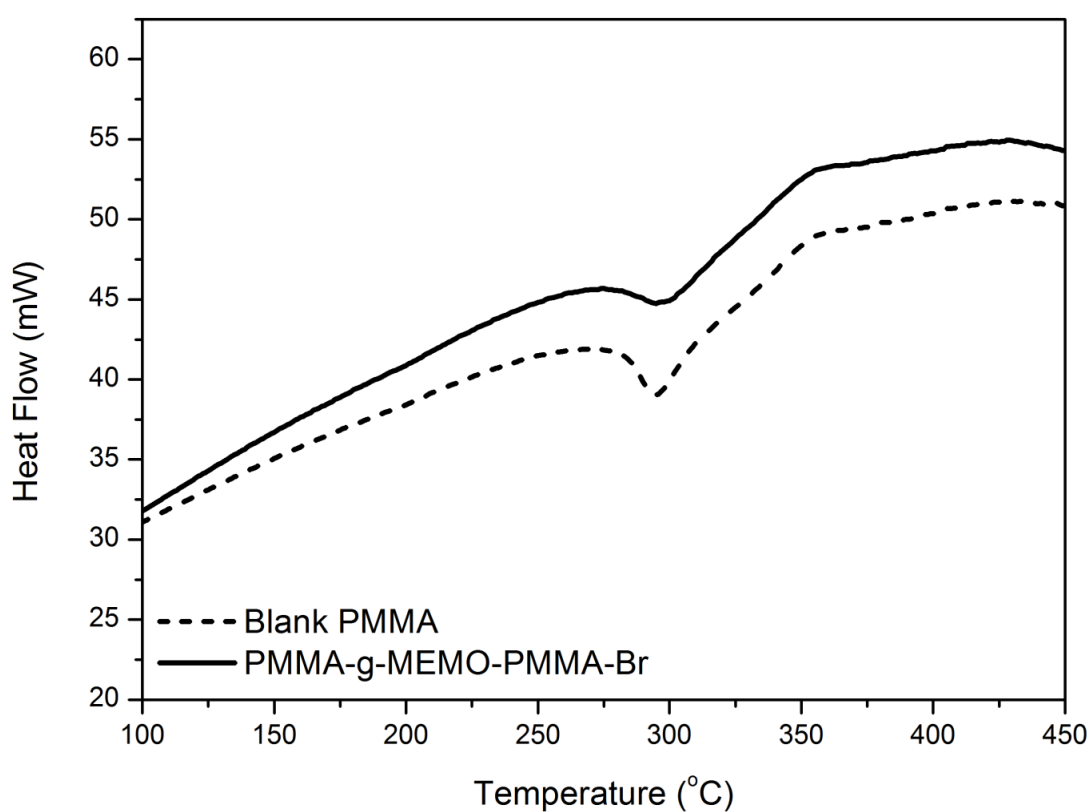
Figure 4.37 *DSC signals of blank PMMA and PMMA-g-MEMO-PMMA-Br before hydrolysed*

The surface composition of TiO_2-g-PMMA was identified by XPS spectra, as displayed in **Figure 4.38**. As a result, the XPS spectra of hydrolysed PMMA found the signal of Si *2p*, C *1s* and O *1s* at about 101, 285 and 530 eV [280-282], respectively. After the titanium dioxide catalyst powder was grafted onto the PMMA film, not only Si *2p* but also Ti *2p* were found at about 459 eV [283].
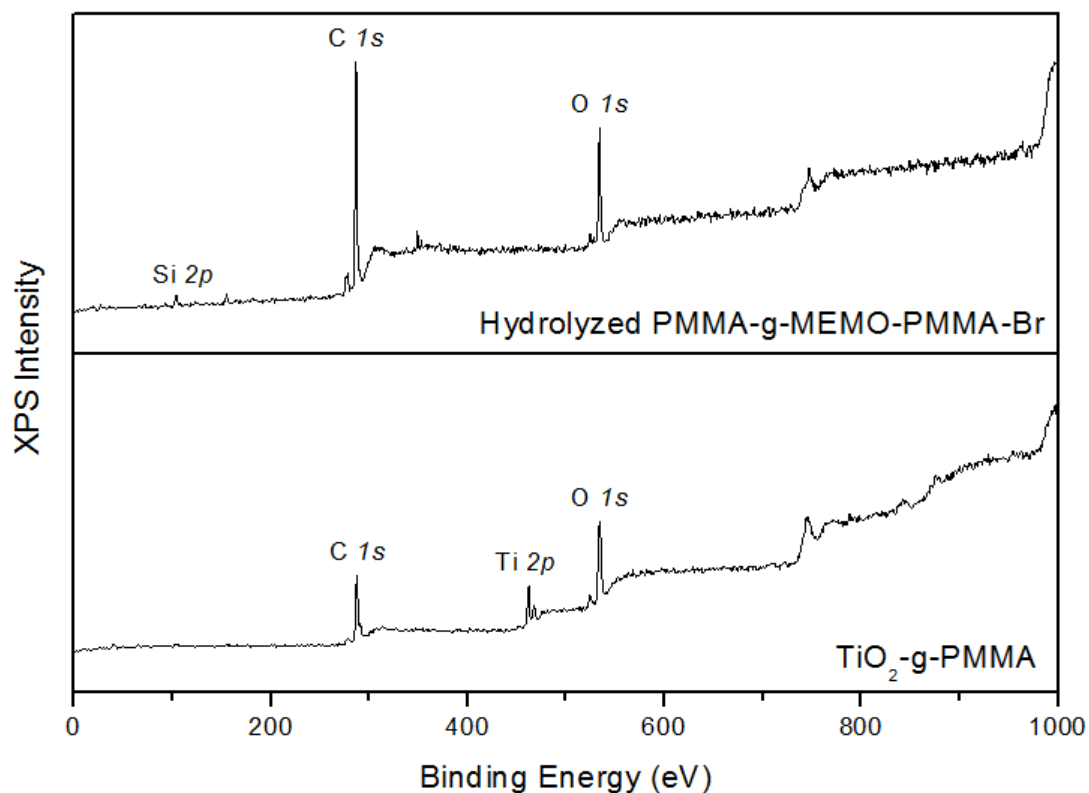
Figure 4.38 *XPS survey spectra of TiO_2-g-PMMA and hydrolysed PMMA-g-MEMO-PMMA-Br*

Figure **4.39** is the fine scan of Ti *2p* core level in XPS characterization. The peaks located at 457.5, 458.5, 463.0 and 464.3 eV are assigned to Ti^{3+} *2p*$_{3/2}$, Ti^{4+} *2p*$_{3/2}$, Ti^{3+} *2p*$_{1/2}$ and Ti^{4+} *2p*$_{1/2}$ [284-287], respectively, which are in excellent agreement with the XPS survey spectra.
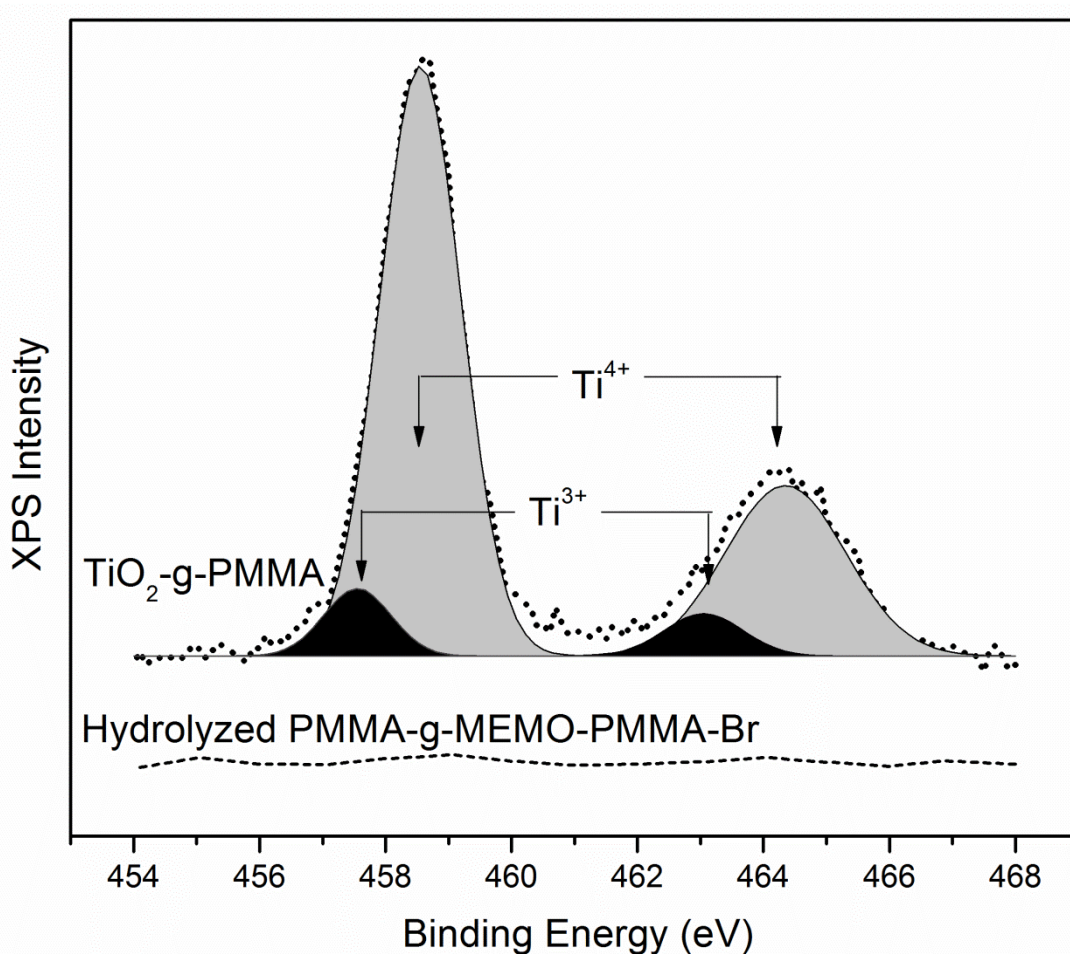
*Figure **4.39** Fine scan of Ti 2p core level in XPS characterization*

The attachment of titanium dioxide with MEMO caused the formation of the silica network via an ATRP route which uniformly distributed on the PMMA film [288, 289]. It is believed that the formation of the silica network mainly happens on the surface of titanium dioxide photocatalyst, because MEMO has already been grafted to

the surface of titanium dioxide photocatalyst. This process provide a porous structure on the surface through grafting [184].

Moreover, the successful grafting of titanium dioxide onto PMMA was also confirmed by the cross-sectional TEM observation. **Figure 4.40** is a representative image of TiO$_2$-g-PMMA that shows uniform spherical shaped morphology of titanium dioxide. This result will be correlated with the possible interaction between silicon and titanium dioxide on the PMMA film surface which was proposed in the **Figure 3.6**.
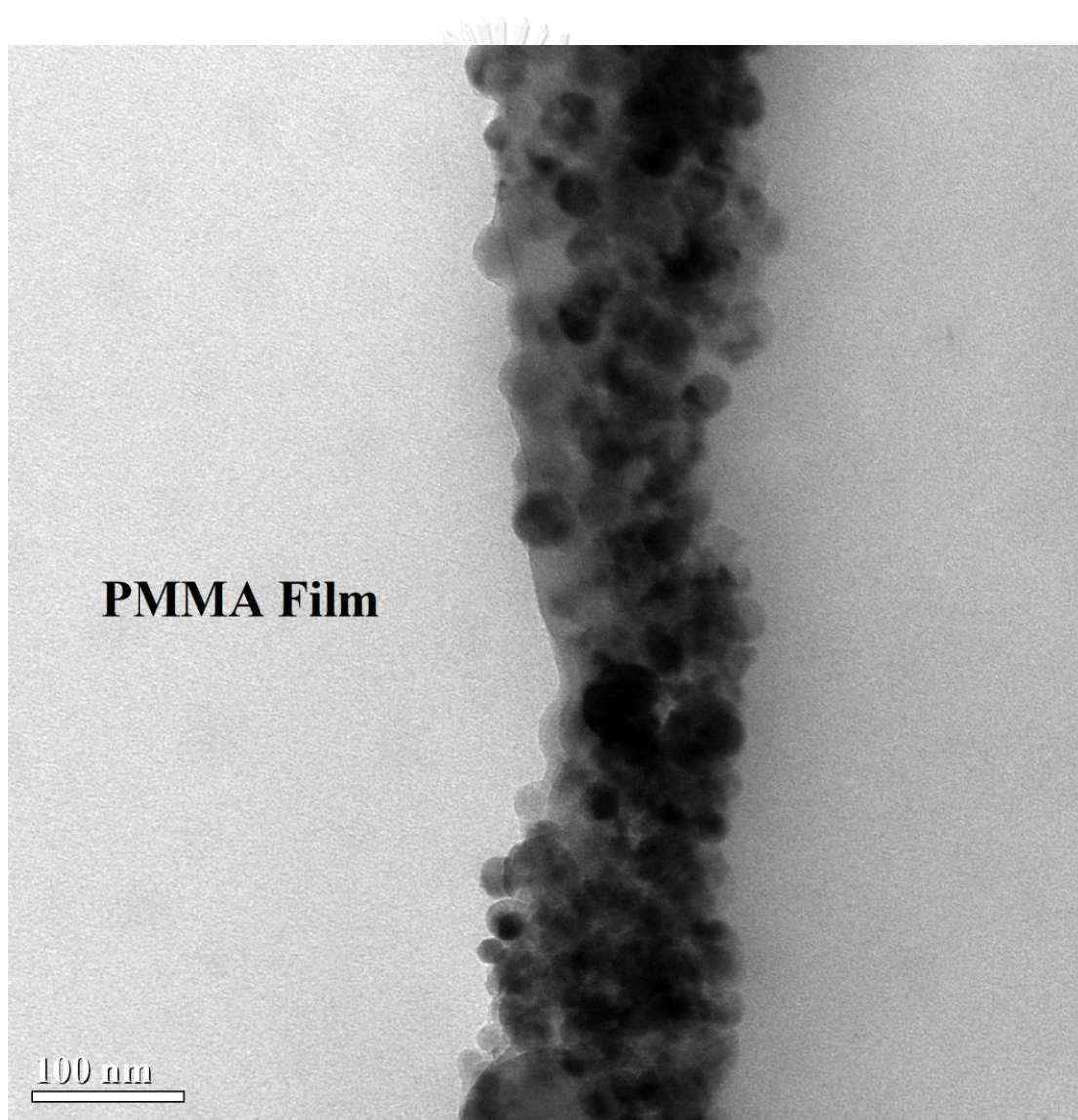
Figure 4.40 *Cross-sectional TEM observation of TiO$_2$-g-PMMA*

The bulk composition and morphology on TiO_2-g-PMMA was also characterised by SEM-EDX, shown in **Figure 4.41**(a. and b.) and **Table 4.18**. The SEM reveals the spherical titanium dioxide particles attached onto the PMMA film compared with blank PMMA. This result corresponds to the EDX composition, which found an absence of titanium atoms in the blank PMMA and did find the element on the TiO_2-g-PMMA.
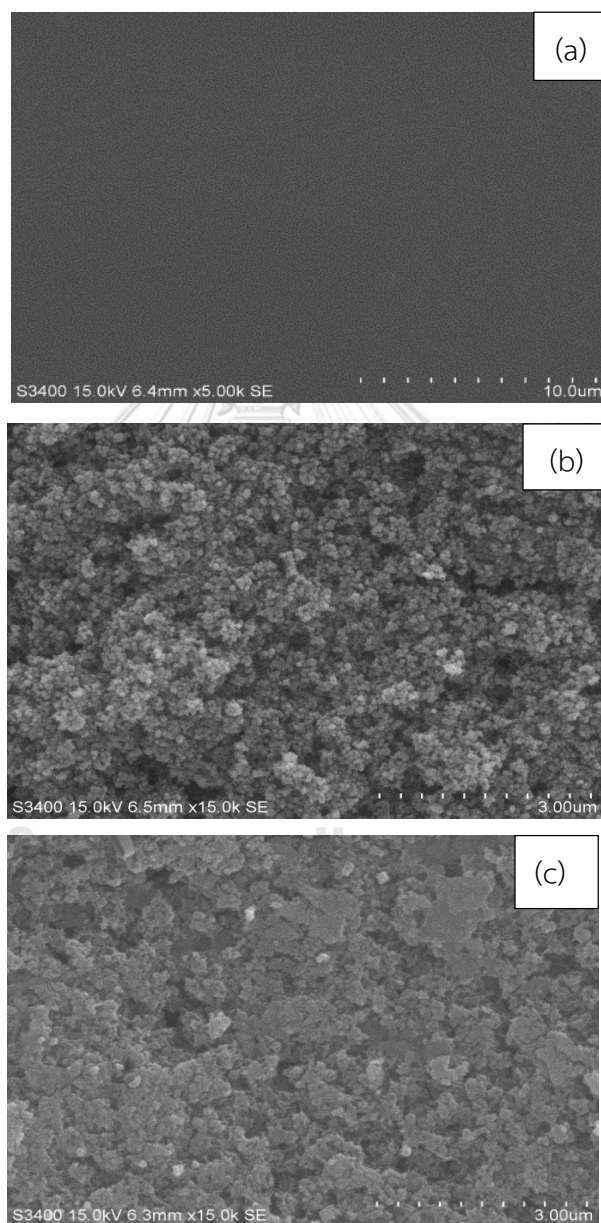
Figure 4.41 *SEM micrograph (a) blank PMMA (b) fresh TiO_2-g-PMMA and (c) used TiO_2-g-PMMA*

Table 4.18 The atomic composition of film by EDX analysis

Elements	Blank PMMA	TiO$_2$-g-PMMA Fresh	TiO$_2$-g-PMMA Used
C	85.46	7.20	8.30
O	13.02	57.06	59.57
Si	0.87	1.78	1.99
Ti	0.65	33.96	30.14

The photocatalytic performance and reusability of TiO$_2$-g-PMMA was investigated using the photodecolourisation of the methylene blue under UV light irradiation, as illustrated in **Figure 4.42**. Before the photocatalytic reaction, the film was immersed in methylene blue solution in the dark for 1 hour in order to remove the effect of the adsorption phenomena. The decolourisation of methylene blue of photolysis (no film) and blank PMMA is more likely not activated by UV light irradiation. For the reusability of TiO$_2$-g-PMMA film, the film was used in 5 cycles which showed nearly constant conversion.
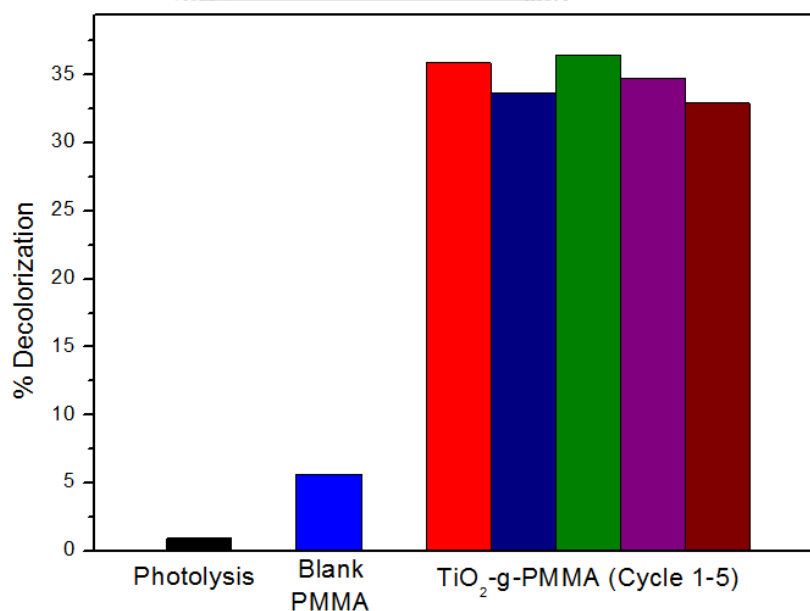
Figure 4.42 Photocatalytic activity of methylene blue decolourisation under UV light irradiation after 90 min

It can be concluded that titanium dioxide grafted onto the PMMA film is still active during photodecolourisation. **Figure 4.41**(c.) also shows the SEM micrograph of TiO_2-g-PMMA after the reaction test. It can be seen that the titanium dioxide particles were successfully grafted onto the PMMA film with this solution. Moreover, after the photocatalytic reaction the titanium dioxide particles did not leach from the PMMA film surface. **Table 4.18** shows the elemental components onto the PMMA film by EDX analysis. The EDX showed that the silicon and titanium elements were found in TiO_2-g-PMMA. The results revealed that there was no significant change in the titanium content deposited on the PMMA film. This was in good agreement with the reaction test. This indicates the high stability of titanium dioxide deposited onto the PMMA film.
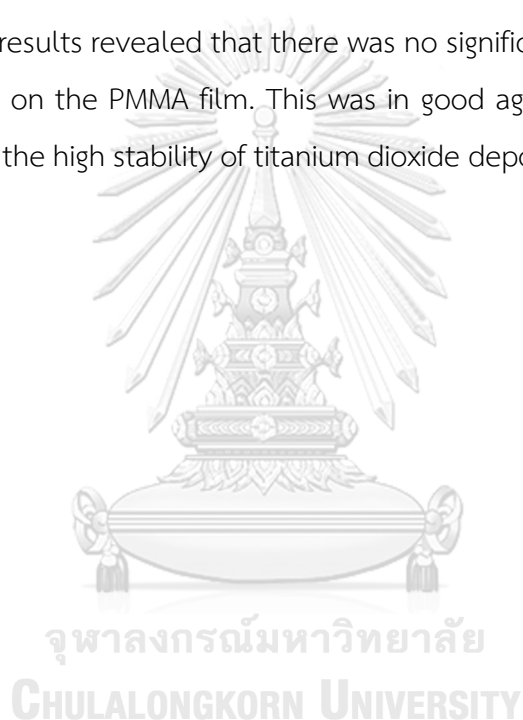
CHAPTER V

CONCLUSIONS AND RECOMMENDATIONS

5.1 Conclusions

The modification of titanium dioxide with nitrogen, silicon, and carbon were studied for visible light photocatalysis. It was found that, by reporting methods, the surface defect density (Ti^{3+}) on the catalyst surface could be increased by changing the calcination atmosphere from oxygen to air and to nitrogen, thus trapping photo-electrons and preventing the electron-hole recombination process. Moreover, the generation of the intermediate state within band gap resulted in the red shift of band gap moving to a visible region, which promoted the photocatalytic activity by decreasing in the indirect band gap. The doping with these elements increased the stability of the anatase phase which promoted the adsorption and degradation of methylene blue. All doping samples showed higher photoinduced wettability. The phenomenon was found to correlate with the presence of Ti^{3+} species.

5.2   Recommendations

1.   The loss of nitrogen during the photocatalysis should be further studied in the future work.

2.   The stability of APTES-modified titanium dioxide should be further studied.

3.   The reusability of carbon-doped titanium dioxide film should be tested.

4.   The leaching of titanium dioxide powder on polymer film should be further investigated.

REFERENCES

[1] A. Fujishima, K. Honda, Electrochemical Photolysis of Water at a Semiconductor Electrode, Nature, 238 (1972) 37-38.

[2] R. Molinari, M. Borgese, E. Drioli, L. Palmisano, M. Schiavello, Hybrid processes coupling photocatalysis and membranes for degradation of organic pollutants in water, Catalysis Today, 75 (2002) 77-85.

[3] L. Xiong, F. Yang, L. Yan, N. Yan, X. Yang, M. Qiu, Y. Yu, Bifunctional photocatalysis of TiO_2/Cu_2O composite under visible light: Ti3 in organic pollutant degradation and water splitting, Journal of Physics and Chemistry of Solids, 72 (2011) 1104-1109.

[4] S. Bekkouche, M. Bouhelassa, A.B. Aissa, S. Baup, N. Gondrexon, C. Pétrier, S. Merouani, O. Hamdaoui, Synergy between solar photocatalysis and high frequency sonolysis toward the degradation of organic pollutants in aqueous phase-scase of phenol, Desalination and Water Treatment, 62 (2017) 457-464.

[5] M. Matsuoka, M. Kitano, M. Takeuchi, K. Tsujimaru, M. Anpo, J.M. Thomas, Photocatalysis for new energy production. Recent advances in photocatalytic water splitting reactions for hydrogen production, Catalysis Today, 122 (2007) 51-61.

[6] W. Zhang, Y. Li, C. Wang, P. Wang, Q. Wang, Energy recovery during advanced wastewater treatment: Simultaneous estrogenic activity removal and hydrogen production through solar photocatalysis, Water Research, 47 (2013) 1480-1490.

[7] R. Michal, S. Sfaelou, P. Lianos, Photocatalysis for renewable energy production using photofuelcells, Molecules, 19 (2014) 19732-19750.

[8] M. Vohra, S. Selimuzzaman, M. Al‑Suwaiyan, NH_4^+‑NH_3 removal from simulated wastewater using UV‑TiO_2 photocatalysis: effect of co‑pollutants and pH, Environmental technology, 31 (2010) 641-654.

[9] O. Yayapao, T. Thongtem, A. Phuruangrat, S. Thongtem, Ultrasonic-assisted synthesis of Nd-doped ZnO for photocatalysis, Materials Letters, 90 (2013) 83-86.

[10] S. Wu, H. Cao, S. Yin, X. Liu, X. Zhang, Amino Acid-Assisted Hydrothermal Synthesis and Photocatalysis of SnO_2 Nanocrystals, The Journal of Physical Chemistry C, 113 (2009) 17893-17898.

[11] B. Li, B. Zhang, S. Nie, L. Shao, L. Hu, Optimization of plasmon-induced photocatalysis in electrospun Au/CeO_2 hybrid nanofibers for selective oxidation of benzyl alcohol, Journal of Catalysis, 348 (2017) 256-264.

[12] Z. Cinar, The Role of Molecular Modeling in TiO_2 Photocatalysis, Molecules, 22 (2017) 556.

[13] Y. Nosaka, A. Nosaka, Introduction to Photocatalysis: From Basic Science to Applications, Royal Society of Chemistry 2016.

[14] S.L. Suib, New and Future Developments in Catalysis: Solar Photocatalysis, Newnes 2013.

[15] X. Zhu, J. Zhou, Z. Cai, The toxicity and oxidative stress of TiO_2 nanoparticles in marine abalone (Haliotis diversicolor supertexta), Marine Pollution Bulletin, 63 (2011) 334-338.

[16] H. Yu, S. Zhang, H. Zhao, G. Will, P. Liu, An efficient and low-cost TiO_2 compact layer for performance improvement of dye-sensitized solar cells, Electrochimica Acta, 54 (2009) 1319-1324.

[17] L. Zhu, J. Zhang, Z. Chen, K. Liu, H. Gao, Effect of Cu_2O morphology on photocatalytic hydrogen generation and chemical stability of TiO_2/Cu_2O composite, Journal of Nanoscience and Nanotechnology, 13 (2013) 5104-5108.

[18] L.F. Lv, S.L. Lin, C.X. Chen, Preparation and anti-corrosion performance of conductive copolymer(aniline-co-pyrrole)/TiO_2 composite, Applied Mechanics and Materials, 2014, pp. 1210-1213.

[19] Y. Cai, Y.P. Feng, Review on charge transfer and chemical activity of TiO_2: Mechanism and applications, Progress in Surface Science, 91 (2016) 183-202.

[20] L. Lopez, W.A. Daoud, D. Dutta, B.C. Panther, T.W. Turney, Effect of substrate on surface morphology and photocatalysis of large-scale TiO_2 films, Applied Surface Science, 265 (2013) 162-168.

[21]   F. Li, T. Han, H. Wang, X. Zheng, J. Wan, B. Ni, Morphology evolution and visible light driven photocatalysis study of Ti^{3+} self-doped TiO_{2-x} nanocrystals, Journal of Materials Research, 32 (2017) 1563-1572.

[22]   J.J. Tang, X.J. Fan, Y. Zou, A.H. Deng, W. Zhang, K.G. Zhou, Effect of crystalline structure on TiO_2 photocatalysis under visible light irradiation, Beijing Keji Daxue Xuebao/Journal of University of Science and Technology Beijing, 31 (2009) 418-422.

[23]   L. Zhang, H. Liu, S. Lv, Q. Niu, Synthesis and photocatalysis of flaky flower TiO_2 with sphere structure, Journal of Sol-Gel Science and Technology, (2017) 1-7.

[24]   D.C. Luo, L.L. Zhang, H.J. Long, Y.M. Chen, Y.A. Cao, Effect of surface modification by Ni^{2+} on photocatalysis activity of TiO_2, Wuli Huaxue Xuebao/ Acta Physico - Chimica Sinica, 24 (2008) 1095-1099.

[25]   M. Farbod, M. Kajbafvala, Effect of nanoparticle surface modification on the adsorption-enhanced photocatalysis of Gd/TiO_2 nanocomposite, Powder Technology, 239 (2013) 434-440.

[26]   Y. Zhang, L. Fei, X. Jiang, C. Pan, Y. Wang, Engineering nanostructured Bi_2WO_6-TiO_2 toward effective utilization of natural light in photocatalysis, Journal of the American Ceramic Society, 94 (2011) 4157-4161.

[27]   G. Cheng, F. Xu, J. Xiong, F. Tian, J. Ding, F.J. Stadler, R. Chen, Enhanced adsorption and photocatalysis capability of generally synthesized TiO_2-carbon materials hybrids, Advanced Powder Technology, 27 (2016) 1949-1962.

[28]   X. Yang, C. Cao, L. Erickson, K. Hohn, R. Maghirang, K. Klabunde, Synthesis of visible-light-active TiO_2-based photocatalysts by carbon and nitrogen doping, Journal of Catalysis, 260 (2008) 128-133.

[29]   G. Yang, Z. Jiang, H. Shi, M.O. Jones, T. Xiao, P.P. Edwards, Z. Yan, Study on the photocatalysis of F-S co-doped TiO_2 prepared using solvothermal method, Applied Catalysis B: Environmental, 96 (2010) 458-465.

[30]   M. Crippa, E. Callone, M. D'Arienzo, K. Müller, S. Polizzi, L. Wahba, F. Morazzoni, R. Scotti, TiO_2 nanocrystals grafted on macroporous silica: A novel hybrid organic-inorganic sol-gel approach for the synthesis of highly photoactive composite material, Applied Catalysis B: Environmental, 104 (2011) 282-290.

[31]   H. Liu, F. Lian, L. Zhang, M. Liu, Photocatalysis property of titania-based thin films with covalent grafting PANi as sensitizer, Advanced Materials Research, 2012, pp. 470-473.

[32]   X.W. Liu, L.Y. Shen, Y.H. Hu, Preparation of TiO_2-Graphene Composite by a Two-Step Solvothermal Method and its Adsorption-Photocatalysis Property, Water, Air, and Soil Pollution, 227 (2016).

[33]   S. Khanchandani, S. Kumar, A.K. Ganguli, Comparative Study of TiO_2/CuS Core/Shell and Composite Nanostructures for Efficient Visible Light Photocatalysis, ACS Sustainable Chemistry and Engineering, 4 (2016) 1487-1499.

[34]   R. Asahi, T. Morikawa, T. Ohwaki, K. Aoki, Y. Taga, Visible-Light Photocatalysis in Nitrogen-Doped Titanium Oxides, Science, 293 (2001) 269.

[35]   J. Liu, Y. Zhou, F. Han, D. Chen, L. Chen, Synthesis of mesoporous Au-TiO_2 nanocomposites via a one-pot sol-gel process with enhanced photocatalytic activity, Materials Letters, 207 (2017) 109-112.

[36]   H. Liang, Z. Jia, H. Zhang, X. Wang, J. Wang, Photocatalysis oxidation activity regulation of Ag/TiO_2 composites evaluated by the selective oxidation of Rhodamine B, Applied Surface Science, 422 (2017) 1-10.

[37]   J. Araña, C. Fernández Rodríguez, O. González Díaz, J.A. Herrera Melián, J. Pérez Peña, Role of Cu in the Cu-TiO_2 photocatalytic degradation of dihydroxybenzenes, Catalysis Today, 101 (2005) 261-266.

[38]   H. Gao, J. Zhou, D. Dai, Y. Qu, Photocatalytic Activity and Electronic Structure Analysis of N‑doped Anatase TiO_2: A Combined Experimental and Theoretical Study, Chemical Engineering & Technology, 32 (2009) 867-872.

[39]   Y. Liu, J. He, Y. Sun, J. Hu, C. Li, G. Xue, S. Ognier, A comparison of N‑doped TiO_2 photocatalysts preparation methods and studies on their catalytic activity, Journal of Chemical Technology and Biotechnology, 88 (2013) 1815-1821.

[40]   Z. Bian, J. Zhu, H. Li, Solvothermal alcoholysis synthesis of hierarchical TiO_2 with enhanced activity in environmental and energy photocatalysis, Journal

of Photochemistry and Photobiology C: Photochemistry Reviews, 28 (2016) 72-86.

[41] D.G. Huang, S.J. Liao, J.M. Liu, Z. Dang, L. Petrik, Preparation of visible-light responsive N-F-codoped TiO_2 photocatalyst by a sol-gel-solvothermal method, Journal of Photochemistry and Photobiology A: Chemistry, 184 (2006) 282-288.

[42] J.S. Jang, H.G. Kim, U.A. Joshi, J.W. Jang, J.S. Lee, Fabrication of CdS nanowires decorated with TiO_2 nanoparticles for photocatalytic hydrogen production under visible light irradiation, International Journal of Hydrogen Energy, 33 (2008) 5975-5980.

[43] G. Tian, Y. Chen, W. Zhou, K. Pan, Y. Dong, C. Tian, H. Fu, Facile solvothermal synthesis of hierarchical flower-like Bi_2MoO_6 hollow spheres as high performance visible-light driven photocatalysts, Journal of Materials Chemistry, 21 (2011) 887-892.

[44] L. Wu, J.C. Yu, X. Fu, Characterization and photocatalytic mechanism of nanosized CdS coupled TiO_2 nanocrystals under visible light irradiation, Journal of Molecular Catalysis A: Chemical, 244 (2006) 25-32.

[45] C.R. Estrellan, C. Salim, H. Hinode, Photocatalytic activity of sol-gel derived TiO_2 co-doped with iron and niobium, Reaction Kinetics and Catalysis Letters, 98 (2009) 187-192.

[46] H. Lin, J. Li, C. Wang, Study on preparation of TiO_2 nanoparticle by sol-gel method, Advanced Materials Research, 2012, pp. 44-47.

[47] C. Anderson, A.J. Bard, Improved photocatalytic activity and characterization of mixed TiO_2/SiO_2 and TiO_2/Al_2O_3 materials, Journal of Physical Chemistry B, 101 (1997) 2611-2616.

[48] A.W. Xu, Y. Gao, H.Q. Liu, The preparation, characterization, and their photocatalytic activities of rare-earth-doped TiO_2 nanoparticles, Journal of Catalysis, 207 (2002) 151-157.

[49] J. Yu, X. Zhao, Q. Zhao, Effect of surface structure on photocatalytic activity of TiO_2 thin films prepared by sol-gel method, Thin Solid Films, 379 (2000) 7-14.

[50]   C. Junin, C. Thanachayanont, C. Euvananont, K. Inpor, P. Limthongkul, Effects of precipitation, sol-gel synthesis conditions, and drying methods on the properties of nano-TiO$_2$ for photocatalysis applications, European Journal of Inorganic Chemistry, (2008) 974-979.

[51]   S. Zhou, Y. Wu, J. Lv, L. Guo, D. Wang, G. Xu, Z. Zheng, Research on photocatalysis properties of nano TiO$_2$/mica composite material prepared by the method of hydrolysis-precipitation, Materials Science Forum, 2011, pp. 449-455.

[52]   G.R. Bamwenda, S. Tsubota, T. Nakamura, M. Haruta, Photoassisted hydrogen production from a water-ethanol solution: a comparison of activities of AuTiO2 and PtTiO$_2$, Journal of Photochemistry and Photobiology, A: Chemistry, 89 (1995) 177-189.

[53]   G.L. Chiarello, E. Selli, L. Forni, Photocatalytic hydrogen production over flame spray pyrolysis-synthesised TiO$_2$ and Au/TiO$_2$, Applied Catalysis B: Environmental, 84 (2008) 332-339.

[54]   O. Arutanti, A.B.D. Nandiyanto, T. Ogi, F. Iskandar, T.O. Kim, K. Okuyama, Synthesis of composite WO$_3$/TiO$_2$ nanoparticles by flame-assisted spray pyrolysis and their photocatalytic activity, Journal of Alloys and Compounds, 591 (2014) 121-126.

[55]   W.Y. Teoh, L. Mädler, D. Beydoun, S.E. Pratsinis, R. Amal, Direct (one-step) synthesis of TiO$_2$ and Pt/TiO$_2$ nanoparticles for photocatalytic mineralisation of sucrose, Chemical Engineering Science, 60 (2005) 5852-5861.

[56]   H. Kominami, J.I. Kalo, Y. Takada, Y. Doushi, B. Ohtani, S.I. Nishimoto, M. Inoue, T. Inui, Y. Kera, Novel synthesis of microcrystalline titanium(IV) oxide having high thermal stability and ultra-high photocatalytic activity: Thermal decomposition of titanium(IV) alkoxide in organic solvents, Catalysis Letters, 46 (1997) 235-240.

[57]   J. Zhang, X. Hou, Z. Pang, Y. Cai, H. Zhou, P. Lv, Q. Wei, Fabrication of hierarchical TiO$_2$ nanofibers by microemulsion electrospinning for photocatalysis applications, Ceramics International, 43 (2017) 15911-15917.

[58]   F. Kayaci, S. Vempati, C. Ozgit-Akgun, I. Donmez, N. Biyikli, T. Uyar, Selective isolation of the electron or hole in photocatalysis: ZnO-TiO$_2$ and TiO$_2$-ZnO core-shell structured heterojunction nanofibers via electrospinning and atomic layer deposition, Nanoscale, 6 (2014) 5735-5745.

[59]   N. Chadwick, S. Sathasivam, A. Kafizas, S.M. Bawaked, A.Y. Obaid, S. Al-Thabaiti, S.N. Basahel, I.P. Parkin, C.J. Carmalt, Combinatorial aerosol assisted chemical vapour deposition of a photocatalytic mixed SnO$_2$/TiO$_2$ thin film, Journal of Materials Chemistry A, 2 (2014) 5108-5116.

[60]   L. Ma, A. Chen, J. Lu, Z. Zhang, H. He, C. Li, In situ synthesis of CNTs/Fe-Ni/TiO$_2$ nanocomposite by fluidized bed chemical vapor deposition and the synergistic effect in photocatalysis, Particuology, 14 (2014) 24-32.

[61]   H. Lin, C.P. Huang, W. Li, C. Ni, S.I. Shah, Y.H. Tseng, Size dependency of nanocrystalline TiO$_2$ on its optical property and photocatalytic reactivity exemplified by 2-chlorophenol, Applied Catalysis B: Environmental, 68 (2006) 1-11.

[62]   H. Fakhouri, J. Pulpytel, W. Smith, A. Zolfaghari, H.R. Mortaheb, F. Meshkini, R. Jafari, E. Sutter, F. Arefi-Khonsari, Control of the visible and UV light water splitting and photocatalysis of nitrogen doped TiO$_2$ thin films deposited by reactive magnetron sputtering, Applied Catalysis B: Environmental, 144 (2014) 12-21.

[63]   Z.A. Lin, W.C. Lu, C.Y. Wu, K.S. Chang, Facile fabrication and tuning of TiO$_2$ nanoarchitectured morphology using magnetron sputtering and its applications to photocatalysis, Ceramics International, 40 (2014) 15523-15529.

[64]   B. Thiébaut, Final Analysis: Flame Spray Pyrolysis: A Unique Facility for the Production of Nanopowders, Platinum Metals Review, 55 (2011) 149-151.

[65]   W. Teoh, A Perspective on the Flame Spray Synthesis of Photocatalyst Nanoparticles, Materials, 6 (2013) 3194-3212.

[66]   J. Zhao, Y. Gu, J. Huang, Flame synthesis of hierarchical nanotubular rutile titania derived from natural cellulose substance, Chemical Communications, 47 (2011) 10551-10553.

[67]   W. Kongsuebchart, P. Praserthdam, J. Panpranot, A. Sirisuk, P. Supphasrirongjaroen, C. Satayaprasert, Effect of crystallite size on the surface defect of nano-TiO$_2$ prepared via solvothermal synthesis, Journal of Crystal Growth, 297 (2006) 234-238.

[68]   M. Danish, S. Ambreen, A. Chauhan, A. Pandey, Optimization and comparative evaluation of optical and photocatalytic properties of TiO$_2$ thin films prepared via sol–gel method, Journal of Saudi Chemical Society, 19 (2015) 557-562.

[69]   P. Kajitvichyanukul, J. Ananpattarachai, S. Pongpom, Sol–gel preparation and properties study of TiO$_2$ thin film for photocatalytic reduction of chromium(VI) in photocatalysis process, Science and Technology of Advanced Materials, 6 (2005) 352-358.

[70]   X. Chen, S.S. Mao, Titanium Dioxide Nanomaterials: Synthesis, Properties, Modifications, and Applications, Chemical Reviews, 107 (2007) 2891-2959.

[71]   Y. Gu, X. Liu, T. Niu, J. Huang, Titania nanotube/hollow sphere hybrid material: Dual-template synthesis and photocatalytic property, Materials Research Bulletin, 45 (2010) 536-541.

[72]   M. Anpo, M. Takeuchi, The design and development of highly reactive titanium oxide photocatalysts operating under visible light irradiation, Journal of Catalysis, 216 (2003) 505-516.

[73]   J.C. Yu, J. Lin, R.W.M. Kwok, Ti$_{1-x}$Zr$_x$O$_2$ solid solutions for the photocatalytic degradation of acetone in air, Journal of Physical Chemistry B, 102 (1998) 5094-5098.

[74]   Y. Tae Kwon, K. Yong Song, W. In Lee, G. Jin Choi, Y. Rag Do, Photocatalytic behavior of WO$_3$-loaded TiO$_2$ in an oxidation reaction, Journal of Catalysis, 191 (2000) 192-199.

[75]   F.B. Li, X.Z. Li, M.F. Hou, K.W. Cheah, W.C.H. Choy, Enhanced photocatalytic activity of Ce^{3+}-TiO^2 for 2-mercaptobenzothiazole degradation in aqueous suspension for odour control, Applied Catalysis A: General, 285 (2005) 181-189.

[76]   X. Yu, J. Yu, B. Cheng, M. Jaroniec, Synthesis of hierarchical flower-like AlOOH and TiO$_2$/AlOOH superstructures and their enhanced photocatalytic properties, Journal of Physical Chemistry C, 113 (2009) 17527-17535.

[77]   P. Cheng, M. Zheng, Y. Jin, Q. Huang, M. Gu, Preparation and characterization of silica-doped titania photocatalyst through sol-gel method, Materials Letters, 57 (2003) 2989-2994.

[78]   N. Bao, Z. Wei, Z. Ma, F. Liu, G. Yin, Si-doped mesoporous TiO$_2$ continuous fibers: Preparation by centrifugal spinning and photocatalytic properties, Journal of Hazardous Materials, 174 (2010) 129-136.

[79]   J.G. Liu, C.W. Yan, Electrochemical characteristics of corrosion behavior of organic/Dacromet composite systems pretreated with gamma-aminopropyltriethoxysilane, Surface and Coatings Technology, 200 (2006) 4976-4986.

[80]   M. Wiśniewska, S. Chibowski, T. Urban, Modification of the alumina surface properties by adsorbed anionic polyacrylamide—Impact of polymer hydrolysis, Journal of Industrial and Engineering Chemistry, 21 (2015) 925-931.

[81]   J. Kim, P. Seidler, L.S. Wan, C. Fill, Formation, structure, and reactivity of amino-terminated organic films on silicon substrates, Journal of Colloid and Interface Science, 329 (2009) 114-119.

[82]   G.H. Mirzabe, A.R. Keshtkar, Application of response surface methodology for thorium adsorption on PVA/Fe$_3$O$_4$/SiO$_2$/APTES nanohybrid adsorbent, Journal of Industrial and Engineering Chemistry, 26 (2015) 277-285.

[83]   K. Abou-El-Sherbini, C. Pape, O. Rienetz, D. Schiel, R. Stosch, P. Weidler, W. Höll, Stabilization of n-aminopropyl silica gel against hydrolysis by blocking silanol groups with TiO$_2$ or ZrO$_2$, Journal of Sol-Gel Science and Technology, 53 (2010) 587-597.

[84]   A. Xue, S. Zhou, Y. Zhao, X. Lu, P. Han, Effective NH2-grafting on attapulgite surfaces for adsorption of reactive dyes, Journal of Hazardous Materials, 194 (2011) 7-14.

[85]   N. Bao, G. Wu, J. Niu, Q. Zhang, S. He, J. Wang, Wide spectral response and enhanced photocatalytic activity of TiO$_2$ continuous fibers modified with

aminosilane coupling agents, Journal of Alloys and Compounds, 599 (2014) 40-48.

[86]   R. Klaysri, S. Wichaidit, T. Tubchareon, S. Nokjan, S. Piticharoenphun, O. Mekasuwandumrong, P. Praserthdam, Impact of calcination atmospheres on the physiochemical and photocatalytic properties of nanocrystalline TiO_2 and Si-doped TiO_2, Ceramics International, 41 (2015) 11409-11417.

[87]   G. Yang, Z. Jiang, H. Shi, T. Xiao, Z. Yan, Preparation of highly visible-light active N-doped TiO_2 photocatalyst, Journal of Materials Chemistry, 20 (2010) 5301-5309.

[88]   N. Comsup, J. Panpranot, P. Praserthdam, The influence of Si-modified TiO_2 on the activity of Ag/TiO_2 in CO oxidation, Journal of Industrial and Engineering Chemistry, 16 (2010) 703-707.

[89]   F. Cheng, S.M. Sajedin, S.M. Kelly, A.F. Lee, A. Kornherr, UV-stable paper coated with APTES-modified P25 TiO_2 nanoparticles, Carbohydrate Polymers, 114 (2014) 246-252.

[90]   M. Ratova, P.J. Kelly, G.T. West, I. Iordanova, Enhanced properties of magnetron sputtered photocatalytic coatings via transition metal doping, Surface and Coatings Technology, 228, Supplement 1 (2013) S544-S549.

[91]   N.T. Nolan, D.W. Synnott, M.K. Seery, S.J. Hinder, A. Van Wassenhoven, S.C. Pillai, Effect of N-doping on the photocatalytic activity of sol-gel TiO_2, Journal of Hazardous Materials, 211-212 (2012) 88-94.

[92]   M.S. Wong, H.P. Chou, T.S. Yang, Reactively sputtered N-doped titanium oxide films as visible-light photocatalyst, Thin Solid Films, 494 (2006) 244-249.

[93]   M.C. Wang, H.J. Lin, C.H. Wang, H.C. Wu, Effects of annealing temperature on the photocatalytic activity of N-doped TiO_2 thin films, Ceramics International, 38 (2012) 195-200.

[94]   G. Abadias, F. Paumier, D. Eyidi, P. Guerin, T. Girardeau, Structure and properties of nitrogen-doped titanium dioxide thin films produced by reactive magnetron sputtering, Surface and Interface Analysis, 42 (2010) 970-973.

[95]   X. Bu, G. Zhang, C. Zhang, Effect of nitrogen doping on anatase–rutile phase transformation of TiO_2, Applied Surface Science.

[96]   F. Peng, L. Cai, H. Yu, H. Wang, J. Yang, Synthesis and characterization of substitutional and interstitial nitrogen-doped titanium dioxides with visible light photocatalytic activity, Journal of Solid State Chemistry, 181 (2008) 130-136.

[97]   Y. Xie, X. Zhao, Y. Chen, Q. Zhao, Q. Yuan, Preparation and characterization of porous C-modified anatase titania films with visible light catalytic activity, Journal of Solid State Chemistry, 180 (2007) 3576-3582.

[98]   T. Ohno, M. Akiyoshi, T. Umebayashi, K. Asai, T. Mitsui, M. Matsumura, Preparation of S-doped TiO_2 photocatalysts and their photocatalytic activities under visible light, Applied Catalysis A: General, 265 (2004) 115-121.

[99]   E.M. Rockafellow, L.K. Stewart, W.S. Jenks, Is sulfur-doped TiO_2 an effective visible light photocatalyst for remediation?, Applied Catalysis B: Environmental, 91 (2009) 554-562.

[100]   V. Gombac, L. De Rogatis, A. Gasparotto, G. Vicario, T. Montini, D. Barreca, G. Balducci, P. Fornasiero, E. Tondello, M. Graziani, TiO_2 nanopowders doped with boron and nitrogen for photocatalytic applications, Chemical Physics, 339 (2007) 111-123.

[101]   M.V. Dozzi, C. D'Andrea, B. Ohtani, G. Valentini, E. Selli, Fluorine-Doped TiO_2 Materials: Photocatalytic Activity vs Time-Resolved Photoluminescence, The Journal of Physical Chemistry C, 117 (2013) 25586-25595.

[102]   Y. Ao, J. Xu, D. Fu, C. Yuan, Synthesis of C,N,S-tridoped mesoporous titania with enhanced visible light-induced photocatalytic activity, Microporous and Mesoporous Materials, 122 (2009) 1-6.

[103]   K.R. Wu, C.H. Hung, Characterization of N,C-codoped TiO_2 films prepared by reactive DC magnetron sputtering, Applied Surface Science, 256 (2009) 1595-1603.

[104]   M.V. Dozzi, E. Selli, Doping TiO_2 with p-block elements: Effects on photocatalytic activity, Journal of Photochemistry and Photobiology C: Photochemistry Reviews, 14 (2013) 13-28.

[105]   N. Serpone, Is the Band Gap of Pristine TiO_2 Narrowed by Anion- and Cation-Doping of Titanium Dioxide in Second-Generation Photocatalysts?, The Journal of Physical Chemistry B, 110 (2006) 24287-24293.

[106]   J.A. Sullivan, E.M. Neville, R. Herron, K.R. Thampi, J.M.D. MacElroy, Routes to visible light active C-doped TiO_2 photocatalysts using carbon atoms from the Ti precursors, Journal of Photochemistry and Photobiology A: Chemistry, 289 (2014) 60-65.

[107]   Y. Zhang, Z. Zhao, J. Chen, L. Cheng, J. Chang, W. Sheng, C. Hu, S. Cao, C-doped hollow TiO_2 spheres: in situ synthesis, controlled shell thickness, and superior visible-light photocatalytic activity, Applied Catalysis B: Environmental, 165 (2015) 715-722.

[108]   J. Wang, Z. Wang, H. Li, Y. Cui, Y. Du, Visible light-driven nitrogen doped TiO_2 nanoarray films: Preparation and photocatalytic activity, Journal of Alloys and Compounds, 494 (2010) 372-377.

[109]   P.J. Kelly, G.T. West, M. Ratova, L. Fisher, S. Ostovarpour, J. Verran, Structural Formation and Photocatalytic Activity of Magnetron Sputtered Titania and Doped-Titania Coatings, Molecules, 19 (2014) 16327-16348.

[110]   P.J. Kelly, R.D. Arnell, Development of a novel structure zone model relating to the closed-field unbalanced magnetron sputtering system, Journal of Vacuum Science & Technology A: Vacuum, Surfaces, and Films, 16 (1998) 2858-2869.

[111]   H. Irie, S. Washizuka, K. Hashimoto, Hydrophilicity on carbon-doped TiO_2 thin films under visible light, Thin Solid Films, 510 (2006) 21-25.

[112]   S.S. Pradhan, S. Sahoo, S.K. Pradhan, Influence of annealing temperature on the structural, mechanical and wetting property of TiO_2 films deposited by RF magnetron sputtering, Thin Solid Films, 518 (2010) 6904-6908.

[113]   D. Kibanova, J. Cervini-Silva, H. Destaillats, Efficiency of clay - TiO_2 nanocomposites on the photocatalytic elimination of a model hydrophobic air pollutant, Environmental Science and Technology, 43 (2009) 1500-1506.

[114] C.C. Wang, C.K. Lee, M.D. Lyu, L.C. Juang, Photocatalytic degradation of C.I. Basic Violet 10 using TiO$_2$ catalysts supported by Y zeolite: An investigation of the effects of operational parameters, Dyes and Pigments, 76 (2008) 817-824.

[115] X. Zhang, M. Zhou, L. Lei, Preparation of photocatalytic TiO$_2$ coatings of nanosized particles on activated carbon by AP-MOCVD, Carbon, 43 (2005) 1700-1708.

[116] A. Dutschke, C. Diegelmann, P. Lobmann, Preparation of TiO$_2$ thin films on polystyrene by liquid phase deposition, Journal of Materials Chemistry, 13 (2003) 1058-1063.

[117] M.N. Tchoul, S.P. Fillery, H. Koerner, L.F. Drummy, F.T. Oyerokun, P.A. Mirau, M.F. Durstock, R.A. Vaia, Assemblies of Titanium Dioxide-Polystyrene Hybrid Nanoparticles for Dielectric Applications, Chemistry of Materials, 22 (2010) 1749-1759.

[118] C. Ye, H. Li, A. Cai, Q. Gao, X. Zeng, Preparation and Characterization of Organic Nano-Titanium Dioxide/Acrylate Composite Emulsions by in-situ Emulsion Polymerization, Journal of Macromolecular Science, Part A, 48 (2011) 309-314.

[119] A. Mesnage, M. Abdel Magied, P. Simon, N. Herlin-Boime, P. Jégou, G. Deniau, S. Palacin, Grafting polymers to titania nanoparticles by radical polymerization initiated by diazonium salt, Journal of Materials Science, 46 (2011) 6332-6338.

[120] S. Lu, S.-S. Sun, J. Niu, L. Zeng, H. Liu, X. Zhao, Poly (thienylene methine) grafted nanocrystalline TiO$_2$ based hybrid solar cells, J Mater Sci: Mater Electron, 23 (2012) 251-256.

[121] A.A. Essawy, A.E.-H. Ali, M. Abdel-Mottaleb, Application of novel copolymer-TiO$_2$ membranes for some textile dyes adsorptive removal from aqueous solution and photocatalytic decolorization, Journal of hazardous materials, 157 (2008) 547-552.

[122] L. Liu, H. Chen, F. Yang, Enhancing membrane performance by blending ATRP grafted PMMA–TiO2 or PMMA–PSBMA–TiO$_2$ in PVDF, Separation and Purification Technology, 133 (2014) 22-31.

[123]   G. Zhang, S. Lu, L. Zhang, Q. Meng, C. Shen, J. Zhang, Novel polysulfone hybrid ultrafiltration membrane prepared with TiO_2-g-HEMA and its antifouling characteristics, Journal of Membrane Science, 436 (2013) 163-173.

[124]   D.A. Savin, J. Pyun, G.D. Patterson, T. Kowalewski, K. Matyjaszewski, Synthesis and characterization of silica-graft-polystyrene hybrid nanoparticles: Effect of constraint on the glass-transition temperature of spherical polymer brushes, Journal of Polymer Science, Part B: Polymer Physics, 40 (2002) 2667-2676.

[125]   L. Bai, L. Zhang, Z. Zhang, J. Zhu, N. Zhou, Z. Cheng, X. Zhu, Alumina additives for fast iron-mediated AGET ATRP of MMA using onium salt as ligand, Journal of Polymer Science, Part A: Polymer Chemistry, 49 (2011) 3970-3979.

[126]   Y. Wang, X. Teng, J.S. Wang, H. Yang, Solvent-free atom transfer radical polymerization in the synthesis of Fe_2O_3@polystyrene core-shell nanoparticles, Nano Letters, 3 (2003) 789-793.

[127]   P. Liu, T. Wang, Poly(hydroethyl acrylate) grafted from ZnO nanoparticles via surface-initiated atom transfer radical polymerization, Current Applied Physics, 8 (2008) 66-70.

[128]   B. Graß, A. Neyer, M. Jöhnck, D. Siepe, F. Eisenbeiß, G. Weber, R. Hergenröder, A new PMMA-microchip device for isotachophoresis with integrated conductivity detector, Sensors and Actuators B: Chemical, 72 (2001) 249-258.

[129]   J.-Y. Cheng, C.-W. Wei, K.-H. Hsu, T.-H. Young, Direct-write laser micromachining and universal surface modification of PMMA for device development, Sensors and Actuators B: Chemical, 99 (2004) 186-196.

[130]   D.A.H. Hanaor, C.C. Sorrell, Review of the anatase to rutile phase transformation, Journal of Materials Science, 46 (2011) 855-874.

[131]   J. Arbiol, J. Cerdà, G. Dezanneau, A. Cirera, F. Peiró, A. Cornet, J.R. Morante, Effects of Nb doping on the TiO_2 anatase-to-rutile phase transition, Journal of Applied Physics, 92 (2002) 853-861.

[132]   K. Okada, N. Yamamoto, Y. Kameshima, A. Yasumori, K.J.D. MacKenzie, Effect of Silica Additive on the Anatase-to-Rutile Phase Transition, Journal of the American Ceramic Society, 84 (2001) 1591-1596.

[133]   D.-J. Won, C.-H. Wang, H.-K. Jang, D.-J. Choi, Effects of thermally induced anatase-to-rutile phase transition in MOCVD-grown TiO_2 films on structural and optical properties, Applied Physics A, 73 (2001) 595-600.

[134]   R. Arroyo, G. Córdoba, J. Padilla, V.H. Lara, Influence of manganese ions on the anatase–rutile phase transition of TiO_2 prepared by the sol–gel process, Materials Letters, 54 (2002) 397-402.

[135]   L.E. Oi, M.-Y. Choo, H.V. Lee, H.C. Ong, S.B.A. Hamid, J.C. Juan, Recent advances of titanium dioxide (TiO2) for green organic synthesis, RSC Advances, 6 (2016) 108741-108754.

[136]   D. Bamba, M. Coulibaly, D. Robert, Nitrogen-containing organic compounds: Origins, toxicity and conditions of their photocatalytic mineralization over TiO_2, Science of The Total Environment, 580 (2017) 1489-1504.

[137]   A. Ramos-Delgado Norma, Á. Gracia-Pinilla Miguel, V. Mangalaraja Ramalinga, K. O'Shea, D. Dionysiou Dionysios, Industrial synthesis and characterization of nanophotocatalysts materials: titania, Nanotechnology Reviews, 2016, pp. 467.

[138]   N. Pinna, M. Niederberger, Surfactant-Free Nonaqueous Synthesis of Metal Oxide Nanostructures, Angewandte Chemie International Edition, 47 (2008) 5292-5304.

[139]   T. Kasuga, M. Hiramatsu, A. Hoson, T. Sekino, K. Niihara, Formation of Titanium Oxide Nanotube, Langmuir, 14 (1998) 3160-3163.

[140]   D.L. Morgan, H.-Y. Zhu, R.L. Frost, E.R. Waclawik, Determination of a Morphological Phase Diagram of Titania/Titanate Nanostructures from Alkaline Hydrothermal Treatment of Degussa P25, Chemistry of Materials, 20 (2008) 3800-3802.

[141]   X. Peng, A. Chen, Large-Scale Synthesis and Characterization of TiO_2-Based Nanostructures on Ti Substrates, Advanced Functional Materials, 16 (2006) 1355-1362.

[142]   Z.G. Li, S. Miyake, Characteristics of N-doped TiO_2 thin films grown on unheated glass substrate by inductively coupled plasma assisted dc reactive magnetron sputtering, Applied Surface Science, 255 (2009) 9149-9153.

[143]   S. Peng, Y. Yang, G. Li, J. Jiang, K. Jin, T. Yao, K. Zhang, X. Cao, Y. Wang, G. Xu, Effect of N_2 flow rate on the properties of N doped TiO_2 films deposited by DC coupled RF magnetron sputtering, Journal of Alloys and Compounds, 678 (2016) 355-359.

[144]   M. Anpo, M. Takeuchi, The design and development of highly reactive titanium oxide photocatalysts operating under visible light irradiation, Journal of Catalysis, 216 (2003) 505-516.

[145]   C. Di Valentin, G. Pacchioni, A. Selloni, Origin of the different photoactivity of N-doped anatase and rutile TiO_2, Physical Review B, 70 (2004) 085116.

[146]   S.A. Ansari, M.M. Khan, M.O. Ansari, M.H. Cho, Nitrogen-doped titanium dioxide (N-doped TiO_2) for visible light photocatalysis, New Journal of Chemistry, 40 (2016) 3000-3009.

[147]   R. Asahi, T. Morikawa, T. Ohwaki, K. Aoki, Y. Taga, Visible-light photocatalysis in nitrogen-doped titanium oxides, science, 293 (2001) 269-271.

[148]   C.W. Dunnill, I.P. Parkin, Nitrogen-doped TiO_2 thin films: photocatalytic applications for healthcare environments, Dalton Transactions, 40 (2011) 1635-1640.

[149]   C. Chen, H. Bai, C. Chang, Effect of Plasma Processing Gas Composition on the Nitrogen-Doping Status and Visible Light Photocatalysis of TiO_2, The Journal of Physical Chemistry C, 111 (2007) 15228-15235.

[150]   M. Hu, M. Fang, C. Tang, T. Yang, Z. Huang, Y. Liu, X. Wu, X. Min, The effects of atmosphere and calcined temperature on photocatalytic activity of TiO_2 nanofibers prepared by electrospinning, Nanoscale Research Letters, 8 (2013) 548.

[151]   M. Dawson, G.B. Soares, C. Ribeiro, Influence of calcination parameters on the synthesis of N-doped TiO_2 by the polymeric precursors method, Journal of Solid State Chemistry, 215 (2014) 211-218.

[152]   M. Kitano, K. Funatsu, M. Matsuoka, M. Ueshima, M. Anpo, Preparation of Nitrogen-Substituted TiO_2 Thin Film Photocatalysts by the Radio Frequency Magnetron Sputtering Deposition Method and Their Photocatalytic Reactivity

under Visible Light Irradiation, The Journal of Physical Chemistry B, 110 (2006) 25266-25272.

[153]   Y. Zeng, S. Zhang, Y. Wang, G. Liu, Q. Zhong, The effects of calcination atmosphere on the catalytic performance of Ce-doped TiO_2 catalysts for selective catalytic reduction of NO with NH3, RSC Advances, 7 (2017) 23348-23354.

[154]   D. Kim, S. Fujimoto, P. Schmuki, H. Tsuchiya, Nitrogen doped anodic TiO_2 nanotubes grown from nitrogen-containing Ti alloys, Electrochemistry Communications, 10 (2008) 910-913.

[155]   K.I. Liu, C.Y. Su, T.P. Perng, Highly porous N-doped TiO_2 hollow fibers with internal three-dimensional interconnected nanotubes for photocatalytic hydrogen production, RSC Advances, 5 (2015) 88367-88374.

[156]   R. Rattanakam, S. Supothina, Visible-light-sensitive N-doped TiO_2 photocatalysts prepared by a mechanochemical method: effect of a nitrogen source, Research on Chemical Intermediates, 35 (2009) 263-269.

[157]   C. Sarantopoulos, A.N. Gleizes, F. Maury, Chemical vapor deposition and characterization of nitrogen doped TiO_2 thin films on glass substrates, Thin Solid Films, 518 (2009) 1299-1303.

[158]   S. Suphankij, W. Mekprasart, W. Pecharapa, Photocatalytic of N-doped TiO_2 Nanofibers Prepared by Electrospinning, Energy Procedia, 34 (2013) 751-756.

[159]   C. Liu, L. Zhang, R. Liu, Z. Gao, X. Yang, Z. Tu, F. Yang, Z. Ye, L. Cui, C. Xu, Y. Li, Hydrothermal synthesis of N-doped TiO_2 nanowires and N-doped graphene heterostructures with enhanced photocatalytic properties, Journal of Alloys and Compounds, 656 (2016) 24-32.

[160]   Y. Cong, J. Zhang, F. Chen, M. Anpo, Synthesis and Characterization of Nitrogen-Doped TiO_2 Nanophotocatalyst with High Visible Light Activity, The Journal of Physical Chemistry C, 111 (2007) 6976-6982.

[161]   H.H.H. Lin, A.Y.C. Lin, C.L. Hung, Photocatalytic oxidation of cytostatic drugs by microwave-treated N-doped TiO_2 under visible light, Journal of Chemical Technology and Biotechnology, 90 (2015) 1345-1354.

[162]   S. Bangkedphol, H.E. Keenan, C.M. Davidson, A. Sakultantimetha, W. Sirisaksoontorn, A. Songsasen, Enhancement of tributyltin degradation under natural light by N-doped TiO$_2$ photocatalyst, Journal of Hazardous Materials, 184 (2010) 533-537.

[163]   G. Yang, Z. Jiang, H. Shi, T. Xiao, Z. Yan, Preparation of highly visible-light active N-doped TiO$_2$ photocatalyst, Journal of Materials Chemistry, 20 (2010) 5301-5309.

[164]   C. Stegemann, R.S. Moraes, D.A. Duarte, M. Massi, Thermal annealing effect on nitrogen-doped TiO$_2$ thin films grown by high power impulse magnetron sputtering plasma power source, Thin Solid Films, 625 (2017) 49-55.

[165]   S.-M. Oh, S.-S. Kim, J.E. Lee, T. Ishigaki, D.-W. Park, Effect of additives on photocatalytic activity of titanium dioxide powders synthesized by thermal plasma, Thin Solid Films, 435 (2003) 252-258.

[166]   X. Yan, J. He, D. G. Evans, X. Duan, Y. Zhu, Preparation, characterization and photocatalytic activity of Si-doped and rare earth-doped TiO$_2$ from mesoporous precursors, Applied Catalysis B: Environmental, 55 (2005) 243-252.

[167]   H. Ozaki, S. Iwamoto, M. Inoue, Enhanced Visible Light Sensitivity of Nitrogen-doped Nanocrystalline Si-modified Titania Prepared by the Glycothermal Method, Chemistry Letters, 34 (2005) 1082-1083.

[168]   H. Ozaki, S. Iwamoto, M. Inoue, Effect of the addition of a small amount of vanadium on the photocatalytic activities of N- and Si- co-doped titanias under visible-light irradiation, Catalysis Letters, 113 (2007) 95-98.

[169]   Y. Su, S. Chen, X. Quan, H. Zhao, Y. Zhang, A silicon-doped TiO$_2$ nanotube arrays electrode with enhanced photoelectrocatalytic activity, Applied Surface Science, 255 (2008) 2167-2172.

[170]   S. Iwamoto, W. Tanakulrungsank, M. Inoue, K. Kagawa, P. Praserthdam, Synthesis of large-surface area silica-modified titania ultrafine particles by the glycothermal method, Journal of Materials Science Letters, 19 (2000) 1439-1443.

[171]   S. Iwamoto, S. Iwamoto, M. Inoue, H. Yoshida, T. Tanaka, K. Kagawa, XANES and XPS Study of Silica-Modified Titanias Prepared by the Glycothermal Method, Chemistry of Materials, 17 (2005) 650-655.

[172]   K.Y. Jung, S.B. Park, Enhanced photoactivity of silica-embedded titania particles prepared by sol–gel process for the decomposition of trichloroethylene, Applied Catalysis B: Environmental, 25 (2000) 249-256.

[173]   K. Yang, Y. Dai, B. Huang, First-principles calculations for geometrical structures and electronic properties of Si-doped TiO_2, Chemical Physics Letters, 456 (2008) 71-75.

[174]   W. Shi, Q. Chen, Y. Xu, D. Wu, C. Huo, A first-principles calculation on the electronic properties of Si/N-codoped TiO_2, Applied Surface Science, 257 (2011) 3000-3006.

[175]   L. Run, J.E. Niall, Band gap engineering of (N, Si)-codoped TiO_2 from hybrid density functional theory calculations, New Journal of Physics, 14 (2012) 053007.

[176]   G.A. Sewvandi, Z. Tao, T. Kusunose, Y. Tanaka, S. Nakanishi, Q. Feng, Modification of TiO_2 electrode with organic silane interposed layer for high-performance of dye-sensitized solar cells, ACS applied materials & interfaces, 6 (2014) 5818-5826.

[177]   J. Zhao, M. Milanova, M.M. Warmoeskerken, V. Dutschk, Surface modification of TiO_2 nanoparticles with silane coupling agents, Colloids and surfaces A: Physicochemical and engineering aspects, 413 (2012) 273-279.

[178]   S.P. Pujari, L. Scheres, A. Marcelis, H. Zuilhof, Covalent surface modification of oxide surfaces, Angewandte Chemie International Edition, 53 (2014) 6322-6356.

[179]   M. Arun, S. Kantheti, R.R. Gaddam, R. Narayan, K. Raju, Surface modification of TiO_2 nanoparticles with 1, 3, 5-triazine based silane coupling agent and its cumulative effect on the properties of polyurethane composite coating, Journal of Polymer Research, 21 (2014) 1-11.

[180]   J.-S. Wang, K. Matyjaszewski, Controlled/"living" radical polymerization. atom transfer radical polymerization in the presence of transition-metal complexes, Journal of the American Chemical Society, 117 (1995) 5614-5615.

[181]   G.-Z. Li, R.K. Randev, A.H. Soeriyadi, G. Rees, C. Boyer, Z. Tong, T.P. Davis, C.R. Becer, D.M. Haddleton, Investigation into thiol-(meth)acrylate Michael addition reactions using amine and phosphine catalysts, Polymer Chemistry, 1 (2010) 1196-1204.

[182]   F. Guo, K. Jankova, L. Schulte, M.E. Vigild, S. Ndoni, One-Step Routes from Di- and Triblock Copolymer Precursors to Hydrophilic Nanoporous Poly(acrylic acid)-b-polystyrene, Macromolecules, 41 (2008) 1486-1493.

[183]   F. Guo, K. Jankova, L. Schulte, M.E. Vigild, S. Ndoni, Surface Modification of Nanoporous 1,2-Polybutadiene by Atom Transfer Radical Polymerization or Click Chemistry, Langmuir, 26 (2010) 2008-2013.

[184]   S. Pazokifard, M. Esfandeh, S.M. Mirabedini, M. Mohseni, Z. Ranjbar, Investigating the role of surface treated titanium dioxide nanoparticles on self-cleaning behavior of an acrylic facade coating, J Coat Technol Res, 10 (2013) 175-187.

[185]   Y. Gu, X. Liu, T. Niu, J. Huang, Superparamagnetic hierarchical material fabricated by protein molecule assembly on natural cellulose nanofibres, Chemical Communications, 46 (2010) 6096-6098.

[186]   S.N. Rashkeev, S. Dai, S.H. Overbury, Modification of Au/TiO_2 Nanosystems by SiO2 Monolayers: Toward the Control of the Catalyst Activity and Stability, The Journal of Physical Chemistry C, 114 (2010) 2996-3002.

[187]   R.A.F. Grieve, F. Langenhorst, D. Stöffler, Shock metamorphism of quartz in nature and experiment: II. Significance in geoscience, Meteoritics and Planetary Science, 31 (1996) 6-35.

[188]   S.T. Martin, H.M. Hung, R.J. Park, D.J. Jacob, R.J.D. Spurr, K.V. Chance, M. Chin, Effects of the physical state of tropospheric ammonium-sulfate-nitrate particles on global aerosol direct radiative forcing, Atmospheric Chemistry and Physics, 4 (2004) 183-214.

[189]   T. Tubchareon, S. Soisuwan, S. Ratanathammaphan, P. Praserthdam, Effect of Na-, K-, Mg-, and Ga dopants in A/B-sites on the optical band gap and photoluminescence behavior of $[Ba_{0.5}Sr_{0.5}]TiO_3$ powders, Journal of Luminescence, 142 (2013) 75-80.

[190]   S.K. Lee, P.K.J. Robertson, A. Mills, D. McStay, N. Elliott, D. McPhail, The alteration of the structural properties and photocatalytic activity of TiO_2 following exposure to non-linear irradiation sources, Applied Catalysis B: Environmental, 44 (2003) 173-184.

[191]   K. Suriye, P. Praserthdam, B. Jongsomjit, Control of Ti^{3+} surface defect on TiO_2 nanocrystal using various calcination atmospheres as the first step for surface defect creation and its application in photocatalysis, Applied Surface Science, 253 (2007) 3849-3855.

[192]   E. Carter, A.F. Carley, D.M. Murphy, Evidence for O_2 - radical stabilization at surface oxygen vacancies on polycrystalline TiO_2, Journal of Physical Chemistry C, 111 (2007) 10630-10638.

[193]   D.C. Hurum, A.G. Agrios, K.A. Gray, T. Rajh, M.C. Thurnauer, Explaining the enhanced photocatalytic activity of Degussa P25 mixed-phase TiO_2 using EPR, Journal of Physical Chemistry B, 107 (2003) 4545-4549.

[194]   G. Riegal, J.R. Bolton, Photocatalytic efficiency variability in TiO_2 particles, Journal of physical chemistry, 99 (1995) 4215-4224.

[195]   X. Shao, W. Lu, R. Zhang, F. Pan, Enhanced photocatalytic activity of TiO_2-C hybrid aerogels for methylene blue degradation, Sci. Rep., 3 (2013).

[196]   M. Sakeye, J.-H. Smått, Comparison of Different Amino-Functionalization Procedures on a Selection of Metal Oxide Microparticles: Degree of Modification and Hydrolytic Stability, Langmuir, 28 (2012) 16941-16950.

[197]   J.M. Rosenholm, M. Lindén, Wet-Chemical Analysis of Surface Concentration of Accessible Groups on Different Amino-Functionalized Mesoporous SBA-15 Silicas, Chemistry of Materials, 19 (2007) 5023-5034.

[198]   B. De Witte, K. Vercruysse, K. Aernouts, P. Verwimp, J.B. Uytterhoeven, N_2-adsorption on amorphous aluminosilicates: Application of the Kelvin equation

and the T-plot analysis for mixed micro-mesoporous materials, J Porous Mater, 2 (1996) 307-313.

[199]   E.I. Basaldella, J.C. Tara, G.A. Armenta, M.E. Patiño-Iglesias, E.R. Castellón, Propane/propylene separation by selective olefin adsorption on Cu/SBA-15 mesoporous silica, Journal of Sol-Gel Science and Technology, 37 (2006) 141-146.

[200]   A. Senthilraja, B. Krishnakumar, B. Subash, A.J.F.N. Sobral, M. Swaminathan, M. Shanthi, Sn loaded Au–ZnO photocatalyst for the degradation of AR 18 dye under UV-A light, Journal of Industrial and Engineering Chemistry, 33 (2016) 51-58.

[201]   C.-C. Chen, S.-H. Hu, Y.-P. Fu, Effects of surface hydroxyl group density on the photocatalytic activity of Fe^{3+}-doped TiO_2, Journal of Alloys and Compounds, 632 (2015) 326-334.

[202]   R. Mueller, H.K. Kammler, K. Wegner, S.E. Pratsinis, OH Surface Density of SiO_2 and TiO_2 by Thermogravimetric Analysis, Langmuir, 19 (2003) 160-165.

[203]   G.S. Avcioglu, B. Ficicilar, A. Bayrakceken, I. Eroglu, High performance PEM fuel cell catalyst layers with hydrophobic channels, International Journal of Hydrogen Energy, 40 (2015) 7720-7731.

[204]   A.G. Rusu, M.I. Popa, G. Lisa, L. Vereştiuc, Thermal behavior of hydrophobically modified hydrogels using TGA/FTIR/MS analysis technique, Thermochimica Acta, (2015).

[205]   J.G. Kim, D.L. Pugmire, D. Battaglia, M.A. Langell, Analysis of the $NiCo_2O_4$ spinel surface with Auger and X-ray photoelectron spectroscopy, Applied Surface Science, 165 (2000) 70-84.

[206]   S. Kaciulis, G. Mattogno, A. Galdikas, A. Mironas, A. Šetkus, Influence of surface oxygen on chemoresistance of tin oxide film, Journal of Vacuum Science & Technology A, 14 (1996) 3164-3168.

[207]   L.M. Pastrana-Martínez, S. Morales-Torres, V. Likodimos, P. Falaras, J.L. Figueiredo, J.L. Faria, A.M.T. Silva, Role of oxygen functionalities on the synthesis of photocatalytically active graphene–TiO_2 composites, Applied Catalysis B: Environmental, 158–159 (2014) 329-340.

[208]   S. Dauphas, S. Ababou-Girard, A. Girard, F. Le Bihan, T. Mohammed-Brahim, V. Vié, A. Corlu, C. Guguen-Guillouzo, O. Lavastre, F. Geneste, Stepwise functionalization of SiNx surfaces for covalent immobilization of antibodies, Thin Solid Films, 517 (2009) 6016-6022.

[209]   I. George, P. Viel, C. Bureau, J. Suski, G. Lécayon, Study of the Silicon/**γ**-APS/Pyralin Assembly Interfaces by X-ray Photoelectron Spectroscopy, Surface and Interface Analysis, 24 (1996) 774-780.

[210]   E.T. Vandenberg, L. Bertilsson, B. Liedberg, K. Uvdal, R. Erlandsson, H. Elwing, I. Lundström, Structure of 3-aminopropyl triethoxy silane on silicon oxide, Journal of Colloid and Interface Science, 147 (1991) 103-118.

[211]   R.M. Pasternack, S. Rivillon Amy, Y.J. Chabal, Attachment of 3-(Aminopropyl)triethoxysilane on Silicon Oxide Surfaces: Dependence on Solution Temperature, Langmuir, 24 (2008) 12963-12971.

[212]   A. Arranz, C. Palacio, D. García-Fresnadillo, G. Orellana, A. Navarro, E. Muñoz, Influence of Surface Hydroxylation on 3-Aminopropyltriethoxysilane Growth Mode during Chemical Functionalization of GaN Surfaces: An Angle-Resolved X-ray Photoelectron Spectroscopy Study, Langmuir, 24 (2008) 8667-8671.

[213]   M. Jang, C.K. Park, N.Y. Lee, Modification of polycarbonate with hydrophilic/hydrophobic coatings for the fabrication of microdevices, Sensors and Actuators B: Chemical, 193 (2014) 599-607.

[214]   S. Gautam, K.-C. Loh, Immobilization of hydrophobic peptidic ligands to hydrophilic chromatographic matrix: A preconcentration approach, Analytical Biochemistry, 423 (2012) 202-209.

[215]   A.A. Golub, A.I. Zubenko, B.V. Zhmud, **γ**-APTES Modified Silica Gels: The Structure of the Surface Layer, Journal of Colloid and Interface Science, 179 (1996) 482-487.

[216]   V. Ääritalo, M. Piispanen, A. Rosling, S. Areva, Silicon releasing sol–gel TiO_2–SiO230/70 films, Thin Solid Films, 519 (2011) 7845-7849.

[217]   M.R. Alexander, R.D. Short, F.R. Jones, W. Michaeli, C.J. Blomfield, A study of HMDSO/O_2 plasma deposits using a high-sensitivity and -energy resolution XPS

instrument: curve fitting of the Si 2p core level, Applied Surface Science, 137 (1999) 179-183.

[218] H. Wang, X. Yuan, Y. Wu, G. Zeng, X. Chen, L. Leng, H. Li, Synthesis and applications of novel graphitic carbon nitride/metal-organic frameworks mesoporous photocatalyst for dyes removal, Applied Catalysis B: Environmental, 174–175 (2015) 445-454.

[219] G.D. Rajmohan, X.J. Dai, T. Tsuzuki, P.R. Lamb, J. du Plessis, F. Huang, Y.-B. Cheng, Modifying TiO2 surface architecture by oxygen plasma to increase dye sensitized solar cell efficiency, Thin Solid Films, 545 (2013) 521-526.

[220] N. Singh, K.K. Reza, M.A. Ali, V.V. Agrawal, A.M. Biradar, Self assembled DC sputtered nanostructured rutile TiO_2 platform for bisphenol A detection, Biosensors and Bioelectronics, 68 (2015) 633-641.

[221] S. Sareen, V. Mutreja, B. Pal, S. Singh, Homogeneous dispersion of Au nanoparticles into mesoporous SBA-15 exhibiting improved catalytic activity for nitroaromatic reduction, Microporous and Mesoporous Materials, 202 (2015) 219-225.

[222] M.r.L.c. Moreira, P.G.C. Buzolin, V.M. Longo, N.H. Nicoleti, J.R. Sambrano, M.S. Li, J.A. Varela, E. Longo, Joint Experimental and Theoretical Analysis of Order–Disorder Effects in Cubic $BaZrO_3$ Assembled Nanoparticles under Decaoctahedral Shape, The Journal of Physical Chemistry A, 115 (2011) 4482-4490.

[223] H. Wang, T. Lin, G. Zhu, H. Yin, X. Lü, Y. Li, F. Huang, Colored titania nanocrystals and excellent photocatalysis for water cleaning, Catalysis Communications, 60 (2015) 55-59.

[224] J.C. Parker, R.W. Siegel, Raman microprobe study of nanophase TiO_2 and oxidation-induced spectral changes, Journal of Materials Research, 5, pp 1246-1252. doi:10.1557/JMR.1990.1246. , 5 (1990) 1246-1252.

[225] M.V. Yakushev, I. Forbes, A.V. Mudryi, M. Grossberg, J. Krustok, N.S. Beattie, M. Moynihan, A. Rockett, R.W. Martin, Optical spectroscopy studies of $Cu_2ZnSnSe_4$ thin films, Thin Solid Films, 582 (2015) 154-157.

[226]   T. Qiu, X.L. Wu, F. Kong, H.B. Ma, P.K. Chu, Solvent effect on light-emitting property of Si nanocrystals, Physics Letters A, 334 (2005) 447-452.

[227]   J. Xu, L. Li, Y. Yan, H. Wang, X. Wang, X. Fu, G. Li, Synthesis and photoluminescence of well-dispersible anatase TiO_2 nanoparticles, Journal of Colloid and Interface Science, 318 (2008) 29-34.

[228]   B. Santara, P.K. Giri, K. Imakita, M. Fujii, Evidence of oxygen vacancy induced room temperature ferromagnetism in solvothermally synthesized undoped TiO_2 nanoribbons, Nanoscale, 5 (2013) 5476-5488.

[229]   Z.-M. Liao, H.-Z. Zhang, Y.-B. Zhou, J. Xu, J.-M. Zhang, D.-P. Yu, Surface effects on photoluminescence of single ZnO nanowires, Physics Letters A, 372 (2008) 4505-4509.

[230]   Y.-Y. Song, H. Hildebrand, P. Schmuki, Optimized monolayer grafting of 3-aminopropyltriethoxysilane onto amorphous, anatase and rutile TiO_2, Surface Science, 604 (2010) 346-353.

[231]   P.I. Pontón, J.R.M. d'Almeida, B.A. Marinkovic, S.M. Savić, L. Mancic, N.A. Rey, E. Morgado Jr, F.C. Rizzo, The effects of the chemical composition of titanate nanotubes and solvent type on 3-aminopropyltriethoxysilane grafting efficiency, Applied Surface Science, 301 (2014) 315-322.

[232]   F. Cuoq, A. Masion, J. Labille, J. Rose, F. Ziarelli, B. Prelot, J.-Y. Bottero, Preparation of amino-functionalized silica in aqueous conditions, Applied Surface Science, 266 (2013) 155-160.

[233]   J.-E. Lee, N.T. Khoa, S.W. Kim, E.J. Kim, S.H. Hahn, Fabrication of Au/GO/ZnO composite nanostructures with excellent photocatalytic performance, Materials Chemistry and Physics, 164 (2015) 29-35.

[234]   E.S. Aazam, Photocatalytic oxidation of methylene blue dye under visible light by Ni doped Ag2S nanoparticles, Journal of Industrial and Engineering Chemistry, 20 (2014) 4033-4038.

[235]   N. Farahani, P.J. Kelly, G. West, M. Ratova, C. Hill, V. Vishnyakov, Photocatalytic activity of reactively sputtered and directly sputtered titania coatings, Thin Solid Films, 520 (2011) 1464-1469.

[236]   M. Ratova, P.J. Kelly, G.T. West, L. Tosheva, M. Edge, Reactive magnetron sputtering deposition of bismuth tungstate onto titania nanoparticles for enhancing visible light photocatalytic activity, Aplied Surface Science, 392 (2017) 7.

[237]   K.I. Schiffmann, M. Fryda, G. Goerigk, R. Lauer, P. Hinze, A. Bulack, Sizes and distances of metal clusters in Au-, Pt-, W- and Fe-containing diamond-like carbon hard coatings: a comparative study by small angle X-ray scattering, wide angle X-ray diffraction, transmission electron microscopy and scanning tunnelling microscopy, Thin Solid Films, 347 (1999) 60-71.

[238]   K.-C. Chen, F.C.-N. Hong, Y.-R. Jeng, Deposition of Titania-containing Diamond-like Carbon Nanocomposite Films by Sputtering-assisted Chemical Vapor Deposition, Plasma Processes and Polymers, 8 (2011) 324-332.

[239]   M.S. Hamdy, R. Amrollahi, G. Mul, Surface Ti^{3+}-Containing (blue) Titania: A Unique Photocatalyst with High Activity and Selectivity in Visible Light-Stimulated Selective Oxidation, ACS Catalysis, 2 (2012) 2641-2647.

[240]   L.-B. Xiong, J.-L. Li, B. Yang, Y. Yu, Ti^{3+} in the Surface of Titanium Dioxide: Generation, Properties and Photocatalytic Application, Journal of Nanomaterials, 2012 (2012) 13.

[241]   W. Mai, F. Wen, D. Xie, Y. Leng, Z. Mu, Structure and composition study of carbon-doped titanium oxide film combined with first principles, Journal of Advanced Ceramics, 3 (2014) 49-55.

[242]   Y. Cheng, H. Sun, W. Jin, N. Xu, Photocatalytic degradation of 4-chlorophenol with combustion synthesized TiO_2 under visible light irradiation, Chemical Engineering Journal, 128 (2007) 127-133.

[243]   F. Zhang, S. Jin, Y. Mao, Z. Zheng, Y. Chen, X. Liu, Surface characterization of titanium oxide films synthesized by ion beam enhanced deposition, Thin Solid Films, 310 (1997) 29-33.

[244]   Y. Park, W. Kim, H. Park, T. Tachikawa, T. Majima, W. Choi, Carbon-doped TiO_2 photocatalyst synthesized without using an external carbon precursor and the visible light activity, Applied Catalysis B: Environmental, 91 (2009) 355-361.

[245] D. Xie, F. Wen, W. Yang, X. Li, Y. Leng, G. Wan, H. Sun, N. Huang, Carbon-Doped Titanium Oxide Films by DC Reactive Magnetron Sputtering Using CO_2 and O_2 as Reactive Gas, Acta Metallurgica Sinica (English Letters), 27 (2014) 239-244.

[246] S.-W. Hsu, T.-S. Yang, T.-K. Chen, M.-S. Wong, Ion-assisted electron-beam evaporation of carbon-doped titanium oxide films as visible-light photocatalyst, Thin Solid Films, 515 (2007) 3521-3526.

[247] M.-S. Wong, S.-W. Hsu, K.K. Rao, C.P. Kumar, Influence of crystallinity and carbon content on visible light photocatalysis of carbon doped titania thin films, Journal of Molecular Catalysis A: Chemical, 279 (2008) 20-26.

[248] S.-H. Wang, T.-K. Chen, K.K. Rao, M.-S. Wong, Nanocolumnar titania thin films uniquely incorporated with carbon for visible light photocatalysis, Applied Catalysis B: Environmental, 76 (2007) 328-334.

[249] G. Soto, AES, EELS and XPS characterization of Ti(C, N, O) films prepared by PLD using a Ti target in N_2, CH_4, O_2 and CO as reactive gases, Applied Surface Science, 233 (2004) 115-122.

[250] J. Tauc, Optical properties and electronic structure of amorphous Ge and Si, Materials Research Bulletin, 3 (1968) 37-46.

[251] K. Taizo, K. Satoshi, TiO_2 patterns with wide photo-induced wettability change by a combination of reactive sputtering process and surface modification in a microfluidic channel, Journal of Micromechanics and Microengineering, 25 (2015) 115014.

[252] R.-D. Sun, A. Nakajima, A. Fujishima, T. Watanabe, K. Hashimoto, Photoinduced Surface Wettability Conversion of ZnO and TiO_2 Thin Films, The Journal of Physical Chemistry B, 105 (2001) 1984-1990.

[253] F.M. Meng, F. Lu, Z.Q. Sun, J.G. Lu, A mechanism for enhanced photocatalytic activity of nano-size silver particle modified titanium dioxide thin films, Science China-Technological Sciences, 53 (2010) 3027-3032.

[254] A. Mills, C. Hill, P.K.J. Robertson, Overview of the current ISO tests for photocatalytic materials, Journal of Photochemistry and Photobiology A: Chemistry, 237 (2012) 7-23.

[255]   P. Evans, S. Mantke, A. Mills, A. Robinson, D.W. Sheel, A comparative study of three techniques for determining photocatalytic activity, Journal of Photochemistry and Photobiology A: Chemistry, 188 (2007) 387-391.

[256]   A. Mills, N. Wells, C. O'Rourke, Correlation between ΔAbs, ΔRGB (red) and stearic acid destruction rates using commercial self-cleaning glass as the photocatalyst, Catalysis Today, 230 (2014) 245-249.

[257]   C. Xie, S. Yang, B. Li, H. Wang, J.-W. Shi, G. Li, C. Niu, C-doped mesoporous anatase TiO_2 comprising 10 nm crystallites, Journal of Colloid and Interface Science, 476 (2016) 1-8.

[258]   Y.-T. Lin, C.-H. Weng, Y.-H. Lin, C.-C. Shiesh, F.-Y. Chen, Effect of C content and calcination temperature on the photocatalytic activity of C-doped TiO_2 catalyst, Separation and Purification Technology, 116 (2013) 114-123.

[259]   F. Wen, C. Zhang, D. Xie, H. Sun, Y.X. Leng, Research of composition and photocatalytic property of carbon-doped Ti-O films prepared by R-MS using CO_2 gas resource, Nuclear Instruments & Methods in Physics Research Section B-Beam Interactions with Materials and Atoms, 307 (2013) 381-384.

[260]   C.W.H. Dunnill, Z.A. Aiken, J. Pratten, M. Wilson, D.J. Morgan, I.P. Parkin, Enhanced photocatalytic activity under visible light in N-doped TiO_2 thin films produced by APCVD preparations using t-butylamine as a nitrogen source and their potential for antibacterial films, Journal of Photochemistry and Photobiology A: Chemistry, 207 (2009) 244-253.

[261]   D. Zhang, Y.R. Shen, G.A. Somorjai, Studies of surface structures and compositions of polyethylene and polypropylene by IR^+visible sum frequency vibrational spectroscopy, Chemical Physics Letters, 281 (1997) 394-400.

[262]   E. Smidt, K. Meissl, The applicability of Fourier transform infrared (FT-IR) spectroscopy in waste management, Waste Management, 27 (2007) 268-276.

[263]   C. Ramírez, M. Rico, A. Torres, L. Barral, J. López, B. Montero, Epoxy/POSS organic–inorganic hybrids: ATR-FTIR and DSC studies, European Polymer Journal, 44 (2008) 3035-3045.

[264]   A. El-masry, H. Fahmy, S. Ali Abdelwahed, Synthesis and Antimicrobial Activity of Some New Benzimidazole Derivatives, Molecules, 5 (2000) 1429.

[265]   A.W. Kawaguchi, A. Sudo, T. Endo, Synthesis of highly polymerizable 1,3-benzoxazine assisted by phenyl thio ether and hydroxyl moieties, Journal of Polymer Science Part A: Polymer Chemistry, 50 (2012) 1457-1461.

[266]   Y. Zhang, P. Talalay, C.G. Cho, G.H. Posner, A major inducer of anticarcinogenic protective enzymes from broccoli: isolation and elucidation of structure, Proceedings of the National Academy of Sciences, 89 (1992) 2399-2403.

[267]   Q. Liu, Y. Chen, Synthesis of well-defined macromonomers by the combination of atom transfer radical polymerization and a click reaction, Journal of Polymer Science Part A: Polymer Chemistry, 44 (2006) 6103-6113.

[268]   H. Akmal, N. Hairul, M. Zulfakar, M. Zulkali, Controlled/Living Radical Polymerization of Methyl Methacrylate in the Presence of 2-Bromoethanol as a Transfer Agent and Comparison with Cumyl Dithiobenzoate as a RAFT Agent, Journal of Applied Sciences, 9 (2009) 3146-3150.

[269]   G.-W. Wang, J.-J. Xia, C.-B. Miao, X.-L. Wu, Environmentally Friendly and Efficient Synthesis of Various 1,4-Dihydropyridines in Pure Water, Bulletin of the Chemical Society of Japan, 79 (2006) 454-459.

[270]   M.A. Mikita, C. Steelink, R.L. Wershaw, Carbon-13 enriched nuclear magnetic resonance method for the determination of hydroxyl functionality in humic substances, Analytical Chemistry, 53 (1981) 1715-1717.

[271]   K. Ala'a, Isolation, separation and characterisation of the fullerenes C 60 and C 70: the third form of carbon, Journal of the Chemical Society, Chemical Communications, (1990) 1423-1425.

[272]   G. Guggenberger, W. Zech, L. Haumaier, B.T. Christensen, Land-use effects on the composition of organic matter in particle-size separates of soils: II. CPMAS and solution 13C NMR analysis, European Journal of Soil Science, 46 (1995) 147-158.

[273]   A.G. Brown, T.C. Smale, T.J. King, R. Hasenkamp, R.H. Thompson, Crystal and molecular structure of compactin, a new antifungal metabolite from Penicillium brevicompactum, Journal of the Chemical Society, Perkin Transactions 1, (1976) 1165-1170.

[274] L.N. Arakaki, C. Airoldi, Ethylenimine in the synthetic routes of a new silylating agent: chelating ability of nitrogen and sulfur donor atoms after anchoring onto the surface of silica gel, Polyhedron, 19 (2000) 367-373.

[275] B.L. Buckwalter, I.R. Burfitt, A.A. Nagel, E. Wenkert, F. Näf, ^{13}C-NMR. Spectroscopy of Naturally Occurring Substances. XXXV. Labdanic diterpenes, Helvetica Chimica Acta, 58 (1975) 1567-1573.

[276] S. Dalton, F. Heatley, P.M. Budd, Thermal stabilization of polyacrylonitrile fibres, Polymer, 40 (1999) 5531-5543.

[277] T. Hiyama, S. Fujita, H. Nozaki, The Photochemistry of 4, 5-Disubstituted 1, 3-Dioxolen-2-ones, Bulletin of the Chemical Society of Japan, 45 (1972) 2797-2801.

[278] R.N. Jones, P. Humphries, K. Dobriner, Studies in Steroid Metabolism. VI. The Characterization of 11-and 12-Oxygenated Steroids by Infrared Spectrometry, Journal of the American Chemical Society, 71 (1949) 241-247.

[279] P. Painter, M. Coleman, R. Snyder, O. Mahajan, M. Komatsu, P. Walker, Low temperature air oxidation of caking coals: Fourier transform infrared studies, Applied Spectroscopy, 35 (1981) 106-110.

[280] X. Hu, H. Li, Y. Liang, Y. Wei, Z. Yu, D. Marshall, J. Edwards Jr, R. Droopad, X. Zhang, A. Demkov, The interface of epitaxial $SrTiO_3$ on silicon: in situ and ex situ studies, Applied physics letters, 82 (2003) 203-205.

[281] W. Lee, J. Lee, P. Reucroft, XPS study of carbon fiber surfaces treated by thermal oxidation in a gas mixture of $O_2/(O_2+ N_2)$, Applied Surface Science, 171 (2001) 136-142.

[282] A.P. Terzyk, The influence of activated carbon surface chemical composition on the adsorption of acetaminophen (paracetamol) in vitro: Part II. TG, FTIR, and XPS analysis of carbons and the temperature dependence of adsorption kinetics at the neutral pH, Colloids and Surfaces A: Physicochemical and Engineering Aspects, 177 (2001) 23-45.

[283] Y. Choi, T. Umebayashi, M. Yoshikawa, Fabrication and characterization of C-doped anatase TiO_2 photocatalysts, Journal of Materials Science, 39 (2004) 1837-1839.

[284]   X. Zhang, H. Tian, X. Wang, G. Xue, Z. Tian, J. Zhang, S. Yuan, T. Yu, Z. Zou, The role of oxygen vacancy-Ti^{3+} states on TiO$_2$ nanotubes' surface in dye-sensitized solar cells, Materials Letters, 100 (2013) 51-53.

[285]   F.N. Sayed, O.D. Jayakumar, R. Sasikala, R.M. Kadam, S.R. Bharadwaj, L. Kienle, U. Schürmann, S. Kaps, R. Adelung, J.P. Mittal, A.K. Tyagi, Photochemical Hydrogen Generation Using Nitrogen-Doped TiO$_2$–Pd Nanoparticles: Facile Synthesis and Effect of Ti3+ Incorporation, The Journal of Physical Chemistry C, 116 (2012) 12462-12467.

[286]   J. Zhu, F. Chen, J. Zhang, H. Chen, M. Anpo, Fe^{3+}-TiO$_2$ photocatalysts prepared by combining sol–gel method with hydrothermal treatment and their characterization, Journal of Photochemistry and Photobiology A: Chemistry, 180 (2006) 196-204.

[287]   B.-Y. Jia, L.-Y. Duan, C.-L. Ma, C.-M. Wang, Characterization of TiO$_2$ Loaded on Activated Carbon Fibers and Its Photocatalytic Reactivity, Chinese Journal of Chemistry, 25 (2007) 553-557.

[288]   S. Kango, S. Kalia, A. Celli, J. Njuguna, Y. Habibi, R. Kumar, Surface modification of inorganic nanoparticles for development of organic–inorganic nanocomposites—a review, Progress in Polymer Science, 38 (2013) 1232-1261.

[289]   G. Kickelbick, Concepts for the incorporation of inorganic building blocks into organic polymers on a nanoscale, Progress in polymer science, 28 (2003) 83-114.

APPENDIX

APPENDIX A

CALCULATION FOR CATALYST PREPARATION

1. **Preparation of 1 wt.% Si-doped titanium dioxide catalysts by solvothermal method**

Preparation of 1 wt.% Si-doped titanium dioxide catalysts by solvothermal method is presented as follows:

Precursor

- Titanium (IV) butoxide (TNB), MW = 340.32, 97% purity
- Titanium dioxide (TiO_2), MW = 79.866
- Tetraethyl orthosilicate (TEOS), MW = 208.33, 98% purity
- Silicon (Si), MW = 28.0855

Calculation

How many grams of TiO_2 from 15 g of TNB?

$$\frac{15 \text{ g TNB}}{} \times \frac{79.866 \text{ g TiO}_2}{340.32 \text{ g TNB}} \times \frac{97}{100} = \frac{3.41 \text{ g TiO}_2}{}$$

How many grams of TEOS required?

$$\frac{3.41 \text{ g TiO}_2}{99 \text{ g TiO}_2} \times \frac{1 \text{ g Si}}{28.0855 \text{ g Si}} \times \frac{208.33 \text{ g TEOS}}{} \times \frac{100}{98} = \frac{0.2607 \text{ g TEOS}}{}$$

2. Preparation of 1 wt.% Si-doped titanium dioxide catalysts by sol-gel method

Preparation of 1 wt.% Si-doped titanium dioxide catalysts by sol-gel method is presented as follows:

Precursor

- Titanium (IV) isopropoxide (TTIP), MW = 284.22, 97% purity
- Titanium dioxide (TiO$_2$), MW = 79.866
- Tetraethyl orthosilicate (TEOS), MW = 208.33, 98% purity
- Silicon (Si), MW = 28.0855

Calculation

How many grams of TiO$_2$ from 166.8 mL of TTIP?

$$\frac{166.8 \text{ mL TTIP}}{} \times \frac{0.96 \text{ g TTIP}}{1 \text{ mL TTIP}} \times \frac{79.866 \text{ g TiO}_2}{284.221 \text{ mL TTIP g TTIP}} \times \frac{97}{100} = \frac{43.65 \text{ g TiO}_2}{}$$

How many grams of TiO$_2$ from 100 mL of solution?

$$\frac{100 \text{ mL Solution}}{} \times \frac{43.65 \text{ g TiO}_2}{2181.2 \text{ mL Solution}} = \frac{2.00 \text{ g TiO}_2}{}$$

How many grams of TEOS required?

$$\frac{2.00 \text{ g TiO}_2}{} \times \frac{1 \text{ g Si}}{99 \text{ g TiO}_2} \times \frac{208.33 \text{ g TEOS}}{28.0855 \text{ g Si}} \times \frac{100}{98} = \frac{0.1529 \text{ g TEOS}}{}$$

3. **Preparation of 1 mM of APTES modified titanium dioxide catalysts by hydrothermal method**

Preparation of 1 mM of APTES modified titanium dioxide catalysts by hydrothermal method is presented as follows:

Precursor

- APTES, MW = 221.37, 99% purity

Calculation

How many grams of APTES required?

$$\frac{100 \text{ mL Toluene}}{} \times \frac{0.001 \text{ mol APTES}}{1000 \text{ mL Toluene}} \times \frac{221.37 \text{ g APTES}}{1 \text{ mol APTES}} \times \frac{100}{99} = \frac{0.0223 \text{ g APTES}}{}$$

จุฬาลงกรณ์มหาวิทยาลัย

CHULALONGKORN UNIVERSITY

APPENDIX B

CALCULATION OF CRYSTALLITE SIZE

Calculation of the crystallite size by using the Debye-Scherrer equation

The crystallite size was calculated from the width at half of height (or full-width-half-max) of diffraction peak of the XRD pattern by using the Debye-Scherrer equation.

$$D = \frac{K\lambda}{\beta \cos\theta}$$

where D = Crystallite size, A°

K = Crystallite-shape factor or Scherrer constant depending on shape

of crystal (= 0.9 for FWHM of spherical crystals with cubic symmetry)

λ = X-ray wavelength, (=1.5418 A° for CuKα)

θ = Observed peak angle, degree

β = X-ray diffraction broadening, radian

The X-ray diffraction broadening (β) is the pure full-width-half-max of powder diffraction peak free from all broadening because of the experimental equipment or diffractometer. For a standard sample, α-Alumina is used as a standard sample to observe the instrumental broadening due to its crystallite size larger than 2000 A°. The X-ray diffraction broadening (β) can be determined by using the Warren's formula. According to Warren's formula:

$$\beta = \sqrt{B_M^2 - B_S^2}$$

Where B_M = Measured peak width at half of peak height, radian

B_S = Corresponding full-width-half-max of the standard material (i.e.,

α-Alumina), radian

Example: Calculation of the crystallite size of anatase TiO_2

The major peak of anatase TiO_2 was observed at 25.48° 2θ.

Full-width-half-max of diffraction peak at 25.48° = 0.526°

$$= \frac{(2\pi \times 0.526°)}{360}$$

$$= 0.00918 \text{ radian}$$

Corresponding full-width-half-max of α-alumina of diffraction peak at 25.48°

= 0.00383 radian

$$\beta = \sqrt{B_M^2 - B_S^2}$$

$$= \sqrt{(0.00918)^2 - (0.00383)^2}$$

$$= 0.00834 \text{ radian}$$

Thus,

β = 0.00834 radian

2θ = 25.48° ➜ θ = 12.74°

λ = 1.5418 A° for CuKα

Crystallite size, $\quad D = \dfrac{K\lambda}{\beta \cos\theta}$

$$= \frac{0.9 \times 1.5418}{0.00834 \times \cos 12.74°}$$

$$= 168.52 \text{ A°}$$

$$= 16.852 \text{ nm}$$
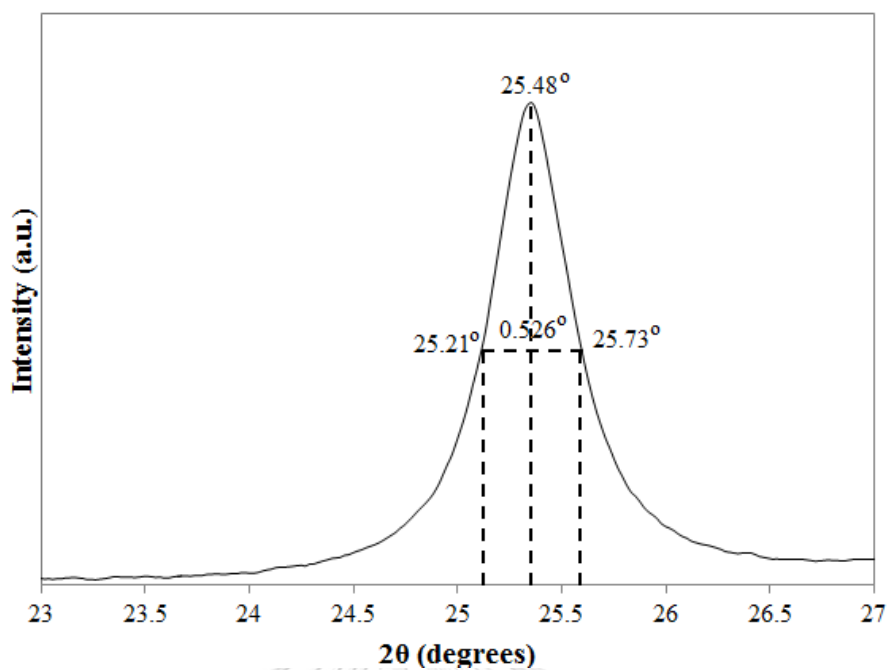
Figure B.1 *The measured XRD peak of anatase TiO$_2$ for calculation of crystallite size of anatase TiO$_2$*
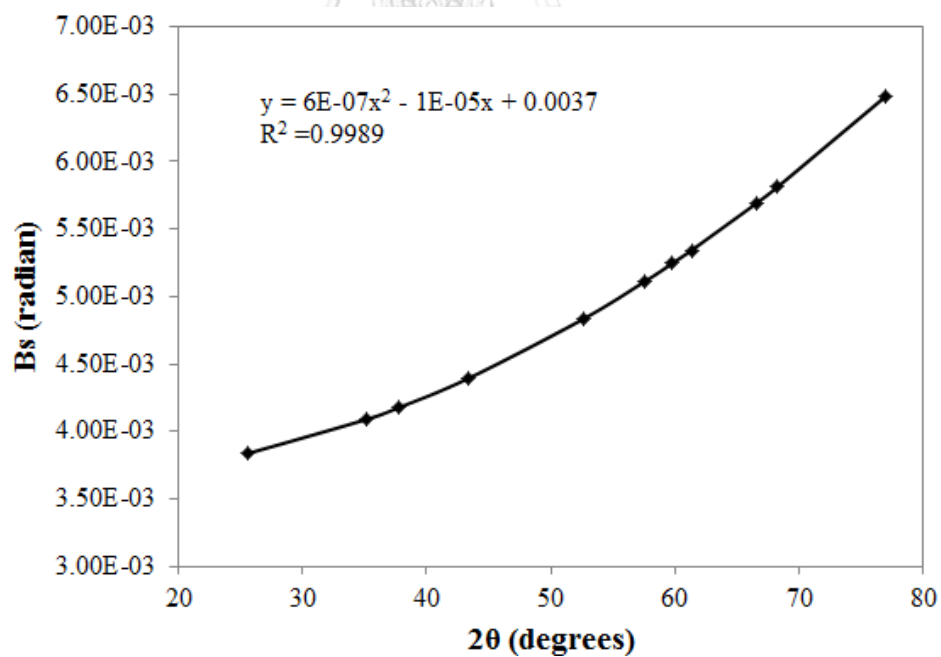
Figure B.2 *The plot indicating the value of line broadening because of the equipment (data were obtained by using **α**-alumina as standard material)*

APPENDIX C

PHASE CONTENT CALCULATION

The relative intensities of anatase and rutile diffraction peaks are different for the TiO_2 samples obtained at different preparation methods. The phase compositions of the TiO_2 samples were obtained from the equation suggested by Spurr and Myers:

$$f = \frac{1}{1 + 1.26 \dfrac{I_R}{I_A}}$$

where f is the weight fraction of anatase in the mixture and I_A and I_R are the XRD intensities of the strongest diffraction peaks of anatase (101) and rutile (110), respectively.

LIST OF PUBLICATIONS

- **First author publications**

1. **R. Klaysri**, S. Wichaidit, T. Tubchareon, S. Nokjan, S. Piticharoenphun, O. Mekasuwandumrong, P. Praserthdam, Impact of calcination atmospheres on the physiochemical and photocatalytic properties of nanocrystalline TiO_2 and Si-doped TiO_2, Ceramics International, 41 (2015) 11409-11417.

2. **R. Klaysri**, S. Wichaidit, S. Piticharoenphun, O. Mekasuwandumrong, P. Praserthdam, Synthesis of TiO_2-grafted onto PMMA film via ATRP: Using monomer as a coupling agent and reusability in photocatalytic application, Materials Research Bulletin, 83 (2016) 640-648.

3. **R. Klaysri**, T. Tubchareon, P. Praserthdam, One-step synthesis of amine-functionalized TiO_2 surface for photocatalytic decolorization under visible light irradiation, Journal of Industrial and Engineering Chemistry, 45 (2017) 229-236.

4. **R. Klaysri**, M. Ratova, P. Praserthdam, P. Kelly, Deposition of Visible Light-Active C-Doped Titania Films via Magnetron Sputtering Using CO_2 as a Source of Carbon, Nanomaterials, 7 (2017) 113.

- **Co-author publications**

5. T. Tubchareon, **R. Klaysri**, P. Praserthdam, A Comparison of Different A-, A-B-, and B-Site Incorporated in $(Ba_{0.5}Sr_{0.5})TiO_3$ on Photocatalytic Application, Advances in Optical Technologies, 2015 (2015) 8.

6. M. Ratova, **R. Klaysri**, P. Praserthdam, P.J. Kelly, Pulsed DC magnetron sputtering deposition of crystalline photocatalytic titania coatings at elevated process pressures, Materials Science in Semiconductor Processing, 71 (2017) 188-196.

VITA

The author of this dissertation, Mr. Rachan Klaysri, was born in July 24, 1989 in Chachoengsao, Thailand. In 2008, he entered Mahanakorn University of Technology, Bangkok, Thailand, where he received his Bachelor of Engineering degree in Chemical Engineering with first-class honours in 2012. Then he started studying his Doctor of Engineering degree in Chemical Engineering at Chulalongkorn University, Bangkok, Thailand, with supported grant by the Royal Golden Jubilee Ph.D. scholarship from Thailand Research Fund (PHD/0067/2554), under Prof. Dr. Piyasan Praserthdam. Between September, 2016, and June, 2017, he was accepted to be a visiting PhD student for one academic year at Manchester Metropolitan University, Manchester, United Kingdom, under the care of Prof. Dr. Peter Kelly.